METAL LEACHING FROM OIL SANDS FLUID PETROLEUM COKE UNDER DIFFERENT GEOCHEMICAL CONDITIONS

A Thesis Submitted to the

College of Graduate and Postdoctoral Studies

In Partial Fulfillment of the Requirements

For the Degree of Master of Science

In the Department of Geological Sciences

University of Saskatchewan

Saskatoon

By

Mojtaba Abdolahnezhad

PERMISSION TO USE

In presenting this thesis in partial fulfillment of the requirements for a Postgraduate degree from the University of Saskatchewan, I agree that the Libraries of this University may make it freely available for inspection. I further agree that permission for copying of this thesis in any manner, in whole or in part, for scholarly purposes may be granted by the professor or professors who supervised my thesis work or, in their absence, by the Head of the Department or the Dean of the College in which my thesis work was done. It is understood that any copying or publication or use of this thesis or parts thereof for financial gain shall not be allowed without my written permission. It is also understood that due recognition shall be given to me and to the University of Saskatchewan in any scholarly use which may be made of any material in my thesis.

Requests for permission to copy or to make other uses of materials in this thesis/dissertation in whole or part should be addressed to:

Head
Department of Geological Sciences
University of Saskatchewan
144 Geology Building, 114 Science Place
Saskatoon, SK, S7N 5E2
Canada

Dean
College of Graduate and Postdoctoral Studies
University of Saskatchewan
116 Thorvaldson Building, 110 Science Place
Saskatoon, SK, S7N 5C9
Canada

ABSTRACT

The potential for metal leaching from fluid petroleum coke under different geochemical conditions was investigated, with a specific focus on metal mobility. Oil sands mine closure landscapes will contain overburden and upgrading by-products, including coke, stored permanently under varied geochemical conditions, and previous field and laboratory studies show that metal leaching is highly dependent upon the geochemical conditions within coke deposits. Therefore, this research will identify the potential for metal leaching and the relationship with water input composition with respect to the metal behavior. Petroleum coke contains elevated solid-phase concentrations of V (1380 ± 45 mg kg^{-1}), Ni (540 ± 18 mg kg^{-1}), Mo (75.1 ± 3.5 mg kg^{-1}), and several other potentially hazardous metal(loid)s (e.g., Cu, Cr, Co, Se, Zn). Laboratory column experiments focused on V, Ni, and Mo, which can occur at elevated dissolved concentrations in coke deposits. Here, we examined metal leaching from fluid petroleum coke in the presence of (i) meteoric water (pH = 7.2, Ionic strength < 0.01 M), (ii) oil sands process-affected water (OSPW; pH = 8.6, I = 0.05 M), and (iii) acid rock drainage (ARD; pH = 2.0, I = 0.2 M). These solutions mimic water types that may interact with coke in closure landscapes. The input, effluent, and profile samples collected over time showed that metal leaching is strongly dependent upon input solution composition. Vanadium and Mo leaching were greatest with ARD and OSPW, whereas sorption limited V and Mo mobility in the presence of meteoric water. Also, Mo leaching was likely promoted by the high ionic strength of ARD and OSPW solutions due to the release of weakly bound MoO_4^{2-} ions via competitive desorption, and a shift to net positive surface charge and dominance of $H_2MoO_4^0$ under ARD. Finally, enhanced Ni leaching in the presence of meteoric water and ARD is due to the limited potential for sorption and to the enhanced solubility of the hydroxide or carbonate phases. Although only a small proportion of total solid-phase V, Ni, and Mo was released, our results demonstrated that geochemical conditions strongly affect leaching behavior.

ACKNOWLEDGEMENTS

I would first like to acknowledge the steady support and mentorship of my supervisor Dr. Matthew Lindsay throughout my entire degree. Thank you for your patience and for providing both academic and professional development opportunities throughout my time with group. Many thanks to Dr. Samuel Butler for teaching me how to use the COMSOL Multiphysics simulation software. Also, thank you to Dr. Jim Meriam for providing geophysical instruments used in this research. Thank you to my external examiner for reviewing my thesis and providing comments.

My gratitude to Noel Galuschik for support in the lab, University of Saskatchewan staff Jing Chen for completion of porewater analyses, and Rafael Gonzales for his help in operating geophysical instruments and laboratory column setup.

Many thanks to my friends, especially Sana Daneshamouz, Alireza Zangouie, Soheil Naderi, Mohsen Asadi, Arash Tavassoli, Reza Azinfar, Mohamed Narimani, Renaud Attioua, Rafael Gonzales, and Mohamed Haiba for their motivation and friendship. Also, thank you for all the soccer players in Hangry Hippos and Due Birra Unito team for the joy and happiness throughout my program. Special thanks for Tod LeBlanc for managing the soccer team and inspiring me with geophysical inversion codes. Also, thanks for Lindsay group members for nominated me as the keeper of time, social butterfly, best office playlist, and jack of all trades' awards at our annual holiday parties.

Words cannot express my gratitude for having such a supportive brother through my academic and life, thank you so much. Finally, a special thank you to my parents, Zahra and Ardeshir, for their love and for supporting my decision to move so far away to pursue my dream especially my Mom, Zahra, as she was my first teacher. She taught me to be an independent, strong, and passionate person about my career. I remember this poem by Iranian poet Ferdowsi:

"Those who have knowledge, art, and culture,why worry if they lack treasure?"

I dedicate this thesis with a Persian poem by Saadi Shirazi to all health workers around the globe who are brave enough to stay in frontline against COVID-19.

"Human beings are members of a whole, since in their creation they are of one essence.

When the conditions of the time brings a member (limb) to pain,

the other members (limbs) will suffer from discomfort.
You, who are indifferent to the misery of others,
it is not fitting that they should call you a human being."

TABLE OF CONTENTS

LIST OF TABLES

LIST OF FIGURES

LIST OF ABBREVIATIONS

AOSR	Athabasca oil sand region
ARD	Acid rock drainage
AWS	Acid washed sand
CBE	Charge balance error
CEC	Cation exchange capacity
CFT	Centrifuged fine tailing
CSS	Cycling steam stimulation
DI	Deionized water
EC	Electrical conductivity
EDX	Energy dispersive X-ray
EMPA	Electron microprobe analyses
ER	Electrical resistivity
FTT	Froth treatment tailings
HDPE	High-density polyethylene
IC	Ion chromatography
ICP-MS	Inductively coupled plasma–mass spectrometry
ICP-OES	Inductively coupled plasma–optical emission spectroscopy
MLSB	Mildred lake settling basin
OSPW	Oil sand process-affected water
PES	polyethersulfone
pH_{PZC}	pH point of zero charge
PP	Polypropylene
PSD	Particle size distributions
PTFE	Polyfluorotetraethylene
PV	Pore volume
SAGD	Steam assisted gravity drainage
SCO	Synthetic crude oil

SEM	Scanning electron microscopy
SP	Self potential
SSA	Specific surface area
XANES	X-ray absorption near edge structure

CHAPTER 1: INTRODUCTION

Oil sand deposits in northern Alberta, Canada contain a mixture of bitumen, mineral solids, and water (Liu et al., 2005). Bitumen is extracted from deposits in the Athabasca Oil Sands Region (AOSR) either by (i) surface mining, hot water addition, and gravity separation or (ii) in situ heating and pumping followed by water removal (AER, 2019). Extracted bitumen is highly viscous and contains high asphaltene and sulfur contents, entrained solids and water, and elevated metal and salt contents (Gray, 2015). These characteristics make extracted bitumen unsuitable for simple refineries and instead bitumen is shipped to high conversion refineries. Many oil sands operations in the AOSR upgrade extracted bitumen to synthetic crude oil (SCO), which can be sold to conventional refineries at higher prices.

Bitumen upgrading involves several processes including vacuum distillation, coking, and hydro-conversion. Coking involves the thermal cracking of long-chain hydrocarbons in the non-distillable bitumen fraction into light hydrocarbons including naphtha, kerosene, and gas oils. Petroleum coke, the principal by-product of the coking process, was generated approximately 170 kg for m^3 of SCO in 2019 (AER, 2019). Fluid coking and delayed coking are the two principal coking methods used in the AOSR. The resulting fluid petroleum coke and delayed petroleum coke exhibit different physical and chemical properties, with the former accounting for approximately 60% of current petroleum coke production (AER, 2019). Approximately 1.13×10^7 t of petroleum coke were generated during bitumen upgrading in 2019 (AER, 2019). Coke stockpiles in the AOSR have steadily increased over time and reached 1.32×10^8 t by the end of 2019 (AER, 2019). These coke stockpiles will be integrated into mine closure landscapes in the AOSR (Simhayov et al., 2017), where the disturbed footprint due to surface mining activities currently exceeds 990 km^2 (CAPP, 2018).

Petroleum coke is a low-density carbonaceous material that contains a wide range of major, minor and trace elements (Kessler & Hendry, 2006; Zubot et al., 2012; Nesbitt et al., 2017). Elevated metal concentrations in petroleum coke leachate are a potential risk to water quality in mine closure landscapes that contain petroleum coke (Zubot et al., 2012; Nesbitt & Lindsay, 2017; Nesbitt et al., 2018, 2017; Robertson et al., 2019). Elevated V and Ni in coke-associated leachates can accumulate within plants and invertebrates in the AOSR, and these leachates are generally

acutely toxic to these organisms (Puttaswamy et al., 2010; Nakata et al., 2011; Puttaswamy & Liber, 2012, 2011; Baker et al., 2012). Nakata et al. (2011) reported that an accumulation of Mo within plants grown on fluid coke-bearing soil could cause molybdenosis in ruminants.

Previous research has shown that V and Mo leaching from fluid petroleum coke is enhanced under oxic conditions at neutral to alkaline pH, which are geochemical conditions that exist within the mixing zone between meteoric water and oil sand process-affected water (OSPW) below the water table of a commercial-scale deposit (Zubot, 2010; Puttaswamy & Liber, 2011; Nesbitt & Lindsay, 2017; Robertson et al., 2019). In addition, Ni release from fluid petroleum coke is increased under acidic pH, while its mobility is limited under alkaline pH (Nesbitt et al., 2018). However, relationships between geochemical conditions and metal leaching from fluid petroleum coke are poorly understood. Previous studies have examined V, Ni, and Mo leaching and mobility in the presence of meteoric water and OSPW, which will represent two principal water types in mine closure landscapes. The oxidative weathering of oil sands froth treatment tailings (FTT) also has a potential for acid rock drainage (ARD) generation within these landscapes (Kuznetsov et al., 2015; Lindsay et al., 2019). Although ARD is unlikely to represent a principal water type, information on metal leaching from fluid petroleum coke under acidic pH conditions would provide additional information to support mine closure planning.

1.1. Research Hypothesis and Objectives

This research will help to constrain the geochemical implications of potential closure scenarios with respect to metal leaching and mobility. My thesis research tests the overarching hypotheses that long-term metal leaching from oil sands fluid petroleum coke is controlled by the composition of associated waters.

To test this hypothesis, my research addresses the following objectives:

- *Objective 1:* Define the geochemical behaviour of petroleum coke under different water input compositions with respect to metal leaching and mobility;
- *Objective 2:* Investigate leaching efficiency and leaching behavior over time; and
- *Objective 3:* Establish a forward and inverse geophysical model to evaluate transport properties and determine porewater velocity.

CHAPTER 2: LITERATURE REVIEW

This chapter provides a review of bitumen extraction and upgrading, and establishes the current state of knowledge of the physical and chemical characteristics of oil sands petroleum coke. The environmental geochemistry of vanadium, nickel, and molybdenum are reviewed, and geophysical techniques and modeling approaches are described.

2.1. Alberta Oil Sands

Oil sands deposits in northern Alberta, Canada represent the largest crude bitumen reserve and the third-largest proven oil reserve in the world (AER, 2015). These deposits have in-place bitumen reserves estimated at 293.1 billion m^3 (AER, 2015), divided among three deposits: Athabasca, Cold Lake, and Peace River (Figure 2.1). The Athabasca deposit, also known as the AOSR, is the largest of these three deposits with recoverable bitumen reserves estimated 171 billion barrels (CAPP, 2018).

The AOSR consists of three main formations: the deeper Waterways, Wabiskaw-McMurray, and Clearwater (Hein & Cotterill, 2006; Gibson et al., 2013). All of these formations are overlain by a thin layer of Quaternary age glacial till sediment (Gibson et al., 2013). The near surface Clearwater Formation, which represent an approximately 10 m of shale unit, grades from silt to fine-grained sand downward, covering the Wabiskaw-McMurray Formation (Gibson et al., 2013). Bitumen in the AOSR hosted within the Wabiskaw-McMurray Formation was deposited during the Cretaceous period (145.5–65.5 Ma) and consists of sand with interbedded shales, sands, and silts (Hein & Cotterill, 2006; Gibson et al., 2013). The deeper Waterways Formation of Devonian age underlies the Wabiskaw-McMurray Formation and contains evaporite deposits within carbonate rock (Gibson et al., 2013).

The oil sands in the AOSR comprise silt, clay, sand, water, and bitumen. Oil sand ore, by weight, contains approximately 85% mineral solids, 5% water, and 10% bitumen (Liu et al., 2005; Zubot et al., 2012). The mineral solids contain abundant clays, including kaolinite (40–70% [w/w]), illite (28–45% [w/w]), and montmorillonite (1–15% [w/w]) and are dominated by quartz (Chalaturnyk et al., 2002).

Bituminous ore within the AOSR occurs in the southwest dipping McMurray formation, which outcrops near Fort McMurray, Alberta along the Athabasca and Clearwater rivers. Bitumen is a high molecular weight, viscous hydrocarbon that needs further upgrading before it can be sent for distribution (Masliyah et al., 2004; Liu et al., 2005).

Figure 2.1. Map of Alberta oil sands regions (AOSR). Public domain image created by N. Einstein (2011), Athabasca Oil Sands Mining Map, https://commons.wikimedia.org/wiki/File:Athabasca_Oil_Sands_map.png.

2.2. Bitumen Extraction

Oil sands operations in the AOSR extract bitumen using two main approaches: in situ extraction or surface mining. In situ bitumen extraction by steam assisted gravity drainage (SAGD) or cycling steam stimulation (CSS) target oil sands positioned approximately 150 to 450 m below the ground surface. In contrast, surface mining methods are suitable for oil sands located within 80 m of the ground surface (Kasperski & Mikula, 2011). Consequently, approximately 20% of bitumen reserves in the AOSR are extracted by surface mining operations (CAPP, 2018). These

operations use large power shovels and dump trucks to mine and haul oil sands ore to preparation plants. Mined ore is crushed and screened before being sent by conveyors to a slurry preparation plant, where hot water and process aids (e.g., sodium hydroxide, sodium citrate) are added to enhance bitumen extraction (Chalaturnyk et al., 2002; Masliyah et al., 2004). The bitumen slurry is pumped to an extraction plant via hydrotransport pipelines, where liberated bitumen attaches to entrained air bubbles to produce bitumen froth (Liu et al., 2005). The conditioned bitumen slurry then enters large gravity separation vessels, where the buoyant bitumen froth separates from liberated solids. The coarse solids are hydrotransported to tailings ponds whereas finer-grained solids (i.e., middlings), containing up to 4% (w/w) bitumen, are retained for additional extraction. The recovered bitumen froth is deaerated and sent to froth treatment, where diluent hydrocarbons (i.e., naphtha, paraffins) are added to decrease bitumen viscosity and liberate entrained solids (Masliyah et al., 2004; Liu et al., 2005). Following solvent recovery, the liberated solids are hydrotransported to tailings ponds and the extracted bitumen is retained for further processing. Overall bitumen recovery during the extraction process typically ranges from 88 to 95% (Chalaturnyk et al., 2002; Masliyah et al., 2004; Liu et al., 2005).

2.3. Bitumen Upgrading

Extracted bitumen cannot be processed at conventional refineries due the presence of water, solids, and impurities (e.g., sulfur, nitrogen, metals), high asphaltene content, and a low hydrogen to carbon ratio. Consequently, approximately 40% of all extracted bitumen is upgraded to SCO, which can be processed at conventional refineries and sells at a premium over extracted bitumen.

Bitumen upgrading to SCO involves the coking process, which involves thermal cracking of long and heavy chain hydrocarbons to shorter and lighter hydrocarbon compounds. In the AOSR, upgrading processes use either fluid or delayed coking, producing fluid or delayed petroleum coke, respectively (Gray, 2015). These methods involve the use of high temperature (350–550 °C, depending on the coking method) to break down long-chain hydrocarbons within the bitumen (Gray, 2015). The two types of petroleum coke have different physical and chemical properties depending on the bitumen feed and coking method (Kessler & Hendry, 2006).

In fluid coking units, bitumen is sprayed into the reactor while steam is injected from the bottom and coats the hot coke particles. Thermal cracking occurs on the surface of these particles at a temperature of 510–550 °C (Figure 2.2). Long and complex molecules crack into lighter and shorter hydrocarbons and leave the reactor vessels from the top as a vapor phase, moving to a

fractionator where vapor is fractioned into various petroleum products like gases, naphtha, light gas oil, and heavy gas oil. The coke particles in this process tend to grow in size; therefore, fine particles are separated by elutriation (based on size, shape, and density), and these relatively cold coke particles pass to the burner where they are combusted with air to supply heat to the reactor. Excess petroleum coke is removed from the burner vessel, mixed with OSPW to form a slurry, and hydrotransported by pipeline to dedicated deposits within tailings impoundments (Gray, 2015).

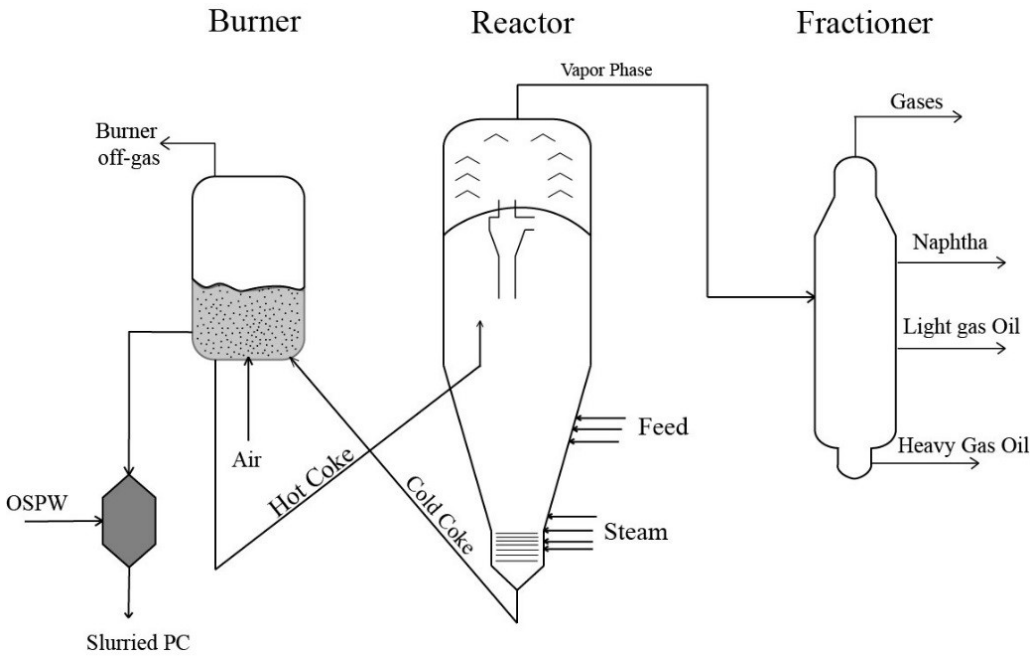

Figure 2.2. Schematic diagram of a fluid coker (after Gray, 2015).

2.4. Petroleum Coke

Petroleum coke is a by-product of the coking process, and is generated at a rate of over 170 kg for m^3 of SCO (AER, 2019). The bitumen upgrading process resulted in the production of approximately 1.13×10^7 t of petroleum coke, and coke stockpiles in the AOSR have steadily increased over time, reaching 1.32×10^8 t by the end of 2019 (AER, 2019). Over the lifetime of oil sands operations, coke stockpiled is expected to reach nearly 1 billion m^3 (Fedorak & Coy, 2006).

2.4.1. Physical Properties

Fluid petroleum coke consists of uniform spherical particles with a relatively low particle density (1.61 g cm^{-3}) and a fine sandy texture (Figure 2.3), resulting in a high hydraulic permeability of $1.48 \pm 0.12 \times 10^{-5}$ m s^{-1}, measured by Zubot (2010).

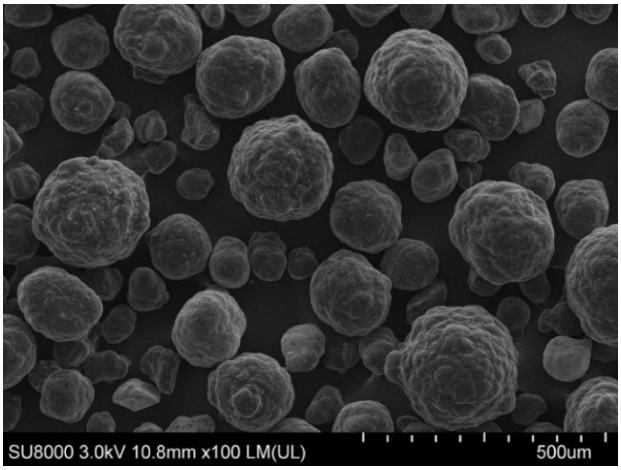

Figure 2.3. Scanning electron microscopy (SEM) image of fluid petroleum coke.

Backscattered electron images of fluid petroleum coke particles in thin section reveal concentric layers and perpendicularly radiating micro-structures attributed to mass addition and the cooling and heating cycles between the burner and reactor during the coking process (Nesbitt et al., 2017; Figure 2.4). Individual concentric layers comprise inner and outer regions measuring 5–10 μm and 1–5 μm thick, respectively. Jack et al. (1979) previously described this internal layering as an "onion skin" structure.

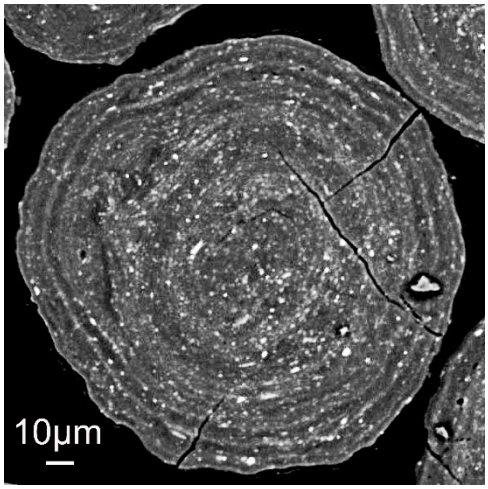

Figure 2.4. Backscattered electron (BSE) image of coke particle thin sections, showing the interior of coke particles.

Fluid petroleum coke exhibits a low specific surface area (SSA) with previous studies reporting values of 4.5 ± 2.8 $m^2 g^{-1}$ (Nesbitt et al., 2017), 6 $m^2 g^{-1}$ (Zubot et al., 2012), 8 $m^2 g^{-1}$ (Pourrezaei et al., 2014), 10 $m^2 g^{-1}$ (Har, 1981), and 11 $m^2 g^{-1}$ (Fedorak & Coy, 2006). The spherical shape and low porosity of fluid coke particles mean that the low SSA values are largely attributed

to primary surfaces. These physical properties also explain why fluid petroleum coke exhibits much lower porosity than activated carbon (>750 m^2 g^{-1}). Nevertheless, Pourrezaei et al. (2014) reported that mesopores with 2–40 nm apertures are likely important for geochemical reactions at surfaces of fluid petroleum coke particles.

2.4.2. Chemical Composition

Fluid petroleum coke is a low density carbonaceous material with elevated concentration of S derived from bitumen within the ore (Zubot et al., 2012; Nesbitt et al., 2017). Other major elements including Si, Al, Fe, Ti, Ca, K, and Mg are largely associated with entrained mineral phases (Nesbitt et al., 2017). Potentially hazardous metals including V, Mo, and Ni are also present at elevated concentrations in fluid petroleum coke particles (Zubot et al., 2012; Nesbitt et al., 2017; Nesbitt & Lindsay, 2017).

The inner and outer margins of the individual layers have different chemical properties. The inner margin of each individual layer contains mostly of C and S, while higher concentrations of V, Ni, Fe, Si, and Al are found at the outer margin (Nesbitt & Lindsay, 2017; Nesbitt et al., 2018). This finding suggests that these elements are concentrated at the outer margin of each concentric layer during the fluid coking process.

Nesbitt et al. (2017) reported that V and Ni are largely hosted within porphyrins and similar organic complexes throughout the fluid petroleum coke grains, which is consistent with their presence in bitumen ore (Figure 2.5). Molybdenum sulfide clusters promoted with nickel or cobalt (supported by alumina, γ-Al_2O_3, and silica), added as a catalyst to help hydro-conversion of bitumen, may incorporate into coke particles and introduce an inorganic source of Ni(II) and Mo(IV). Also, these catalysts may promote porphyritic conversion of Ni and V to their metal sulfide phases on the catalyst surface and provide another inorganic source of V(IV) and Ni(II) (Gray, 2015).

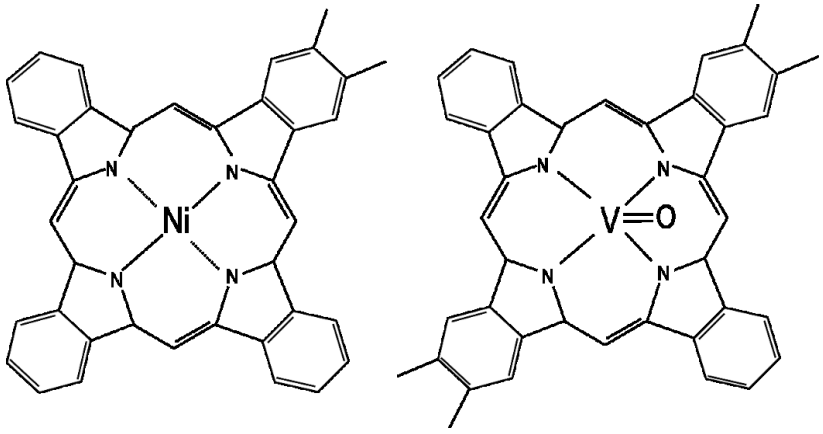

Figure 2.5. Chemical structures of metal species (Ni and V) in bitumen (after Gray, 2015).

Although porphyrin complexes are considered as stable and resistant complexes to weathering and thermal decomposition (Zuliani et al., 2016), degradation of these complexes has been reported previously in both field by Grosjean et al. (2004) and laboratory studies by Cordero et al. (2015). In addition, Zuliani et al. (2016) reported thermal decomposition of these stable porphyrin complexes are possible at temperatures higher than 400 °C. Moreover, distinct differences in V speciation between the inner and outer regions of individual layers suggests that the coking process may also degrade metalloporphyrin complexes (Nesbitt & Lindsay, 2017).

2.5. Metal Geochemistry

Among all the elements present in fluid petroleum coke, the potentially hazardous metals V, Ni, and Mo are of particular interest because of their elevated solid-phase concentrations and enhanced environmental mobility. Previous studies have reported dissolved V and Ni concentrations up to 3 mg L^{-1} and 120 µg L^{-1}, respectively within fluid petroleum coke deposits (Nesbitt & Lindsay, 2017; Nesbitt et al., 2018). Dissolved Mo concentrations exceeding 2.0 mg L^{-1} have also been reported within these coke deposits (Robertson et al., 2019).

Elevated metal concentrations in fluid coke leachate are a potential risk to water quality in the AOSR (Zubot et al., 2012; Nesbitt & Lindsay, 2017; Nesbitt et al., 2018; Robertson et al., 2019). Elevated V and Ni in coke leachates are reported to be acutely toxic to some aquatic organisms (Puttaswamy et al., 2010; Puttaswamy & Liber, 2012, 2011; Jensen-Fontaine et al., 2014). Nakata et al., (2011) conducted a greenhouse study to investigation the effect of coke on plant growth and reported phytotoxic concentrations of Ni and V. Also, plants grown on coke can accumulate Mo at a concentration which could cause molybdenosis in ruminants (Nakata et al., 2011). Since produced coke may be integrated into the reclamation landscape within the AOSR, and because of the potential risk presented by coke and the associated leachate, understanding the metal geochemistry of coke is critically essential.

2.5.1. Vanadium

Routinely, heavy-type oil deposits, such as oil sands bitumen contain elevated V concentrations (Dechaine & Gray, 2010; Zuliani et al., 2016). Strong & Filby (1987) reported V concentrations of 180 to 196 mg kg^{-1} within Alberta bitumen reservoirs, and fluid petroleum coke typically exhibits V concentrations of 1000 to 2000 mg kg^{-1} (Jack et al., 1979; Har, 1981; Chung, 1996; Kessler and Hendry, 2006; Zubot et al., 2012; Nesbitt et al., 2017). Nesbitt et al. (2017) reported that V(IV) porphyrins are the dominant form of V in petroleum coke. Nesbitt and Lindsay

(2017) subsequently found that V(IV) porphyrins dominate V speciation in the inner region of these layers, whereas both V(IV) porphyrins and octahedrally coordinated V(III) are abundant at the outer margins of individual layers. Minor to trace V(V) concentrations have also been detected within fluid petroleum coke particles (Nesbitt et al., 2017; Nesbitt & Lindsay, 2017).

The high stability of V(IV) porphyrin complexes and the prevalence of V(III) at the outer margin of concentric layers make V(III) a potential source of dissolved V in fluid petroleum coke leachate, however the contribution of V(V) to the dissolved V in fluid petroleum coke leachates cannot be ruled out.

Li et al. (2007) reported the presence of V(IV) and V(V) within petroleum coke leachate, however, V(IV) is oxidized rapidly to V(V) under oxic conditions (Jensen-Fontaine, 2012). In soil, the mobile V species is mainly V(V), and only a small amount is present as V(IV) (Baken et al., 2012; Burke et al., 2012; Huang et al., 2015). Laboratory studies demonstrate that V leaching from fluid petroleum coke is enhanced under oxic conditions and at neutral to alkaline pH (Zubot, 2010; Puttaswamy & Liber, 2011). Nesbitt & Lindsay (2017) observed enhanced V mobility under similar geochemical conditions within the mixing zone between meteoric water and OSPW below the water table of a commercial-scale fluid coke deposit. Positive correlation between pH and V leaching and mobility have also been reported in previous laboratory studies (Wehrli & Stumm, 1989; Zubot, 2010; Puttaswamy & Liber, 2011; Pourrezaei et al., 2014).

Vanadium is a transition metal with six possible oxidation state ranging from V(−I) to V(V); however, V(III), V(IV), and V(V) are dominant in the environment (Baes and Mesmer, 1976; Huang et al., 2015). Reduction–oxidation (redox), precipitation–dissolution, and sorption–desorption reactions control V mobility within surface and groundwater systems (Wehrli & Stumm, 1989; Peacock & Sherman, 2004; Wright et al., 2014; Huang et al., 2015). Although V(III) is thermodynamically stable over a wide range of pH values (Wright & Belitz, 2010), aqueous V(III) rapidly hydrolyzes to form VOH^{2+}, $V(OH)_2^{+}$, and $V_2(OH)_2^{4+}$ (Pajdowski, 1966; Pajdowski & Jeżowska-Trzebiatowska, 1966), and V(III) (oxy)hydroxides rapidly precipitate from solution over a wide pH range (Wanty & Goldhaber, 1992). Aqueous V(III) species can also oxidize rapidly to V(IV) or V(V) under oxic conditions and are, therefore, relatively rare in surface waters and shallow groundwater (Aureli et al., 2008; Wang and Sañudo Wilhelmy, 2009; Wällstedt et al., 2010). Under anoxic conditions, microbial reduction of dissolved V(V) to V(IV) or V(III) is possible (Li & Le, 2007; Li et al., 2009) and may be coupled to microbial oxidation of organic matter (Borch et al., 2010) or abiotic oxidation of aqueous Fe(II) (Vessey & Lindsay, 2020). However, reduction rates

generally decrease with increasing pH and are slowest above pH 6 (Huang et al., 2015). Also, a simultaneous reduction of V(IV) to V(III) couple with H_2S oxidation might occur; however, reduction rates are remarkably slow, even with the presence of higher H_2S concentrations that reported by Nesbitt et al. (2018) at fluid petroleum coke deposits. Complexation of V(IV) and V(III) with inorganic and organic ligands also influences aqueous V geochemistry including the inhibition of redox reactions (Wanty & Goldhaber, 1992; Jensen-Fontaine, 2012; Huang et al., 2015). The Pourbaix (Eh–pH) diagram for a median V concentration in fluid petroleum coke was determined using modified MINTEQ.V4 database (Vessey et al., 2020) in PHREQCi (Figure 2.6).

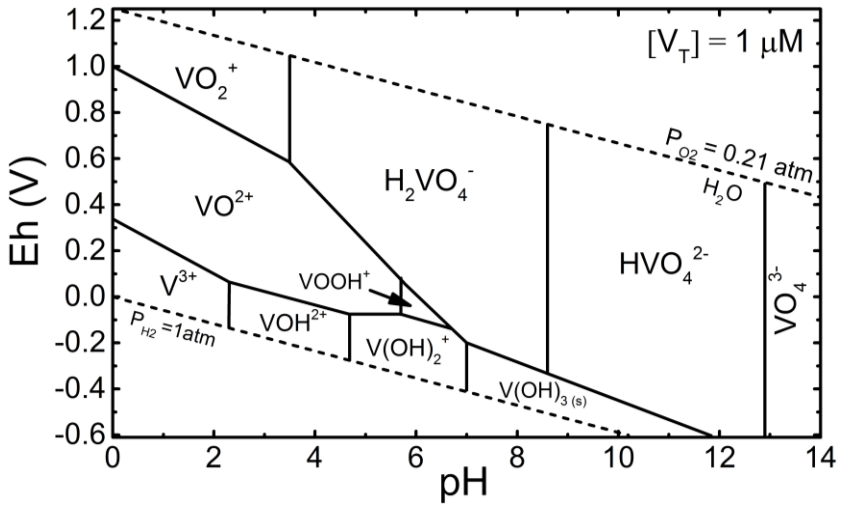

Figure 2.6. Pourbaix (Eh–pH) diagram for a total aqueous concentration of 1 µM vanadium.

At concentrations exceeding 100 µM, aqueous V can polymerize to form aqueous species containing up to 10 V atoms (Figure 2.7; Wanty & Goldhaber, 1992; Elvingson et al., 1996; Cruywagen, 1999; Gustafsson, 2019). Using the reaction enthalpy for V_4 and V_5 cyclic species, V stability is enhanced by poly-nucleation (Huang et al., 2015; McCann et al., 2015). The formation of aqueous V polymers has recently been shown to affect surface complexation by Fe(III) (oxyhydr)oxides commonly found in soils and sediments.

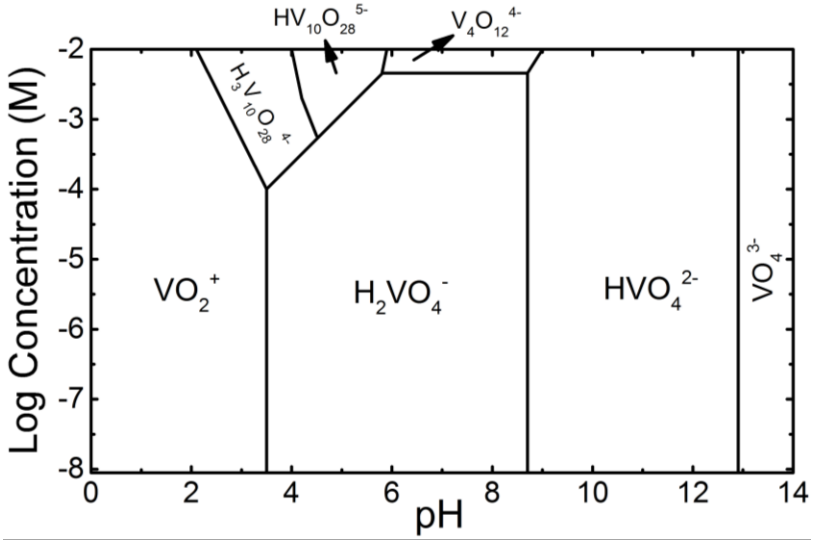

Figure 2.7. Predominance diagram showing aqueous V(V) speciation as a function of pH and $[V]_T$.

Vanadium species are readily leachable under oxic condition and predominantly as V(V), although V(IV) has been detected. However, V(IV) is expected to oxidize rapidly to V(V) under oxic conditions.

Long-term V leaching and mobility within associated coke leachates are complex processes depending on the interaction of coke with water matrixes, V aqueous speciation, and the geochemical conditions of coke storage. However, complex interaction mechanisms between coke and OSPW in the long-term led to a gradual decrease in the aqueous V concentration (Zubot et al., 2012). This result suggests a dynamic fluctuation in the V partitioning between coke and the aqueous phase within coke deposits.

2.5.2. Nickel

Strong & Filby (1987) reported a Ni concentration of 62–75 mg kg^{-1} within Alberta bitumen. Associated fluid petroleum coke typically exhibits a Ni concentration of 35–719 mg kg^{-1} (Jack et al., 1979; Chung, 1996; Kessler & Hendry, 2006; Zubot et al., 2012; Nesbitt et al., 2018, 2017). Nesbitt et al. (2018) reported that Ni(II) porphyrin complexes are the dominant Ni form in petroleum coke. Nesbitt et al. (2018) found that X-ray absorption near edge structure (XANES) spectra from the inner and outer margins of individual concentric layers are usually different, and heterogeneous distribution and speciation of Ni within coke particles has been discovered, including organic and inorganic phases. Nickel(II) porphyrin complexes are the dominant form of solid-phase Ni in the inner region of these concentric layers, while the outer margins contain inorganic Ni(II)-sulfide and Ni(II)-oxide, constituting a minor component of Ni in fluid coke (Nesbitt et al., 2018). The

dominance of porphyrin complexes in fluid petroleum coke is consistent with the geological petroleum system (Lewan & Maynard, 1982; Lewan, 1984).

Adding Mo(IV)-disulfide (MoS_2) along with Ni and Co (supported by alumina, γ–Al_2O_3, and silica) as catalysts for the hydro-conversion of bitumen distillates prior to coking may cause Ni to incorporate into coke particles and therefore could introduce an inorganic source of Ni. In addition, the catalyst may promote the porphyritic conversion to the sulfide phase (Gray, 2015), providing another inorganic source of Ni. These inorganic phases, plus the thermal decomposition of porphyrin complexes during the coking process, results in heterogeneous Ni distribution and speciation within coke particles (Nesbitt et al., 2018).

Nesbitt et al. (2018) observed enhanced Ni release from fluid petroleum coke at elevated ionic strength and acidic pH. Also, Nesbitt et al. (2018) reported an aqueous Ni concentration of 2–120 μg L^{-1} within coke deposits from the AOSR with a significant negative correlation between dissolved Ni concentrations and pH. A similar negative correlation between pH and Ni concentration in coke pore water was discovered by Zajic et al. (1977). Puttaswamy & Liber (2011) reported a Ni concentration of 145 ± 31 μg L^{-1} at pH 5.5 in contrast with 0.2 ± 0.1 μg L^{-1} at pH 9.5 in oil sands fluid petroleum coke. The observed negative relationship between pH and dissolved Ni concentrations may result from the pH-dependent variation in net surface charge and sorption of Ni^{2+} and positively charged Ni complexation (i.e., $NiHCO_3^+$) on the coke surface. This also implies that the pH_{PZC} (pH point of zero charge) for Ni is an important factor that could control Ni mobility within fluid coke deposits.

Nickel(II) is the dominant oxidation state of Ni in the environment and it is soluble in most natural waters, except for at pH > 10 where low-solubility Ni(II) hydroxides are formed and precipitated (Hummel & Curti, 2003). Nickel is less redox-sensitive than V, existing exclusively in the Ni(II) oxidation state (Figure 2.8).

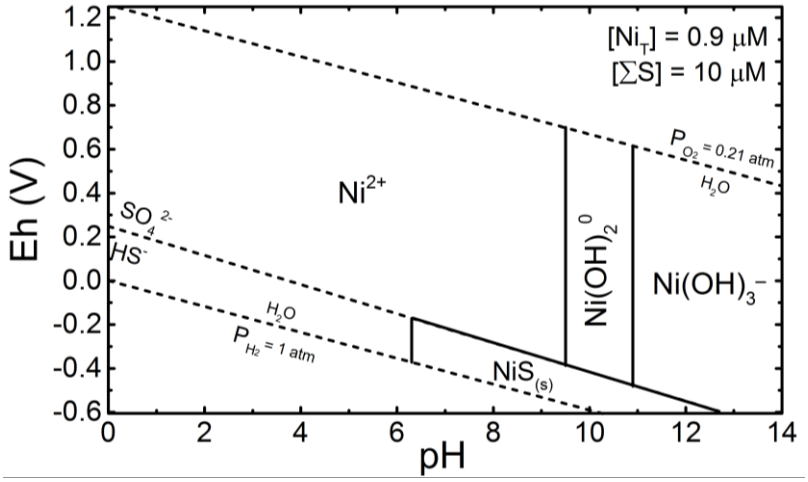

Figure 2.8. Pourbaix (Eh–pH) diagram for Ni at 0.9 μM total aqueous concentration.

The precipitation of the secondary sulfide phase (i.e., $NiS_{(s)}$, mackinawite [$FeS_{(s)}$], and pyrite [FeS_2] in the presence of H_2S) may limit dissolved Ni concentrations. Incorporation of Ni into the formed mackinawite and pyrite formed under sulfate-reducing conditions may limit Ni mobility (Huerta-Diaz et al., 1998; Luther et al., 1980; Rickard, 2012). Aqueous Ni speciation and mobility is also controlled by the presence of ligands such as sulfate (SO_4^{2-}), carbonate (CO_3^{2-}), and bicarbonate (HCO_3^-; Figure 2.9). Pore water pH, sorption–desorption, complexation, and (co)-precipitation reactions are the principal controls on dissolved Ni concentration and mobility within oil sands fluid petroleum coke deposits.

Inorganic Ni is likely the primary long-term source of dissolved Ni in fluid petroleum coke deposits, and its release and mobility are highly correlated with porewater pH and sorption–desorption reactions such that: (1) acidic environments lead to high release and mobilisation of Ni, and (2) alkaline environments can limit the Ni mobility.

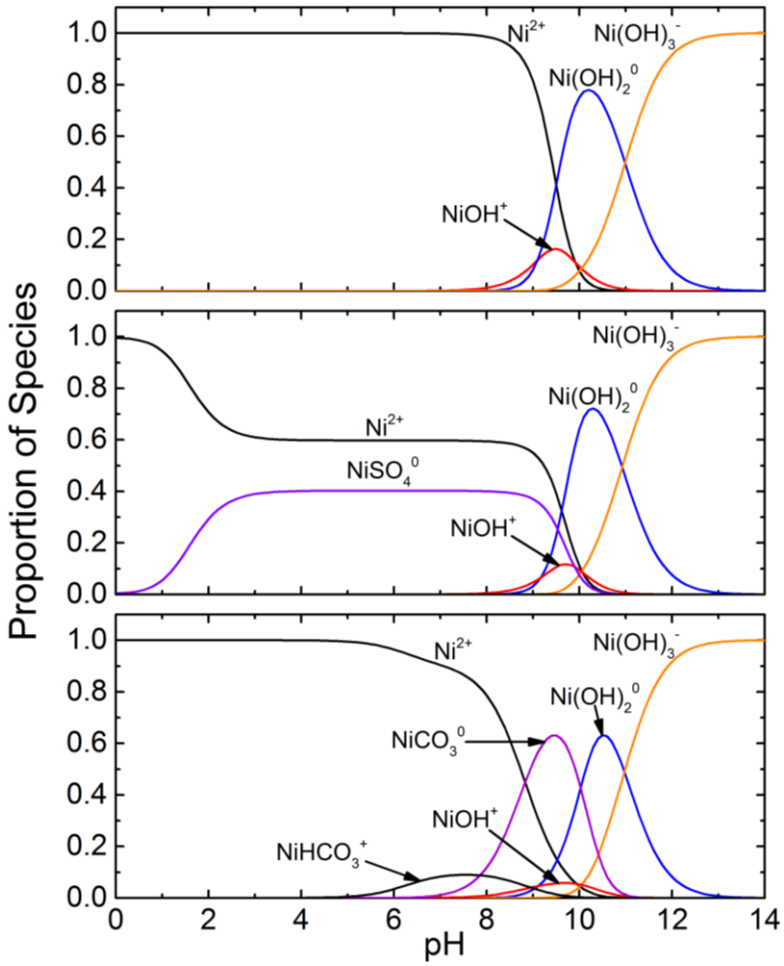

Figure 2.9. Nickel(II) hydroxide speciation (top), Ni(II) complexation in the presence of sulfate (1000 mg kg^{-1}; middle), and Ni(II) complexation in open carbonate systems (bottom).

2.5.3. Molybdenum

Fluid petroleum coke typically exhibits Mo concentrations of 7.6–121 mg kg^{-1} (Jack et al., 1979; Chung, 1996; Kessler & Hendry, 2006; Zubot et al., 2012; Nesbitt, 2016). Robertson et al. (2019) reported that Mo occurs as Mo(VI), outer- and inner-sphere complexes, and Mo(IV) in petroleum coke. A lower proportion of outer-sphere Mo(VI) complexes relative to inner-sphere complexes was observed by Robertson et al. (2019) in a slurry coke sample, which suggests that outer-sphere complexes are susceptible to leaching under the geochemical conditions within the coke deposit.

Although solid-phase Mo concentrations are relatively low compared with V and Ni, Mo concentrations in pore water within AOSR coke deposits are comparable to dissolved V and Ni (Nesbitt and Lindsay, 2017; Nesbitt et al., 2018; Robertson et al., 2019). Robertson et al. (2019) reported a dissolved Mo concentration of 0.097–2.2 mg L^{-1} within coke deposits, with the maximum

concentration below the water table within the mixing zone between slightly acidic and oxic meteoric water and mildly alkaline and anoxic OSPW. This mixing zone resulted in elevated pH, electrical conductivity (EC), and ionic strength, and likely mobilized the outer-sphere Mo(VI) complexes (Robertson et al., 2019). Also, geochemical modeling of pore water within AOSR fluid petroleum coke deposits suggested that MoO_4^{2-} is the dominant aqueous species of Mo(VI); therefore, the presence of MoO_4^{2-} adsorption complexes is possible (Robertson et al., 2019).

Molybdenum exhibits complex aqueous geochemistry and occurs in a range of oxidation states, and also could form complexes with cations, anions, and organic ligands. Molybdenum(VI) is the dominant oxidation state in most oxic natural water and is present as tetrahedral MoO_4^{2-} (Goldberg et al., 1996; Xu et al., 2013; Smedley & Kinniburgh, 2017). The dissolved Mo concentration is controlled by aqueous Mo species, pH, redox potential, sorption–desorption, and precipitation–dissolution reactions (Smedley & Kinniburgh, 2017). The integration of these factors defines Mo mobility and attenuation within AOSR deposits. Fe-(hydr)oxides, pyrite, clay minerals, and organic matter are the phases existing within the coke that can adsorb MoO_4^{2-}; therefore, Mo mobility and attenuation could be controlled by the presence of these phases and their activity. These phases have the highest adsorption capacity under mildly acidic conditions since the net surface charge is positive (~pH 3–6)(Goldberg et al., 1996; Bostick et al., 2003; Gustafsson & Tiberg, 2015). However, increasing pH and ionic strength would decrease their adsorption capacity, with minimal adsorption occurring at pH > 8 (Goldberg et al., 1996; Gustafsson & Tiberg, 2015). At circumneutral to alkaline pH, Mo occurs as soluble molybdate (MoO_4^{2-}; [Mo(VI)]). Organic matter, clay minerals, and pyrite exhibit net negative surface charge under these pH conditions, whereas net surface charge is neutral or slightly negative for Fe-(hydr)oxides phases. Consequently, molybdate adsorption is typically limited at neutral to alkaline pH (Smedley & Kinniburgh, 2017).

Precipitation of relatively insoluble metal molybdate phases (e.g., $NiMoO_4$, $PbMoO_4$, and $CaMoO_4$) caused by elevated ionic activities have been reported in neutral to alkaline mine tailings (Essilfie-Dughan et al., 2011; Conlan et al., 2012; Blanchard et al., 2015) and could limit Mo concentrations in fluid petroleum coke deposits. Under sulfate-reducing conditions, a series of intermediate thiomolybdate species including MoO_3S^{2-}, $MoO_2S_2^{2-}$, $MoOS_3^{2-}$, and MoS_4^{2-} could form (Figure 2.10; Helz et al., 1996; Xu et al., 2013). These thiomolybdates dominate Mo speciation in sulfidic environments (Smedley & Kinniburgh, 2017) and are readily attenuated by co-precipitation or adsorption reactions at mineral surfaces (Helz et al., 1996; Bostick et al., 2003; Das et al., 2007).

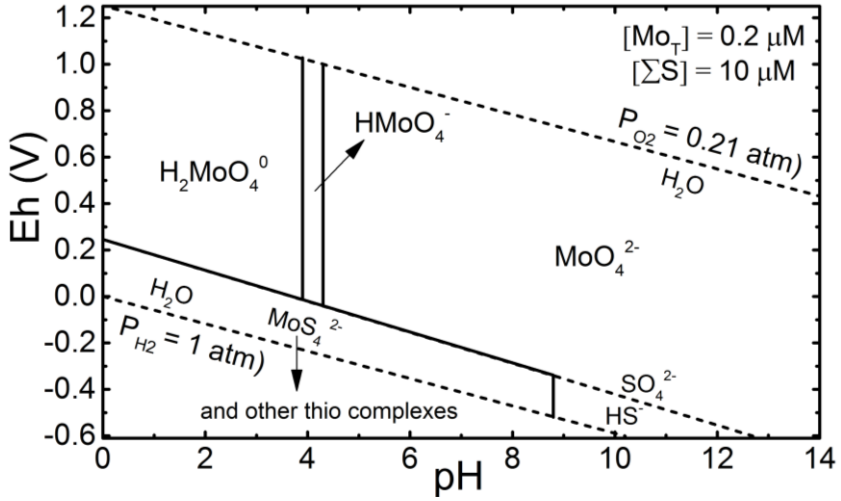

Figure 2.10. Pourbaix (Eh–pH) diagram for a median concentration of Mo at 1 μM total aqueous concentration found within fluid petroleum coke deposits.

Aqueous Mo(VI) polymerizes to form $H_xMo_7O_{24}^{x-6}$, where x = 1 to 3, at high $[Mo]_T$ (i.e., $\geq 10^{-3}$ M) and acidic pH (i.e., < 6; Figure 2.11; Xu et al., 2013; Smedley & Kinniburgh, 2017).

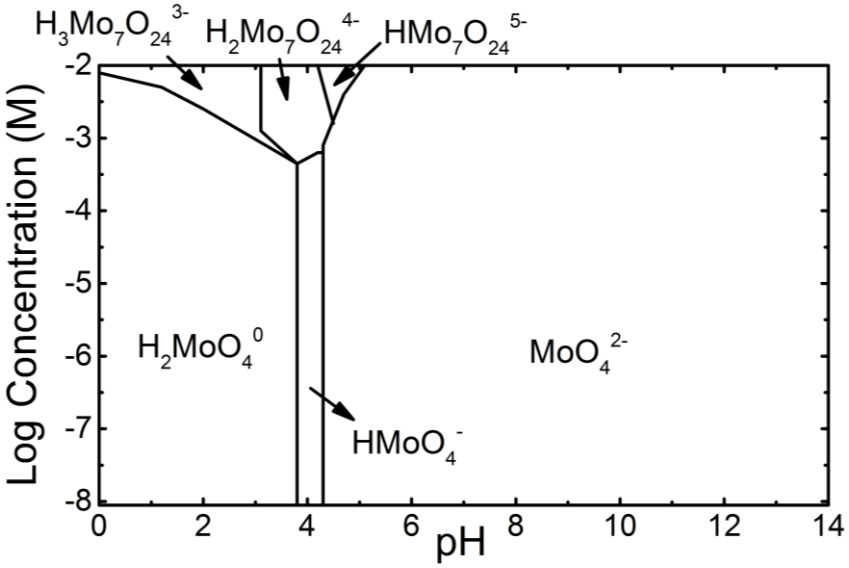

Figure 2.11. Predominance diagram showing aqueous Mo(VI) speciation as a function of pH and $[Mo]_T$.

Since adsorbed MoO_4^{2-} is readily mobilized in the presence of OSPW, the oxidative dissolution of MoS_2 is likely a principal long-term source of dissolved Mo in fluid petroleum coke deposits (Robertson et al., 2019). However, MoS_2 is both highly insoluble and resistant to oxidative weathering, suggesting that long-term Mo release may be limited (Lindsay et al., 2015).

2.6. Mine Closure Considerations

Oil sands mining operations have disturbed a large land area within the AOSR including forests and peatlands, primarily fens covering >50% of landscape (Price et al., 2010; Vitt et al., 1996). Regulations ensure that disturbed land is progressively reclaimed to an acceptable state once operations have reached the end of their productive life. Therefore, environmental conservation is considered throughout a project, from planning to reclamation and reforestation. Tailings (fluid fine tailings [FFT], centrifuged fine tailing [CFT], tailings sand, etc.), petroleum coke, and overburden within the AOSR will likely be stored together in terrestrial or subaqueous closure landscapes. However, the interaction between these materials, with different physical and chemical properties, as well as the potential effects of these interactions on the overall success of a closure system, is a major concern and needs further investigation.

Petroleum coke can act as a low density, highly permeable aggregate for a light capping on soft tailings material such as CFT and tailings (Sobkowicz et al., 2012; Simhayov et al., 2017). The use of petroleum coke as a capillary break between CFT and reclamation material (peat-mineral mix soil) was investigated by Cilia (2018) and Swerhone (2018). Also, Simhayov et al. (2017) used a layer of petroleum coke as a construction material to create a self-sustaining, peat accumulating fen-upland ecosystem. In a fen system, petroleum coke can act as permeable underdrain to distribute the hydraulic pressure (water and solute flows) beneath the fen. Moreover, several research studies have investigated the use of petroleum coke for OSPW management including a water treatment option (Gamal El-Din et al., 2011; Zubot et al., 2012). However, potential leachability of certain trace elements, reported previously by Nesbitt (2016) and Swerhone (2018), make their applications limited.

The leachability of elements in petroleum coke depends on the physical and chemical properties of the coke and the composition of the water that may interact with it. Previous field studies have examined the potential for metal leaching by meteoric water and OSPW, however it is possible that petroleum coke may also encounter ARD generated by the oxidative weathering of froth treatment tailings (Kuznetsov et al., 2015; Lindsay et al., 2019). Metal leachability and the interaction between petroleum coke and ARD has not been previously established. Therefore, a better understanding of long-term metal leaching from petroleum coke under different geochemical conditions relevant to mine closure is critical. The results of this study will improve the understanding of metal (i.e., V, Ni, and Mo) leaching and mobility within the oil sands mine closure

landscape, and will assist decision makers (i.e., mine closure planners) to develop strategies for integrating coke into closure landscapes while limiting the release and transport of metals.

2.7. Hydrogeophysics

Hydrogeophysics is a research area which uses non-destructive or minimally destructive methods (i.e., electrical resistivity [ER]; self-potential [SP]) to evaluate hydrogeological parameters such as permeability and dispersivity, water content, water quality, and biological activity (Naudet & Revil, 2005; Ntarlagiannis et al., 2005; Rubin & Hubbard, 2005; Williams et al., 2005; Hubbard & Linde, 2011; Revil et al., 2012; Ahmed et al., 2016).

Electrical resistivity (ER) is an active geophysical method and is performed by injecting a current waveform through electrodes (sink and source) and measuring the respond voltage difference through potential electrodes. ER corresponds with water content, temperature, the salinity of pore water, clay content, and mineralogy (Binley et al., 2015; Singha et al., 2015). Rock texture, pore-space geometry, and mineralogy are factors that control solute transport processes within the subsurface and together resulted in spatial-temporal changes in solute concentrations. Knowing the link between petrophysical properties with geophysical parameters is necessary to interpret and study the transport process. Coupling geophysical and tracer test have been investigated before as a tool to resemble solute transport in the subsurface (Binley et al., 2002; Slater et al., 2002; Martínez-Pagán et al., 2010; Bolève et al., 2011). The inverse problems conditionally can be parametrized to employ stochastic inversion to determine the probability density of material properties, such as permeability. Forward and inverse modeling are needed to interpret the measured data at the site or in the lab (Appendix A).

CHAPTER 3: MATERIALS AND METHODS

3.1. Laboratory Columns Experiments

Laboratory column experiments were conducted to assess long-term metal leaching from fluid petroleum coke during interaction with different water types that could be encountered in oil sands mine closure landscapes. Based on previous field studies, meteoric water and OSPW are the two prevalent compositions anticipated in oil sands mine closure landscapes, whereas localized ARD generation associated with sulfide-mineral oxidation in FTT deposits is possible (Kuznetsov et al., 2015; Nesbitt et al., 2017; Lindsay et al., 2019), so these water compositions were selected for experiments (meteoric water was simulated by deionized water [DI]). Two separate experiments were conducted to (i) examine geochemical controls on long-term metal release and (ii) determine the timing and extent of long-term metal release.

The first experiment examined long-term metal leaching in a series of small columns. In these experiments, each solution was continuously passed through a separate column containing fluid petroleum coke collected directly from a coker unit (dry coke) and another column containing fluid petroleum coke collected from a hydrotransport line (slurry coke). The second experiment examined long-term metal leaching in a large column. In this experiment, the three different solutions were sequentially passed through a column containing dry coke. Hydrogeophysical methods were used to monitor transport within the large column. Aqueous influent, effluent, and profile samples were collected from both the small and large columns over time. Solid-phase samples were collected from all columns at the beginning and end of the experiments.

3.1.1. Small Column Setup

The first laboratory column experiments utilized (i) six acrylic columns measuring 0.225 m long with 0.078 m inner diameter, (ii) fresh dry and slurry coke, and (iii) acid-washed #20–#40 mesh Ottawa sand (Figure 3.1). All small columns were packed with 16.5 cm fresh dry coke (n = 3) or fresh slurry coke (n = 3) placed between two layers of 0.03 m acid-washed sand (AWS). The AWS layers were placed at the top lower and upper layer and used to direct a homogeneous flow of water through the coke layer (middle layer). Nylon mesh screen (No. 125) was used to separate the coke from the acid-washed sand layers. The layers were packed to ensure that the bulk density

was consistent along the column and among all columns for each material (Appendix B). Sampling tubes were installed within sampling ports at 0.03 m intervals from 0.035 m to 0.185 m relative to the column base. Sampling tubes, constructed from polyfluorotetraethylene (PTFE) tubes, were installed into each sampling port to facilitate pore water sampling. These 0.08 m samplers were sealed at one end and perforated along their length prior to installation. Following installation, the tubes were sealed into the ports with cyanoacrylate crazy glue, and two-way stopcocks were attached to facilitate sampling via syringe (Figure 3.1).

Each column was fitted with one inlet and one outlet port. The inlet port was connected to a high-precision, low-flow multi-channel peristaltic pump (Model 2058, Watson-Marlow, Inc.) using PTFE tubing. The outlet port was connected in series to a sealed overflow sampling cell and then an overflow waste container. Before starting the experiment, the columns were flushed for 48 h with $CO_{2(g)}$, which is highly soluble in water, and therefore minimizes bubble entrapment during initial water saturation.

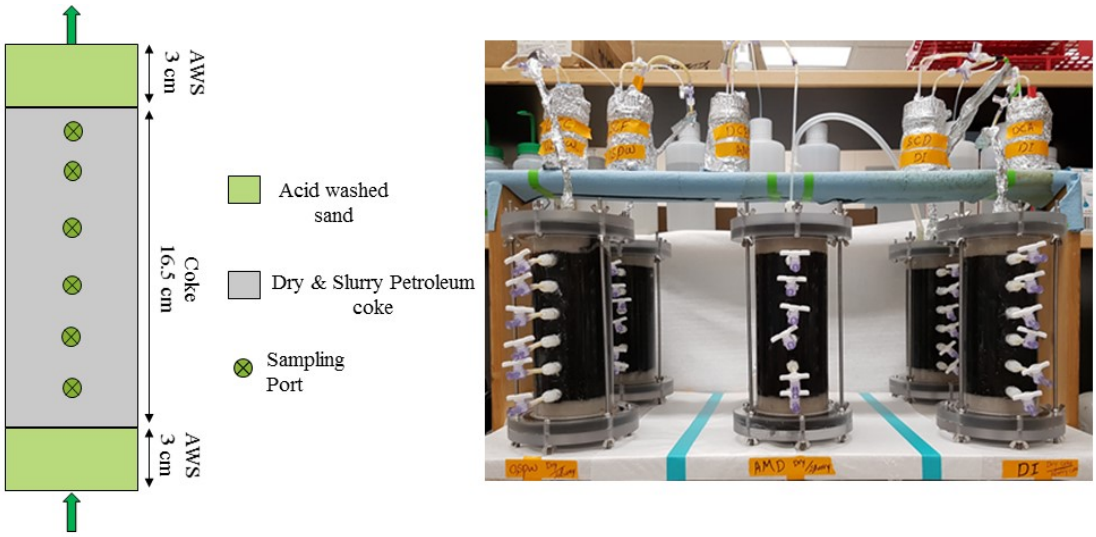

Figure 3.1. Schematic diagram and photo of the small column experiments. The coke layers were placed between two acid washed sand (AWS) layers.

3.1.2. Large Column Setup

The second laboratory column experiment (sequential water input with different compositions) utilized (i) one PVC column measuring 0.67 m long with 0.162 m inner diameter, (ii) fresh dry coke, and (iii) acid-washed #20–40 mesh Ottawa sand (Figure 3.2). The column was packed with 0.5 m of fresh dry coke between two 0.085 m layers of acid-washed sand. In order to

avoid mixing of acid-washed sand with coke, a nylon mesh screen (No. 125) was placed between these two layers. Packing ensured that the bulk density was consistent along the column (Appendix B). Five sampling ports were positioned at 0.10, 0.15, 0.25, 0.35, and 0.40 m from the base of the coke layer and equipped with pore water suction samplers (Rhizon MOM, Rhizosphere Research Products B.V., The Netherlands). These sampling ports were sealed with a cyanoacrylate crazy glue to prevent leaks. Non-polarizing Ag/AgCl pellet electrodes (n = 11) were installed at intervals of 0.05 m along the column for time-lapse SP geophysical method measurements, from 0.115 m to 0.615 m from the column base. These electrodes were used to measure the voltage differences between each electrode and the reference electrode (the last electrode). A platinum wire was cut into 0.01 m long pieces to use as an electrode for time-lapse geophysical resistivity measurements. Four electrodes were positioned at 90° angles in a ring configuration at 0.09 m intervals, except for the first and last that were at 0.05 m intervals, from 0.06 m to 0.61 m from the column base. This configuration was based on sensitivity analysis performed using COMSOL Multiphysics (COMSOL Multiphysics® v.5.4). The large column was instrumented with eight platinum rings and 11 Ag/AgCl pellet electrodes. Time-lapse geophysical measurements (ER, SP) were performed using the IRIS (Syscal, France) instrument during the tracer tests (twice a day, every 12 h), and recorded data were prepared for geophysical modeling.

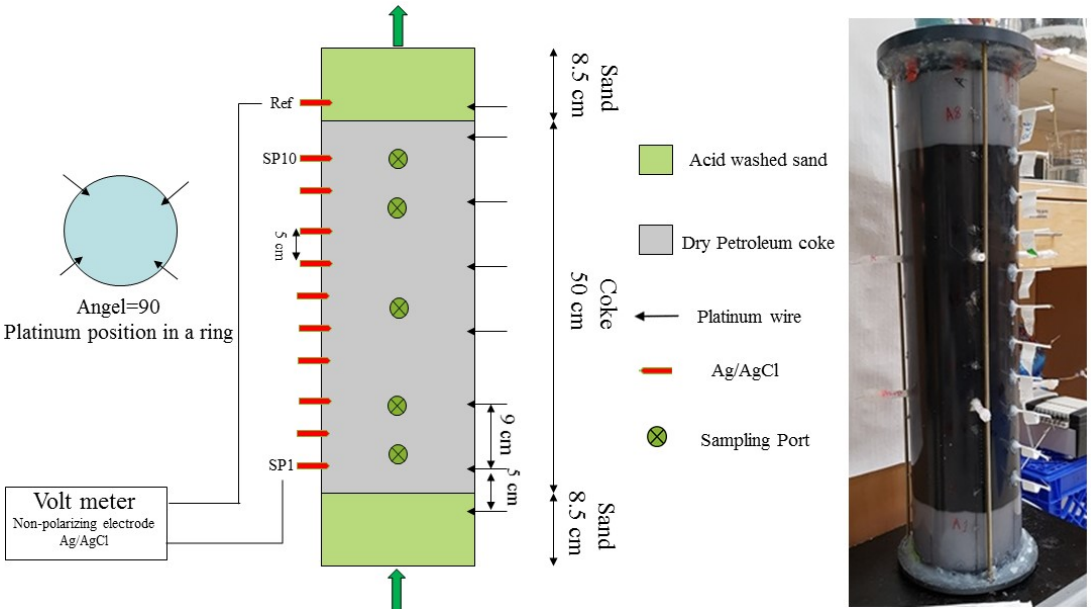

Figure 3.2. Graphical representation of the placement of platinum wire (left); schematic representation of column experiment (middle); photograph of the fully constructed column (right).

The large column was fitted with one inlet and one outlet port. The inlet port was connected to a high-precision, low-flow multi-channel peristaltic pump (Model 2058, Watson-Marlow, Inc.) using PTFE tubing. Overflow sampling cell was sealed, and then in series outlet port, overflow sampling cell and waste jug were all connected using PTFE tubing. Before starting the experiment, the columns were flushed for 48 h with $CO_{2(g)}$, which is highly soluble in water, and therefore minimizes bubble entrapment during initial water saturation.

3.1.3. Input Solutions

Input solutions were prepared in 5 L acid-washed amber glass media bottles using DI water and ACS reagent-grade salts. The composition of synthetic OSPW and ARD solutions were based on previous studies (Dompierre et al., 2017; Lindsay et al., 2019; Table 3.1). The synthetic OSPW solution was prepared by dissolving (g L^{-1}) NaCl (1.78), $NaHCO_3$ (1.34), $MgSO_4 \cdot 7H_2O$ (0.203), $CaSO_4 \cdot 2H_2O$ (0.172), KCl (0.038), and Na_2SO_4 (0.037) into DI water. While continuously stirring, the solution was purged with $CO_{2(g)}$ overnight and then with compressed air for 24 h until the solution pH stabilized at approximately 8.4. The synthetic ARD solution was prepared by dissolving (g L^{-1}) $Fe_2(SO_4)_3 \cdot xH_2O$ (11.2), $MgSO_4 \cdot 7H_2O$ (2.03), $CaSO_4 \cdot 2H_2O$ (1.72), Na_2SO_4 (0.315) and NaCl (0.248) in DI water. The ARD solution was adjusted to pH 2.0 using concentrated H_2SO_4. The simulated meteoric water solution was prepared by bubbling DI with air overnight to ensure equilibration with atmospheric gases. The sequential leaching experiment (large column experiment) also included OSPW collected from an oil sands mine as an input solution (field OSPW). All input solutions were vacuum filtered through 0.45 μm cellulose filter paper (Whatman acetate membranes, GE Healthcare, USA) to remove any precipitated solids, and transferred to clean acid-washed amber glass media bottles. The solutions were pumped in an upward direction to avoid gravity drainage through the columns. The peristaltic pumps were calibrated to achieve approximated flow rates of 49 and 460 mL d^{-1} for the small columns and large column, respectively. Column discharge was monitored over time and tracer tests were performed to determine pore water velocity, column hydrodynamic properties (i.e., dispersivity and porosity), and residence time. A mylar balloon containing 100% (v/v) $N_{2(g)}$ was attached to the input solution reservoir during the field OSPW input phase of the large column experiment to limit $O_{2(aq)}$ concentrations.

Table 3.1. Target input solution composition.

Parameter	Units	DI[a]	OSPW[b]	OSPW[c]	ARD[d]
pH		7.2	8.6	8.86	2.0
Na	mg L^{-1}	2.97	1060	1160	200
Mg	mg L^{-1}	0.02	20	6.54	200
K	mg L^{-1}	0.2	20	12.5	0.4
Ca	mg L^{-1}	0.25	12.5	5.96	400
HCO_3	mg L^{-1}	13.4	870	1120	0
Cl	mg L^{-1}	0.41	1100	900*	150
SO_4	mg L^{-1}	0.25	200	592	10000
Fe	mg L^{-1}	0	0	0	2460

*Cl concentration was assessed using charge balance error (CBE) calculated by PHREEQCi

[a]DI: Deionized water

[b]OSPW: synthetic oil sand process-affected water

[c]OSPW: Oil sand process-affected water

[d]ARD: Acid rock drainage

3.2. Aqueous-Phase Analyses

Column influent and effluent samples were collected weekly from the input solution reservoir and the effluent sampling cells. Daily effluent sampling was also performed during the first pore volume to capture initial element leaching. Profile sampling of the column pore water was performed every two months for the small columns and monthly for the large column. These frequencies were chosen for profile sampling to limit disturbances to the column flow regime. All water samples were collected into clean all-plastic polypropylene (PP) syringes (Norm-Ject®, Henke-Sass Wolf GmbH, Germany).

Pore water pH, reduction–oxidation potential (Eh), EC, temperature, and alkalinity were measured immediately following sample collection. Before each measurement, calibration of the pH probe (Orion 8156BNUWP ROSS Ultra, Thermo Fisher Scientific, USA) was done using a 3-point calibration with NIST traceable pH 4, 7, and 10 buffer solutions. The Eh electrode (Orion 9678BNWP Sureflow, Thermo Fisher Scientific, USA) performance was checked by Light's

(Light, 1972) and ZoBell's (Nordstrom, 1977; ZoBell, 1946) solutions (Ricca Chemical Co., USA). A standard solution of NaCl with 1413 μS cm^{-1} (Thermo Scientific, USA) was used to calibrate the EC electrode. The pH and Eh measurements were performed on unfiltered samples, and EC and alkalinity measurements were performed on samples filtered through 0.45 μm polyethersulfone (PES) syringe filter membranes (Minisart, Sartorius AG, Germany). Electrode performance (pH, Eh, EC) was checked between each measurement, and re-calibration was completed as required. Alkalinity was determined by titration with 0.16 N or 1.6 N H_2SO_4 (Hach Co., USA) to the bromocresol green/methyl red endpoint (Ricca Chemical Co., USA).

Samples for quantification of inorganic anions, major cations, and trace elements were passed through 0.45 μm, 0.2 μm, and 0.1 μm PES filter membranes (Minisart, Sartorius AG, Germany), respectively, and stored in high-density polyethylene (HDPE) bottles (Nalge Nunc International Corp., USA). Samples for cations and trace element analyses were acidified to pH < 2 using concentrated trace metal grade HNO_3 (OmniTrace, EMD Millipore, USA). All samples (inorganic anions, cations, trace elements) were kept at 4 °C until analysis. Analysis of major cations and trace elements was performed by inductively coupled plasma–optical emission spectrometry (ICP-OES; SPECTROBLUE, Spectro analytical instruments, Germany), and inductively coupled plasma–mass spectrometry (ICP-MS; NexION 300D). Major anion concentrations were measured by ion chromatography (IC; ICS2100; Dionex Corporation).

3.3. Solid-Phase Analyses

Samples of fluid petroleum coke solids were collected during column setup for physical, chemical, and mineralogical analyses. Two samples from each small column (n =12) were collected at 0.1 m intervals from the large column (n = 5). These samples were sealed in 50 mL PE centrifuge tubes and stored at −20 °C until analysis.

3.3.1. Specific Surface Area Analyses

The SSA was determined using Brunauer-Emmett-Teller N_2 adsorption isotherms, utilizing a BET ASAP 2020 surface area analyzer (Micromeritics, Georgia, USA; Brunauer et al., 1938). Also, the Barrett-Joyncer-Halenda (BJH) method was used to calculate adsorption and desorption of surface area, pore volume, and pore size. Samples were heated 60 °C for 24 h to remove any moisture and absorbed gases on the coke particle surface prior to analyses.

3.3.2. Particle Size Distribution

Particle size distributions (PSD) for dry coke, slurry coke, and acid-washed sand were determined by passing the samples through standard test sieves arranged in descending order of mesh size, based on ASTM D422–63. For each sample (i.e., acid-washed sand, dry and slurry coke), 400 g of sample was weighed before putting the sample on a shaker. Samples were shaken for 20 min, and the mass retained in each sieve was weighed to determine the PSD using percent passing by mass.

3.3.3. Electron Microscopy

Scanning electron microscopy (SEM; Hitachi FE-SEM SU8010, Japan) was performed on the bulk freeze-dried samples mounted on carbon tape without coating, using a 3 kV acceleration voltage to capture the micro-scale morphology of coke particles. Electron microprobe analysis (EMPA; JEOL JXA-8600 Superprobe Microanalyzer, Japan) was used to investigate the internal chemical composition of discrete particles hosted within coke prepared as thin sections. Thin sections were coated with a 200 Å carbon layer using the JEOL JEE-4X carbon vacuum evaporator prior to EMPA analysis.

3.3.4. Cation Exchange Capacity Analysis

The cation exchange capacity (CEC) and exchangeable cation composition are important factors in water-sediment interactions. Methylene blue has a high binding affinity compared with inorganic cations (e.g. AgTU, LiCl), as the polar and non-polar components make methylene blue able to bind well with the surface. Also, the methylene blue test is the method least impacted by the presence of carbonate mineral phases (Holden et al., 2012). CEC was evaluated for oven-dried fresh dry ($n = 4$) and slurry coke ($n = 4$) using combined methods described by Holden et al. (2012), Kaminsky (2014), and Santamarina et al. (2002; Appendix C).

3.3.5. pH Point of Zero Charge

The pH point of zero charge (pH_{PZC}) for dry and slurry coke particles was determined using combined solid addition methods described by Pourrezaei et al. (2014), Alam et al. (2016), and Robertson et al. (2019). Prior to the experiment, 1 L 0.1 N NaCl, as a background electrolyte solution, was purged with $N_{2(g)}$ for 24 h in an anaerobic chamber (Coy Laboratory Products, USA; ≤5 vol% $H_{2(g)}$, balance $N_{2(g)}$) to remove the buffering effect of dissolved CO_2 in solution (Alam et al., 2016). For each sample, nine 40 mL amber vials were labeled with the sample name and desired

pH (2, 3, 4, 5, 6, 7, 8, 9, 10). Each amber bottle was filled with 25 mL purged 0.1 M NaCl solution, and the pH was adjusted with a small volume of 0.1 or 1 M HCl or NaOH. The pH for each amber vial was measured again and recorded after 1 h to ensure they had reached equilibrium. Adding 0.1 N HCl or NaOH was continued until the actual pH was within ± 0.3 of the target pH. Then, 0.5 g gently-ground, homogenized, and air-dried coke was added to each amber vial, and the amber bottles were sealed immediately with gas-impermeable rubber-lined septa. All steps were performed in an anoxic chamber, except weighing. Amber vials were removed from the anaerobic chamber and placed on an orbital shaker at 100 rpm for 48 h, after which the pH of suspension was measured again. The change in pH (ΔpH) versus initial pH (pH_0) was plotted, and the point of intersection of the curve with the x-axis (pH_0) is associated with pH_{PZC} (Pourrezaei et al., 2014; Alam et al., 2016).

3.3.6. Elemental Analyses

Total C and S were determined by combustion and infrared detection of evolved CO_2 and SO_2 (CS230 Carbon/Sulfur Determinator, LECO Corporation, USA). Concentrations of major and trace elements were quantified by Li borate fusion digestion followed by ICP-OES and ICP-MS, respectively. A modified aqua regia (1:1:1 HNO_3:HCl:DI) digestion for 1 h at 80 °C followed by ICP-MS was used to determine As and Se concentrations.

3.4. Data Analysis

3.4.1. Statistical Methods

The Pearson correlation was performed on bulk elemental results; correlation matrixes were generated using the following procedure to examine the significance and robustness of correlations. Prior to analysis, a center log-ratio transformation was carried out; the individual element concentration was divided by the geometric mean of all elements for the same sample. Then, the log10 of the result was calculated. Such a transformation of values is used to make an open data set with the sum of elemental concentrations equal to zero. All statistical analyses were executed on all submitted samples (n = 17) and results were reported for the same sample size (n = 35) and significance level of 5% (i.e., ρ = 0.05).

3.4.2. Transport Parameters

A tracer test using a conservative tracer with initial concentration of zero throughout the system ($C_o = 0$) was carried out on the columns to determine the pore water velocity, dispersivity coefficient, porosity, and residence time. A tracer solution containing 100 mg L^{-1} Br^- (from NaBr) was prepared, and the bromide electrode (Orion 9635BNWP, Thermo Scientific, USA) performance and sensitivity was checked prior to measurements. A series of different concentrations of the Br^- solution was prepared (0, 2.5, 3, 5, 10, 20, 25, 30, 50, 80, 90, 100 and 200 mg L^{-1}), and a 10-fold difference in concentration should result in a difference of 57 ± 3 mV. Based on this test, the probe sensitivity was determined to be 2.5 mg L^{-1}, which means ±2.5% is the electrode sensitivity. A breakthrough curve is the ratio of C/C_o versus the number of passed pore volumes of effluent collected (or time). The column hydraulic parameters (i.e., dispersivity) and average linear pore-water velocity were determined by solving the equation 3.1 obtained from Genuchten (1982) which was written and solved for the Br breakthrough curve in MATLAB.

$$\frac{\partial C}{\partial t} = D\,\frac{\partial^2 C}{\partial x^2} - Vw\,\frac{\partial C}{\partial x} \tag{3.1}$$

where D is the hydrodynamic dispersion coefficient ($L^2\ T^{-1}$), which could be measured with equation 3.2, and V_w is the average linear pore water velocity ($L\ T^{-1}$).

$$D = \alpha V_w + D^* \tag{3.2}$$

In equation 3.2, D^* is the effective diffusion coefficient of molecule ($L^2\ T^{-1}$) and calculated with $D^* = \omega * D_d$,where ω is coefficient that is related to the tortuosity and here is considered 0.7 based on Perkins and Johnston, 1963 study for uniform sand column. The first term of equation 3.2 is the mechanical dispersion, where α is the dispersivity coefficient (L).

The column discharge rates were monitored throughout the leaching experiment and tracer test by weighing the waste container over time, as this is an important factor in measuring cumulative mass release. The residence time for the columns was determined by finding the time associated with $C/C_o = 0.5$, which means the Br^- concentration in the column effluent is equal to half of the influent Br^- concentration. Pore volume (PV) calculated by multiplying the residence time (T) by the discharge volume ($L^3\ T^{-1}$) over associated time of the residence time. Finally, the effective porosity was calculated using equation 3.3, dividing PV over the total volume of column.

$$n_e = \frac{PV}{V_T} \tag{3.3}$$

3.4.3. Geochemical Modelling

Thermodynamic equilibrium modeling using PHREEQCi (version 3.6.1–15000; Parkhurst & Appelo, 2013) with a modified Minteq version 3.1 database (Gustafsson, 2018) was performed to assess data quality, saturation indices, and trace element speciation occurring in the pore water.

Saturation indices were determined from the modeling output to indicate which mineral phases are most likely present in or out of solution. The charge balance error (CBE) calculated by equation 3.4 inside the PHREEQC model is an indication of data quality, where a CBE of less than 5% is generally acceptable.

$$CBE\ (\%) = \frac{(\sum cations + \sum anions)}{(\sum cations - \sum anions)} * 100 \qquad (3.4)$$

Access to a corrected thermodynamic database for various reactions that can occur is important in order to understand the water chemistry of V. The redox reactions and associated equilibrium constants were obtained from Allison et al. (1991) and Wanty and Goldhaber (1992), as these two databases were in good agreement.

Under strong anoxic conditions, like sulfide-containing sediments or wetlands, V(III) is expected to be stable. Assuming similar water chemistry between V(III) and Fe^{3+} (Gustafsson, 2019), thermodynamic data for V(III) hydrolysis were chosen from Buglyó et al. (2005).

Depending on the pH, V(V) will occur in a different coordination environment. At low pH (pH < 3.6), V(V) presents as VO_2^+, while at high pH, it presents as the $H_nVO_4^{(3-n)-}$ ion (i.e., HVO_4^{2-}). Also, V has a tendency to form poly-nuclear species at concentrations exceeding 100 µM that may consist of up to 10 V atoms (V_2, V_3, V_4, V_5, V_6, and V_{10}). Mononuclear and poly-nuclear V reactions and equilibrium constants were considered from Larson (1995), Cruywagen et al. (1996), Elvingson et al. (1996), Cruywagen (1999), Smith et al. (2004), and McCann et al. (2015, 2013; Appendix D).

3.4.4. Geophysical Modeling

This section describes the low-frequency geoelectrical methods (i.e., SP and ER) and their application in solving practical hydrogeological problems. These techniques can be used to monitor the interaction of pore water minerals and to evaluate hydrodynamic parameters. These methods should be used in parallel with additional data from other in situ tests (e.g., chemical analysis of porewater) to help verify the geoelectrical results. Electrical geophysical computer modeling falls into two categories: (i) forward and (ii) inverse modeling. Forward modeling is the

simulation of a response, given a set number of parameters, to identify a solution. Forward modeling is usually solved numerically using finite-difference or finite-element methods (i.e., COMSOL Multiphysics). Inverse modeling evaluates the optimal parameters given a specific acquired dataset.

The geometric factor (K_g) for the ring and lateral (A, B, C, and D; Wenner array configuration) positions were calculated in COMSOL Multiphysics assuming a constant resistivity throughout the column and current of 1 A. The inversion model, given the measured voltage and current ($\frac{\Delta V}{I}$) over time with calculated geometric factors, was carried out by multiplying the geometric factor by the ratio of voltage over current to calculate the apparent resistivity (ohm m). The calculated apparent resistivity was plotted over time for each individual ring. Based on midpoints theory, the time for the apparent resistivity to reach the median value was determined for each individual ring during the first tracer test (including the injection and decay). The average linear velocity was measured using a linear regression of locations vs. mid-point time for the individual ring.

Forward 1-D time dependent modeling was performed in COMSOL Multiphysics using the direct currents (AC/DC) module. Chemical species, including Na^+, Br^-, SO_4^{2-}, Al^{3+}, Fe^{2+}, Ca^{2+}, Mg^{2+}, and alkalinity were considered in the transport model—transport equation 3.5 was solved for each individual species. Their associated diffusion coefficients were obtained from Yuan-Hui and Gregory (1974). Also, as coke is a reactive material, the reaction rates for individual species (R_i) were determined by finding the best fit to measured concentrations in the column effluent (Appendix A).

$$\frac{\partial C}{\partial t} + \nabla . J_i + u . \nabla C_i = R_i \qquad (3.5)$$

where Ji is hydrodynamic dispersion and is equal to $-D_i * \nabla Ci$, u is the pore water velocity. The transport equation (equation 3.5) was solved as a function of time for these chemical species, and their aqueous concentrations were converted to EC using the Kohlrausch's law of independent ionic mobility (equation 3.6); where the EC of a solution is equal to the sum of EC of all aqueous species in the solution. The Kohlrausch's law covers complete and partial ionisation that typically represented by strong and weak electrolytes, respectively. Thus, the salt-type solute for this experiment was assumed as a strong electrolyte and the molar conductivities as a function of electrolyte concentration for each individual species is linear. In order to measure the EC of

individual species, the concentration of the individual species (M m^{-3}), νi, was multiplied by the molar ionic conductivity (mS m^2 M^{-1}), λi, obtained from Adamson (1973).

$$\Lambda^{\circ}_{m} = \sum_i \upsilon_i * \lambda_i \quad (3.6)$$

Finally, Archie's law (Archie, 1942) is used to calculate the apparent resistivity of individual ring with porosity and EC of the pore fluid (Equation 3.7). The fitting parameter m, could be estimated based on initial values of R, Rw and porosity (φ).

$$\sigma_0 = \sigma_w \varphi^m \quad (3.7)$$

3.4.5. Cumulative Mass Release Calculations

Cumulative mass release calculations were performed to determine the metal leaching for coke under different geochemical conditions (including DI, OSPW, and ARD) using equation 3.8.

$$\Delta M_j = \sum M_{jOutflow} - \sum M_{jInflow} \quad (3.8)$$

where $M_{jOutflow}$ and M_{jIflow} are masses for a given solute, j, were calculated with equation 3.9 as the product of water volume (L), dV_i, over a given sampling interval, i, and the mean concentration (µg L^{-1}) of the solute, $\overline{m_{j,i}}$, over that time interval.

$$M_{j,i} = dV_i \, \overline{m_{j,i}} \quad (3.9)$$

The cumulative mass, $\sum M_j$, in and out were determined with equation 3.10 by summing $M_{j,i}$ over time:

$$\sum M_j = \sum_{i=1}^{n} M_{j,i} \quad (3.10)$$

CHAPTER 4: RESULTS AND DISCUSSION

4.1. Physical Characteristics

Coke solids exhibit a spherical to sub-spherical shape and typically range from 40 to 500 μm in diameter (Figure 4.1). Given its uniform spherical shape with a sandy texture and the measured PSD for slurry and dry coke samples, coke can be classified as a moderately well-sorted sand with low fines (uniformity coefficient [CU] ~2; Table 4.1).

Coke particles display fractures and broken pieces that may result from heating and cooling cycles in the coking process or during slurry preparation when hot coke particles are mixed with OSPW prior to hydrotransport (Figure 4.1). These features (i.e., fracturing and broken pieces) are attributed to the thermal shock on coke particles. Also, some attached particles observed on the surface of slurry coke particles might have settled on the coke surface during slurry preparation or hydrotransport. More cracks and broken pieces were observed on slurry coke samples compared with dry coke samples (Figure 4.1), suggesting that slurry coke preparation promotes fracturing, broken particles, and particle attachment on the coke surface.

Table 4.1. Physical properties of acid-washed sand (AWS) and coke.

Source	d10 (mm)	d60 (mm)	Cu[a]	SSA[b] (m^2 g^{-1})	pH_{PZC}[c]	CEC[d] (meq 100 g^{-1})
DC[e]	0.1	0.27	2.7	0.25 ± 0.18	6.65 ± 0.17	0.032 ± 0.013
SC[f]	0.12	0.27	2.25	6.5 ± 0.48	7.19 ± 0.17	0.203 ± 0.007
AWS[g]	0.3	0.60	2	–	–	–

[a]Cu: Uniformity coefficient (d60/d10)

[b]SSA: Specific surface area

[c]pHPZC: pH point of zero charge

[d]CEC: Cation exchange capacity

[e]DC: Dry coke

[f]SC: Slurry coke

[g]AWS: Acid washed sand

Although the SSA for coke samples is generally low, more fractured and broken pieces and attached particles on the slurry coke surface compared with the dry coke samples resulted in higher

SSA for slurry coke (Table 4.1). The measured SSA for coke is generally consistent with previously reported values of 4.5 ± 2.8 $m^2 g^{-1}$ (Nesbitt et al., 2017), 6 $m^2 g^{-1}$ (Zubot et al., 2012), 8 $m^2 g^{-1}$ (Pourrezaei et al., 2014), 10 $m^2 g^{-1}$ (Har, 1981), and 11 $m^2 g^{-1}$ (Fedorak & Coy, 2006) for similar samples collected from coke deposits or coker units.

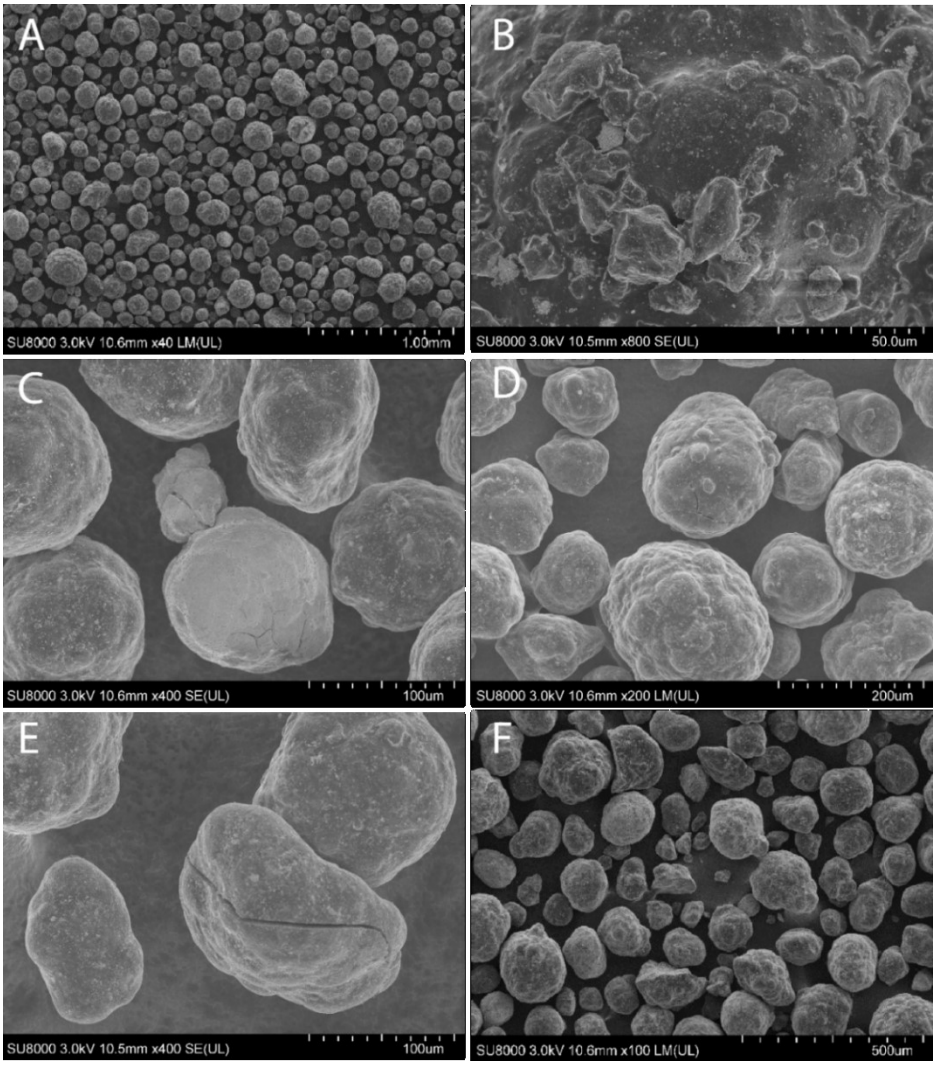

Figure 4.1. Scanning electron microprobe (SEM) images of fluid petroleum coke; (a) dry coke, (b) slurry coke, (c, d) dry coke, and (e, f) slurry coke.

The average pH_{PCZ} values for fresh dry and slurry coke were 6.65 ± 0.17 and 7.19 ± 0.17, respectively (Table 4.1, Appendix E). These values were consistent with previous studies of oil sands fluid petroleum coke by Pourrezaei et al. (2014), Nesbitt et al. (2018), and Robertson et al. (2019), yet substantially higher than the pH_{PCZ} of 2.5 reported by Alam et al. (2016). Coke particles exhibit net positive and net negative surface charges when in contact with solution having a pH

below and above the pH_{PCZ} of 6.7–7.2, respectively. This has implications for the mobility of aqueous metal ions in coke deposits and in mine closure landscapes.

4.2. Chemical Characteristics

The chemical composition of fluid petroleum coke samples is dominated by C (79.25 ± 1.34 wt%) and S (8.00 ± 0.13 wt%), which are associated with bitumen (Figure 4.2, Appendix F). Elevated concentrations of several major elements including Si (12760 ± 945 mg kg^{-1}), Al (7000 ± 180 mg kg^{-1}), Fe (5200 ± 200 mg kg^{-1}), Ti (1400 ± 70 mg kg^{-1}), Ca (2000 ± 180 mg kg^{-1}), K (1060 ± 45 mg kg^{-1}), and Mg (790 ± 40 mg kg^{-1}) are largely attributed to entrained solids (Nesbitt et al., 2017). Potentially hazardous trace metals including V (1380 ± 45 mg kg^{-1}), Ni (540 ± 18 mg kg^{-1}), and Mo (75.1 ± 3.5 mg kg^{-1}) were also detected. Har (1981) reported volatile elements including H (1.5–1.67 wt%), N (1.3–1.6 wt%), and O (2.3–2.5 wt%) which are lost on ignition. Very similar volatile element concentrations also have been reported previously by Chung (1996) and Kessler & Hendry (2006).

Solid-phase concentrations of major and trace elements are generally consistent with previous studies of fluid petroleum coke (Table 4.2). Exceptions include Ni concentrations previously reported by Zubot et al. (2012) and Mo concentrations previously reported by Nesbitt et al. (2017) and Zubot et al. (2012). Nickel concentrations were 513–573 mg kg^{-1} for samples analyzed in this study, while Zubot et al. (2012) reported 35–68 mg kg^{-1}. Similarly, Mo concentrations were 71–85 mg kg^{-1} in this study compared to 7.6–29 mg kg^{-1} reported by Zubot et al. (2012) and Nesbitt et al. (2017). Some previous studies analyzed samples collected immediately from coker units or hydrotransport lines (Jack et al., 1979; Har, 1981; Zubot et al., 2012), whereas other studies analyzed samples from coke deposits subjected to extended periods of weathering (Chung, 1996; Kessler & Hendry, 2006; Nesbitt et al., 2017). Variability in reported values could result from differences in bitumen feedstock, sampling location, weathering extent, or analytical methods.

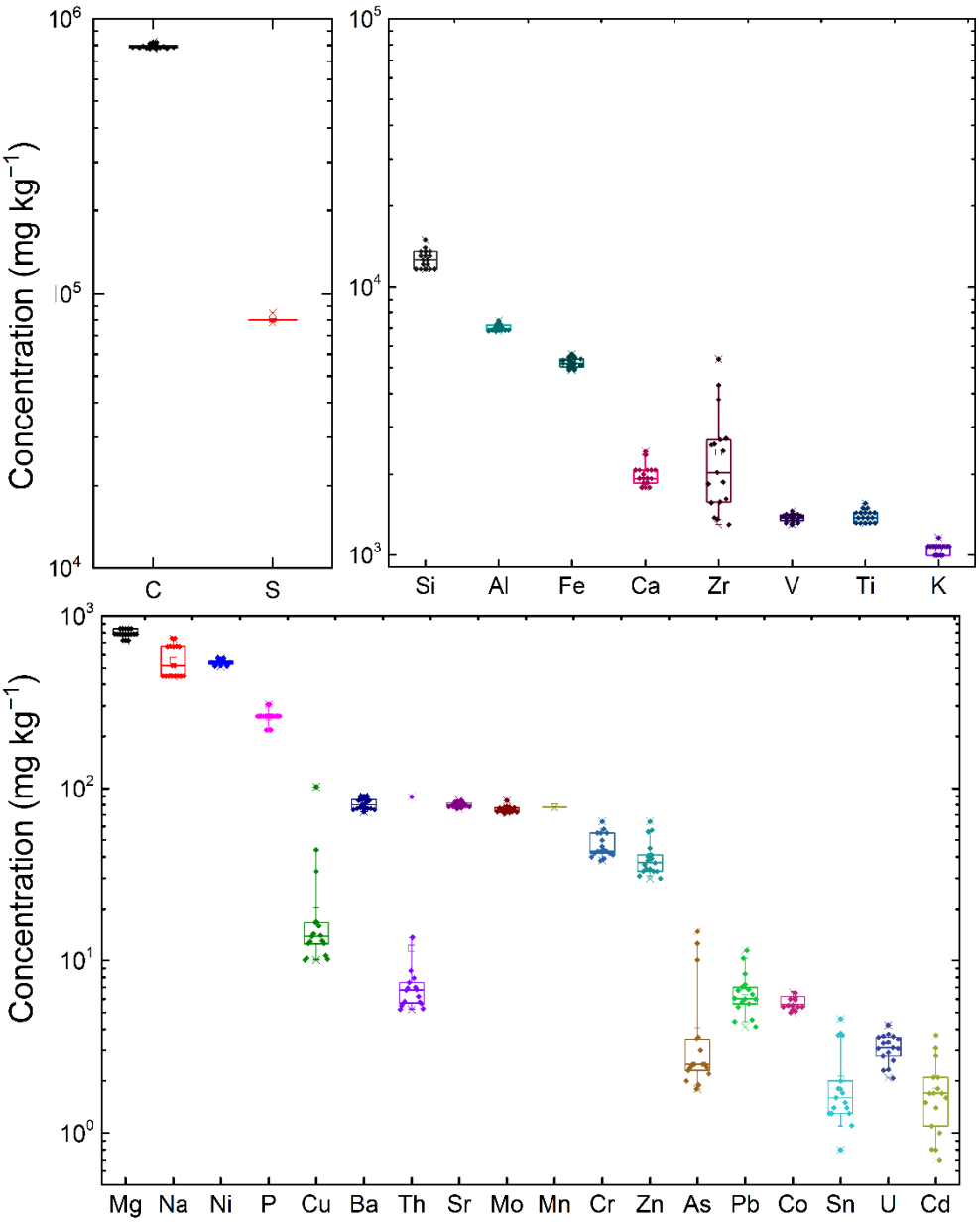

Figure 4.2. Bulk elemental analyses for elements in fluid petroleum coke. Box lines define 25th, 50th, and 75th percentiles; lower and upper whiskers define 10th and 90th percentiles.

Coke particles consisted of a series of sub-spherical, successive concentric layers. Each concentric layer was composed of two zones: (i) an inner region measuring 5–10 µm thick; and (ii) an outer margin measuring 1–5 µm thick. In addition, the outer region was a lighter color compared with the inner region in backscattered electron (BSE) images (Figure 4.3), which suggests more elements with a higher atomic number are present.

Table 4.2. Summary of selected elemental contents for fluid petroleum coke samples collected from coker units and field deposits.

Source	*n*	C (wt.%)	S (wt.%)	V (mg kg^{-1})	Ni (mg kg^{-1})	Mo (mg kg^{-1})
coker[a]	1	82	3.3	1600	660	121
coker[b]	10	79–82	5.8–7.1	1500–1900	550–720	–
deposit[c]	5	80–84	6.1–-6.9	1600–1766	475–520	66–100
deposit[d]	3	78–84	7.0–8.1	1134–1440	470–590	67–94
coker[e]	29	75–89	5.6–7.6	1000–1400	35–68	12–29
deposit[f]	28	80–89	6.4–7.6	1000–1500	130–460	7.6–23
coker[g]	11	78–82	7.8–8.4	1300–1400	510–570	71–78
deposit[g]	6	74–82	7.9–8.1	1400–1500	520–570	72–85

[a]Jack et al. (1979)
[b]Har (1981)
[c]Chung (1996)
[d]Kessler & Hendry (2006)
[e]Zubot et al. (2012)
[f]Nesbitt et al. (2017)
[g]This study

Energy dispersive X-ray (EDX) spectra of the inner and outer margins of individual layers revealed that the chemistry of the inner region of individual layers is dominated by S, Al, and Si, while the outer margin of these layers have elevated K, Ca, Ti, V, Mn, and Fe concentrations (Figure 4.3). Successive concentric layers with different chemistry were reported by Nesbitt et al. (2017). The coking cycle process, including material adding and thermal decomposition of organic components, resulted in successive concentric layers with different chemistry (Zubot et al., 2012; Nesbitt et al., 2017).

Bulk C and S concentrations exhibited a strong positive correlation (r = 0.97). This positive correlation was attributed to the fact that the chemical composition of coke is dominated by C and S. Statistical analysis revealed a strong positive correlation between V and Ni with both C (r = 0.92) and S (r = 0.95). The correlation of V and Ni with C is attributed to the prevalence of V(IV) and Ni(II) porphyrins in fluid coke samples (Nesbitt & Lindsay, 2017; Nesbitt et al., 2018, 2017). Also, the correlation between C, S, and metals is consistent with Nesbitt et al. (2017). There was also a strong positive correlation between Mo, C (r = 0.88), and S (r = 0.90) within coke bulk concentrations.

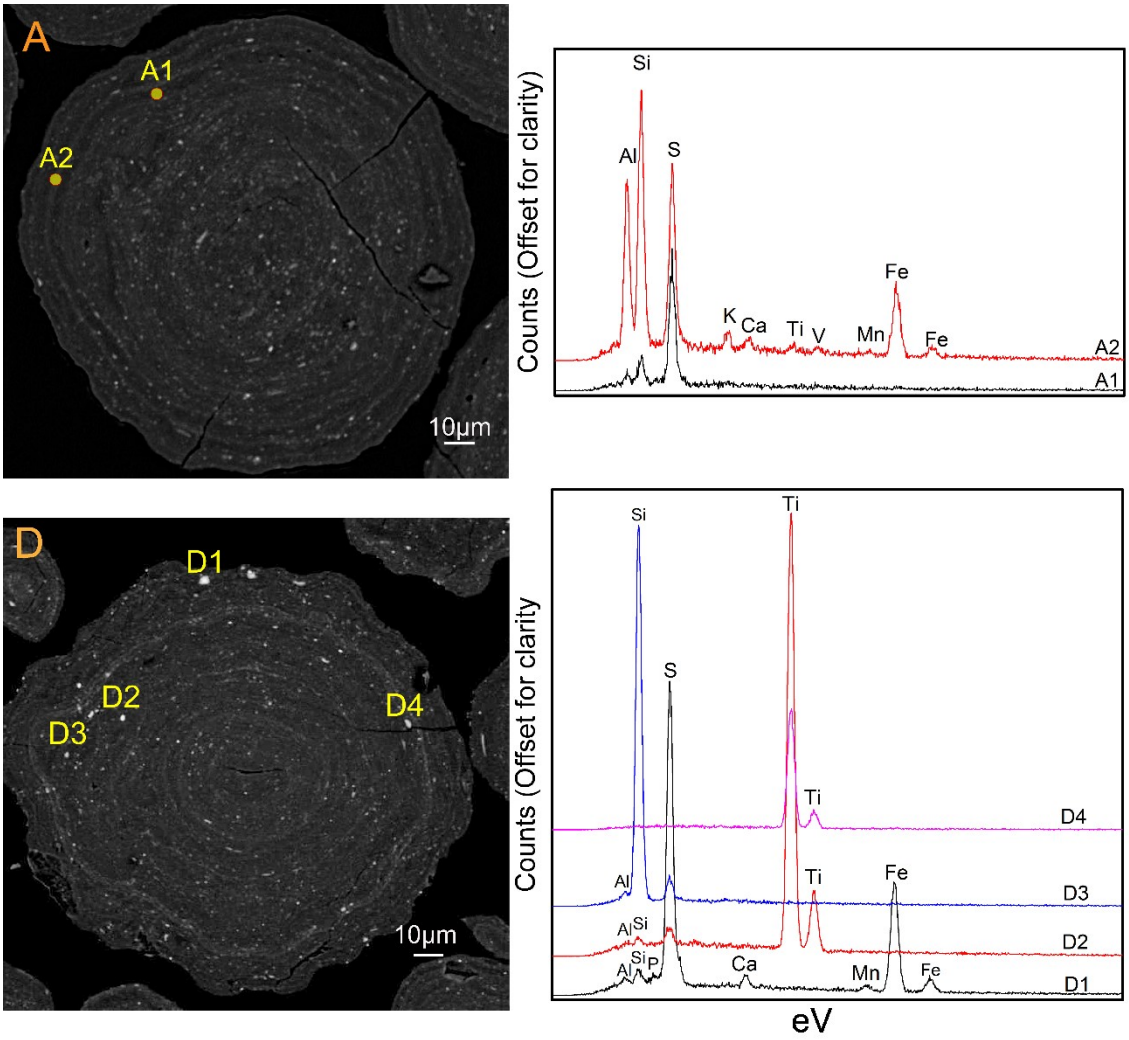

Figure 4.3. Top: Backscattered electron (BSE) images of fluid coke particles in thin section. Yellow dots and labels denote the energy dispersive X-ray (EDX) spectra for sample A (top) and sample D (bottom). Yellow dots indicate locations of the obtained spectra while the points without a red dot spectra was obtained for that specific mineral.

Iron and Ti exhibited a strong positive correlation ($r = 0.88$), which indicates their association with oxide phases. Obtained EDX spectra at the outer margin of individual layers exhibited relatively higher Ti and Fe content than the inner regions. In addition, discrete grains of pyrite (FeS_2; D1) and titanium oxide like rutile or anatase (i.e., TiO_2; D2, D4) were observed within coke particles (Figure 4.3). The presence of a Ti-bearing phase throughout the coke matrix was previously reported by Nesbitt et al. (2017). Regions with elevated concentration of co-located sub-micron Fe- and Ti-bearing phases within coke grains was reported by Nesbitt et al. (2017).

The presence of Fe- and Ti-bearing phases hosted in coke may act as adsorption sites for aqueous trace metals (Blackmore et al., 1996; Zubot et al., 2012).

Correlation between Si, Al, K, and Mg (r = 0.72–0.91) was attributed to their co-occurrence in entrained aluminosilicate phases within fluid petroleum coke particles. Si, Al, K, Ca, and Mg were detected through the obtained EDX spectra of coke particles (Figure 4.3). This is in agreement with Nesbitt et al. (2017) who showed that distinct Si-bearing particles and sub-micron sized particles containing Al, K, Mg, and Si have been reported. A high correlation between Ca and Sr (r = 0.75) was observed within bulk coke, and suggests the presence of carbonate minerals. The presence of carbonate minerals in fluid coke particles was also reported by Kessler & Hendry (2006) and Nesbitt et al. (2017). Elevated Al, Si, K, Ca, Ti, V, and Fe at the outer margin of individual layers compared with the inner margin could be attributed to material addition and coke surface coking during each cycle within the coker units.

4.3. Small Columns

4.3.1. Aqueous Geochemistry

The pH of the influent was relatively stable during the experiments, with a median value of 7.21, 8.60, and 2.04 for DI, OSPW, and ARD, respectively. Compared with the influent, the effluent pH declined for the DI solution, to 4.48–5.40 for dry coke and 4.70–6.40 for slurry coke. The pH of the OSPW effluent solution was 6.10–6.80 for dry coke and 6.10–6.90 for slurry coke. The pH of the ARD effluent solution was 1.90–2.60 and 1.90–3.30 for dry and slurry coke, respectively. The pH of the influent and effluent under ARD is generally similar except for the first two pore volumes for the column with slurry coke, which had a higher pH due to acid neutralization by the residual OSPW on the coke surface (Figure 4.4).

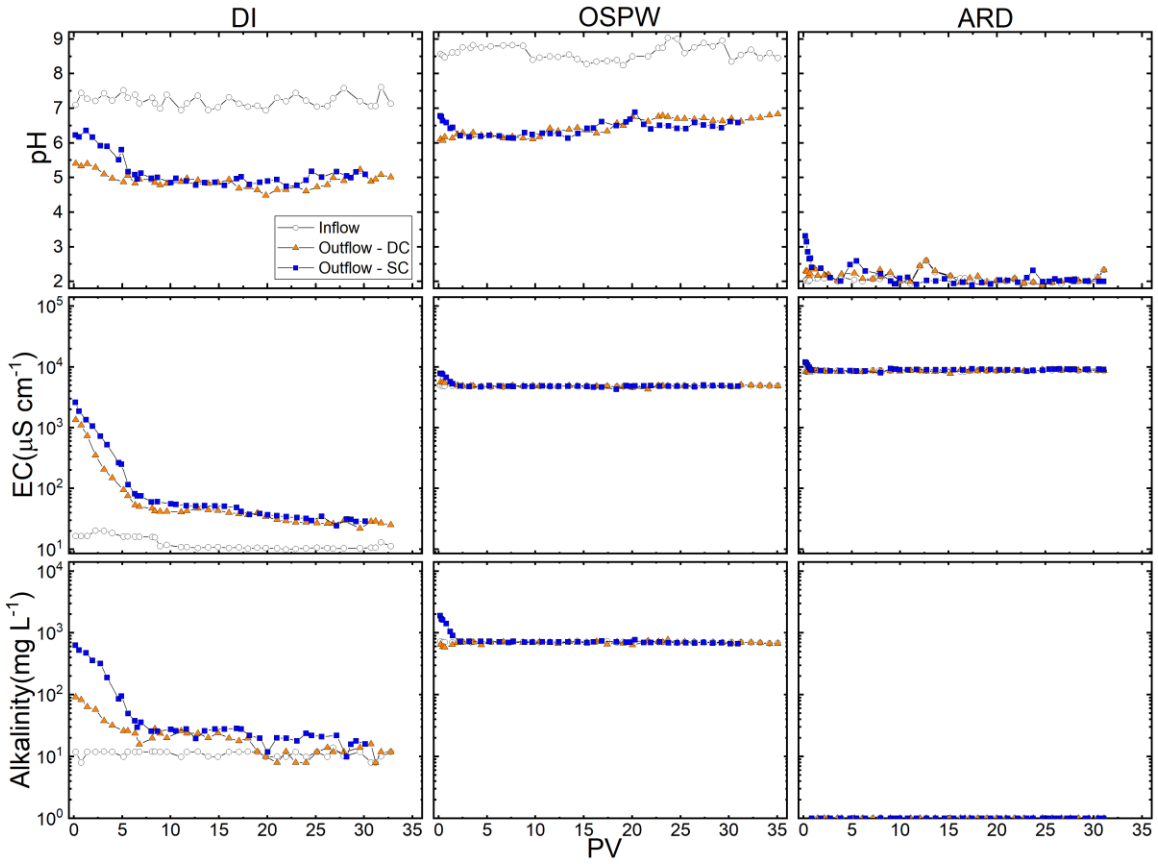

Figure 4.4. Influent (open symbol) and effluent (filled symbols) pH, electrical conductivity (EC), and alkalinity as a function of pore volume (PV) for the small columns experiment during deionized (DI), oil sand process-affected water (OSPW), and acid rock drainage (ARD) solutions. The orange triangles and blue squares represent dry coke and slurry coke, respectively. Units for alkalinity are mg L^{-1} as $CaCO_3$ and values plotted on the x-axis are equal to zero.

The pH reduction for the DI and OSPW solutions, along with the elevated Fe and S concentrations in the column effluent (Figure 4.5), suggested acid generation via Fe-S–bearing phase oxidation (i.e., pyrite). The presence of Fe-S–bearing phases was observed by EMPA (Figure 4.3) and reported previously by Kessler and Hendry (2006). Elevated concentrations of Ca, Mg, Sr, and Ba, in addition to a significantly positive correlation of Sr with Ca ($r = 0.37$), Mg ($r = 0.47$), and Ba ($r = 0.2$) in the effluent (Appendix G), correspond to the dissolution of carbonate minerals and is another indication of acid generation by coke. The pH reduction could lead to carbonate dissolution, therefore mobilizing and releasing associated elements such as Sr and Ca. The effluent pH of the columns gradually increased during the experiment with DI and OSPW

inputs for both dry and slurry coke, suggesting a decrease in the acid generation potential for coke (Figure 4.4).

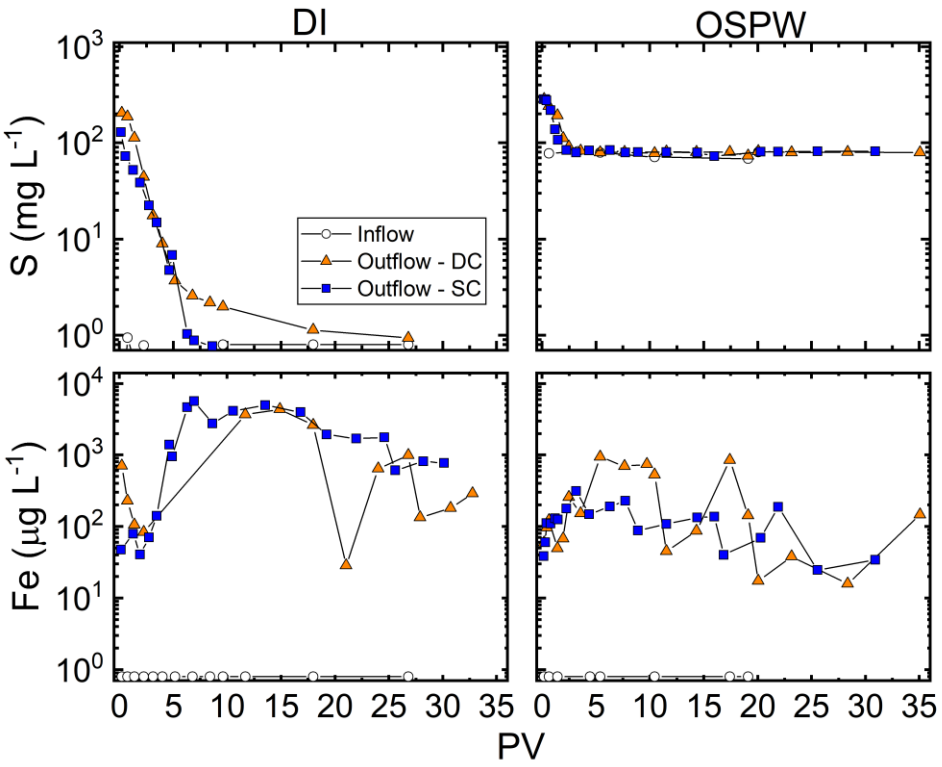

Figure 4.5. Influent (open symbol) and effluent (filled symbols) dissolved concentration of S and Fe as a function of pore volume (PV) for the small columns experiment during deionized (DI) and oil sand process-affected water (OSPW) solutions. The orange triangles and blue squares represent dry and slurry coke, respectively. Values plotted on the x-axis are equal to zero.

Thermodynamic modeling indicated that the initial pH of the effluent was strongly influenced by $CO_{2(g)}$ dissolution, associated with column setup, and washing of the residual OSPW from the slurry coke sample. The dissolved $CO_{2(g)}$ promoted carbonate dissolution and ion-exchange reactions over the first one to two pore volumes.

The influent EC and alkalinity of all solutions were relatively consistent over the experiment. The median EC for the influent solutions was 10.8 µS cm^{-1} for DI, 4.84 mS cm^{-1} for OSPW, and 8.69 mS cm^{-1} for ARD (Figure 4.4). The median alkalinity of the influent solutions was 11.9 mg L^{-1} for DI and 712 mg L^{-1} (as $CaCO_3$) for OSPW. The alkalinity could not be measured for the ARD solution since the pH was less than the pH of the bromocresol green–methyl red indicator.

The EC and alkalinity under DI input decreased rapidly for both dry and slurry coke over the first five pore volumes. The EC decreased from 1100 to 75.6 µS cm^{-1} and the alkalinity decreased from 83.2 to 26 mg L^{-1} for dry coke, and the EC decreased from 2620 to 251 µS cm^{-1} and alkalinity decreased from 634 to 95.0 mg L^{-1} (as $CaCO_3$) for slurry coke. Over the rest of the experiment, the EC and alkalinity under DI input gradually decreased to 21.9 µS cm^{-1} and 7.90 mg L^{-1} for dry coke and to 24.3 µS cm^{-1} and 9.90 mg L^{-1} for slurry coke, respectively (Figure 4.4).

Under OSPW input, the effluent EC was 4.30–5.57 for dry coke and 4.29–7.84 mS cm^{-1} for slurry coke. Under ARD input, the effluent EC was 7.76–9.02 and 7.97–11.98 mS cm^{-1} for dry and slurry coke, respectively. In addition, the effluent alkalinity was 582–777 mg L^{-1} for dry coke and 667–1890 mg L^{-1} for slurry coke under OSPW input. The residual OSPW in slurry coke from coke hydrotransport was released and flushed by the all of the water input compositions (DI, OSPW, and ARD). As a result, a higher EC and alkalinity was observed for the first several pore volumes of the experiment (Figure 4.4). In addition, the influent and effluent EC and alkalinity under OSPW and ARD conditions were generally similar after the first few pore volumes after residual OSPW was flushed from the coke surface. A significant positive correlation between pH and EC ($r = 0.34–0.46$) and alkalinity ($r = 0.79–0.88$) was observed under DI and OSPW input for both dry and slurry coke, which likely corresponded to OSPW flushing, acid generation, and carbonate dissolution from the system.

4.3.1.1. Vanadium

Column influent (DI, OSPW, or ARD) did not contain any metals of interest (V, Ni, or Mo). Dissolved V, Ni, and Mo concentrations in the column effluent varied between slurry and dry coke, and were generally higher for slurry coke than dry coke for all water input compositions (Figure 4.6). Higher SSA values for slurry compared with dry coke, and flushing of residual OSPW (containing V, Mo, and Ni; Appendix G) off the coke surface, resulted in a higher leaching potential for slurry coke. With DI input, the effluent V concentrations were 0–2.9 µg L^{-1} for dry coke and 11.1–6760 µg L^{-1} for slurry coke; for OSPW input, the effluent V concentrations were 0–17.0 µg L^{-1} for dry coke and 73.9–13700 µg L^{-1} for slurry coke; and for ARD input, effluent V concentrations were 56.4–3420 µg L^{-1} for dry coke and 65.9–22400 µg L^{-1} for slurry coke (Figure 4.6, Appendix G). Aqueous V concentrations followed the general order of ARD > OSPW > DI

and decreased over time after the rapid initial release of adsorbed V(V) from the surface of coke particles was followed by slower leaching of less mobile forms of V.

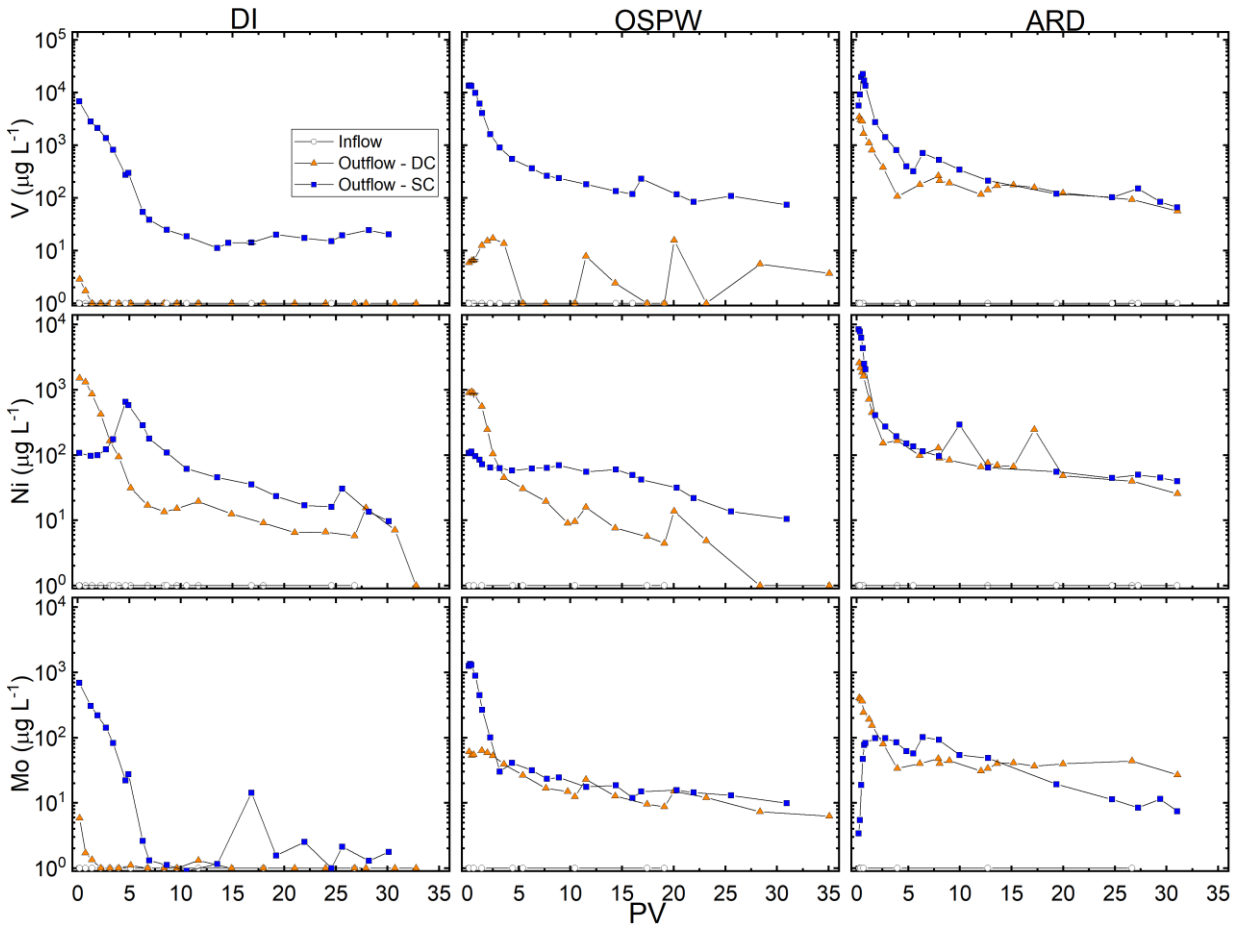

Figure 4.6. Influent (open symbol) and effluent (filled symbols) dissolved concentration of V, Mo, and Ni for the small columns under deionized (DI), oil sand process-affected water (OSPW), and acid rock drainage (ARD) as a function of pore volume (PV). Orange triangles and blue squares represent dry and slurry coke, respectively. Data on the x-axis are below the method detection limit and are assumed to be zero.

Thermodynamic geochemical modeling of porewater indicated a general undersaturated state for calcium vanadate and other V(V) phases. It also indicated that aqueous V species were dominated by $H_2VO_4^-$ with DI and OSPW input, but VO^{2+} was dominant under ARD input (Figure 4.7). Although geochemical modeling suggested the dominance of VO^{2+} with ARD input, oxidation of aqueous V(IV) to V(V) occurs rapidly under oxic conditions (Jensen-Fontaine, 2012). Thus, aqueous VO^{2+} species could be oxidized further to VO_2^+ by Fe(III) within ARD input. Poor agreement between the measured and theoretical Eh values is well established (Lindberg &

Runnells, 1984), and a slight decrease in input Eh values (±50 mV) shifted the model prediction to Fe(III) or Fe(II) as the dominant Fe oxidation state. The V oxidation state is sensitive to Eh values, especially with ARD input, since a slight change in Eh shifts the model prediction to V(V) or V(IV) as the dominant form. Based on dissolved V concentrations and geochemical modeling, poly-nuclear V species were not expected to form (Figure 4.7).

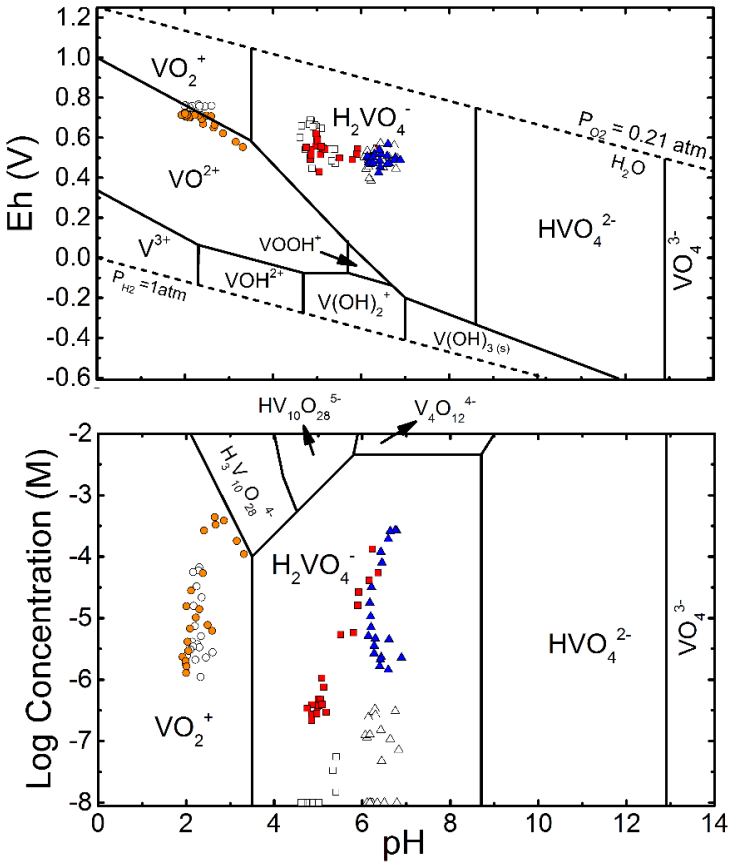

Figure 4.7. Pourbaix (Eh–pH) diagram for vanadium (top) and a predominance diagram showing aqueous V(V) speciation as a function of pH and total V concentration (bottom). All V aqueous species were assumed to be V(V) in the second figure. Squares, triangles, and circles represent data points for deionized (DI), oil sand process-affected water (OSPW), and acid rock drainage (ARD), respectively. Filled symbols represent slurry coke and empty symbols represent dry coke.

Variation in dissolved V concentrations in the column effluent under different water input compositions could be a result of pH-dependent sorption of V(V) onto the coke surface, or oxidation and dissolution of V complexes. According to porewater pH and pH_{PZC} for coke (6.7–7.2), the coke had a net positive surface charge with DI and ARD ($pH < pH_{PZC}$), but the surface charge was negative with OSPW ($pH > pH_{PZC}$). Therefore, the high ionic strength of ARD (I ~0.2)

and OSPW (I ~0.05), in addition to unfavorable conditions for V(V) adsorption on the coke surface including net surface charge and dominance of VO^{2+} (or VO_2^+) or $H_2VO_4^-$, mobilized V from the coke surface. Meanwhile, V mobility was limited and controlled by the adsorption of aqueous $H_2VO_4^-$ with DI input.

Cumulative V release calculations indicate that V leaching occurred under all water input compositions, however the leaching efficiency (the proportion of total leached to the bulk concentration) was relatively low, with a maximum 0.90% (12800 µg kg^{-1}) observed for slurry coke under ARD (Table 4.3, Appendix H). This is attributed to the large portion of V associated with porphyrin complexes (Nesbitt et al., 2017; Nesbitt and Lindsay, 2017), which are stable and resistant to weathering (Lewan & Maynard, 1982; Zuliani et al., 2016). Slurry coke exhibited a higher leaching potential than dry coke with 1.27 µg kg^{-1} compared with 5030 µg kg^{-1} with DI input, 70.5 µg kg^{-1} compared with 10100 µg kg^{-1} with OSPW input, and 3290 µg kg^{-1} compared with 12800 µg kg^{-1} with ARD (Table 4.3). In addition, over 50% of the cumulative V release occurred during the first five PV in experiments using dry and slurry coke with DI and ARD, and slurry coke with OSPW, representing the initial release of adsorbed V(V). While only 36% of cumulative V was released from the dry coke with OSPW given the slow leaching of rate of V (Figure 4.8, Appendix H).

Table 4.3. Cumulative mass release per kg of fluid petroleum coke for the small columns.

Elements	DI[a] (µg)		OSPW[b] (µg)		ARD[c] (µg)	
	DC[d]	SC[e]	DC	SC	DC	SC
V	1.27	5030	70.5	10100	3290	12800
Ni	1170	1330	760	651	2110	3550
Mo	3.82	514	276	869	758	610

[a]DI: Deionized water

[b]OSPW: Oil sand process-affected water

[c]ARD: Acid rock drainage

[d]DC: Dry coke

[e]SC: Slurry coke

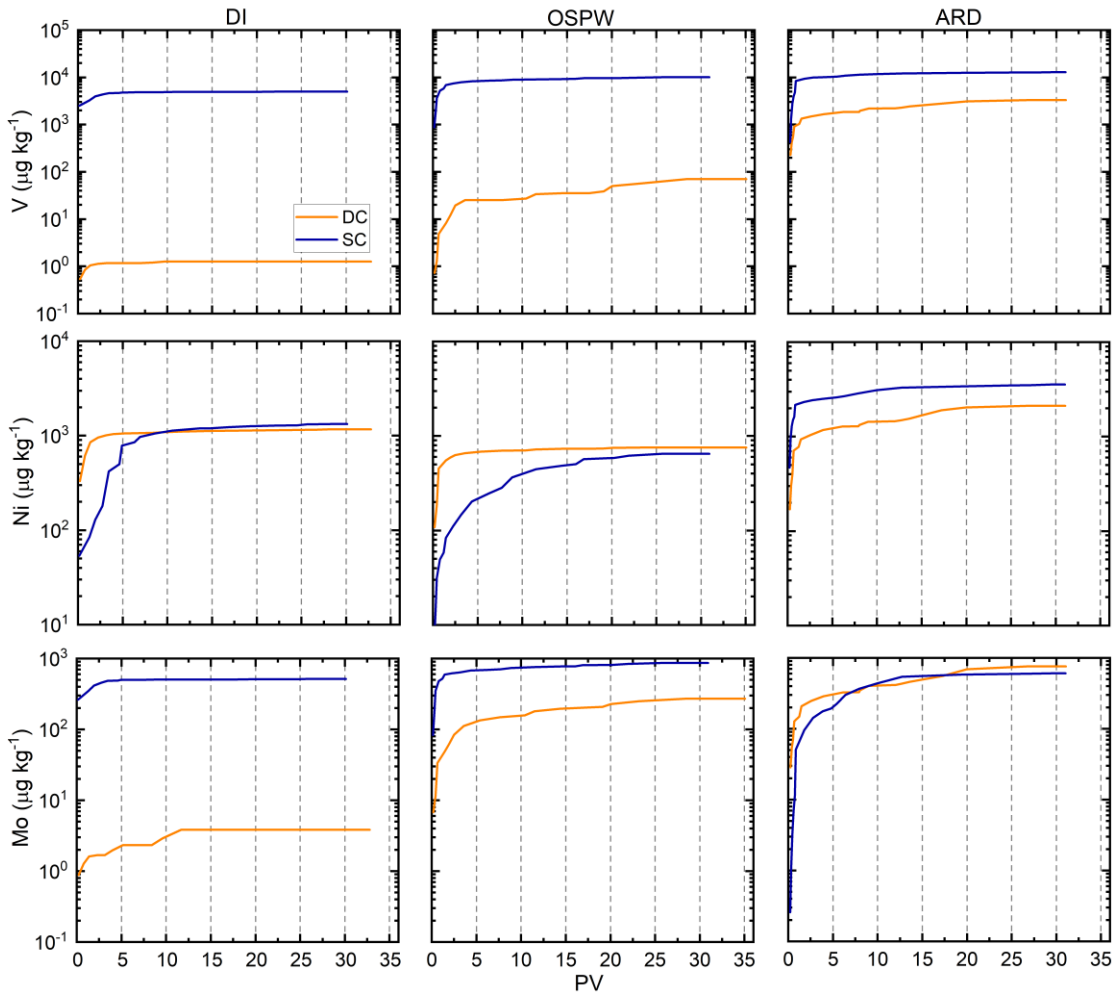

Figure 4.8. Cumulative mass release per kg of coke under deionized (DI), oil sand process-affected water (OSPW), and acid rock drainage (ARD) as function of pore volume (PV). Orange lines represent the dry coke; blue lines represent slurry coke.

4.3.1.2. Nickel

Nickel concentrations in column effluent with DI input were 0–1520 µg L^{-1} for dry coke and 9.70–655 µg L^{-1} for slurry coke, with OSPW input they were 0–929 µg L^{-1} for dry coke and 10.5–113 µg L^{-1} for slurry coke, and for ARD input they were 25.1–2600 µg L^{-1} for dry coke and 38.5–8460 µg L^{-1} for slurry coke (Figure 4.6, Appendix G). Aqueous Ni concentrations followed a general order of ARD > DI > OSPW and decreased over time with the rapid initial release of Ni from the surface of coke particles followed by slower leaching of less mobile and available forms of Ni.

Thermodynamic modeling indicated that with DI and OSPW input, Ni^{2+} was the dominant aqueous Ni species making up over 45% of aqueous Ni, while $NiSO_4^0$ and $NiHCO_3^+$ accounted

for the rest (Figure 4.9). However, during DI input, the proportions of $NiSO_4^0$ and $NiHCO_3^+$ species decreased rapidly over three pore volumes and shifted completely to Ni^{2+} while SO_4^{2-} and HCO_3^- (alkalinity) decreased (Figure 4.4 and 4.5). Speciation of aqueous Ni during ARD input showed that $NiSO_4^0$ and Ni^{2+} accounted for approximately 50% of aqueous Ni. Geochemical modeling showed that porewater was consistently undersaturated with respect to $NiO_{(S)}$, $NiCO_{3(S)}$, and $Ni(OH)_{2(S)}$. Therefore, these phases do not control the dissolved aqueous Ni concentration. Complexation of Ni with bicarbonate and sulfate forms non-ionic species ($NiHCO_3^+$, $NiSO_4^0$) which may increase Ni mobility and limit Ni sorption.

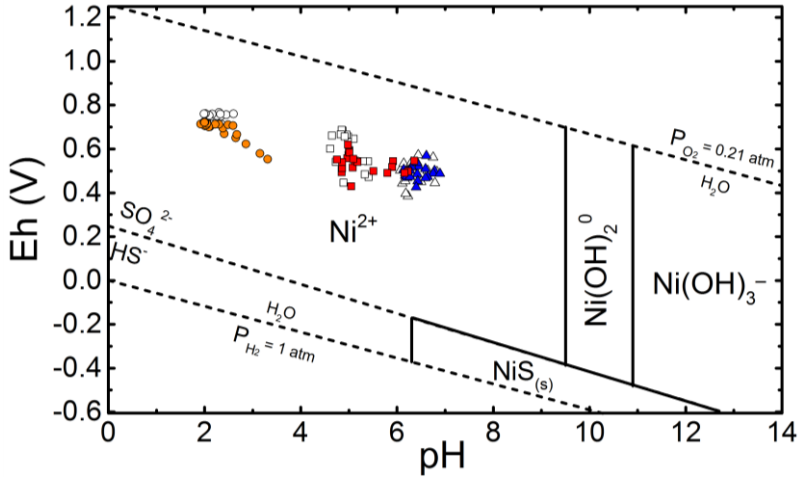

Figure 4.9. Pourbaix (Eh–pH) diagram for Ni. Squares, triangles, and circles represent data points for deionized (DI), oil sand process-affected water (OSPW), and acid rock drainage (ARD), respectively. Filled symbols represent data points for slurry coke and blank symbols represent dry coke.

A significant negative correlation between pH values and dissolved Ni concentrations ($r = -0.25$) and alkalinity values ($r = -0.19$) was observed, suggesting that pH-dependent precipitation–dissolution and sorption reactions are the principal factors controlling Ni mobility and aqueous concentrations within coke. A similar negative correlation value between pH values and Ni concentrations was reported by Puttaswamy & Liber (2011) and Nesbitt et al. (2018). Coke showed a positive net surface charge when porewater pH was less than pH_{PZC} (6.7–7.2), therefore, observing higher Ni concentrations in the column effluent during DI and ARD input compared with OSPW could be explained by a net positive surface charge along with the presence of cationic or non-ionic Ni species such as Ni^{2+}, $NiHCO_3^+$, and $NiSO_4^0$. Therefore, Ni had higher mobility

with DI and ARD, while Ni mobility was limited during OSPW because of adsorption of cationic Ni species, including Ni^{2+} and $NiHCO_3^+$, on the coke surface.

Cumulative mass release calculations indicated that Ni had a higher leaching potential from slurry than from dry coke with DI input (1330 µg kg^{-1} for slurry coke; 1170 µg kg^{-1} for dry coke), OSPW input (650 µg kg^{-1} for slurry coke; 760 µg kg^{-1} for dry coke), and for ARD input (3550 µg $kg^{-}1$ for slurry coke; 2110 µg kg^{-1} for dry coke; Table 4.3). Although Ni leaching occurred during all water input compositions, leaching efficiency was relatively low (<1%) to a maximum of 0.65% (3550 µg) of total Ni observed for slurry coke during the ARD input (Table 4.3, Appendix H). This result is attributed to large portion of Ni associated with porphyrin complexes (Nesbitt et al., 2017, 2018), which are stable and resistant to weathering (Lewan & Maynard, 1982; Zuliani et al., 2016). During DI and ARD inputs, approximately 60% of Ni leaching occurred during the first five pore volumes for both dry and slurry coke as a rapid initial release of Ni phases. Under OSPW input, around 90% of the Ni leaching from dry coke occurred during the first five pore volumes, whereas only 33.6% of Ni was leached from slurry coke. Nickel leaching from slurry coke was more gradual during OSPW input and required more volume (19 pore volumes) to reach 90% of total Ni cumulative mass (Figure 4.8, Appendix H).

4.3.1.3. Molybdenum

Effluent Mo concentrations were 0–5.84 µg L^{-1} for dry coke and 0.58–500 µg L^{-1} for slurry coke during DI input, 3.45–22.1 µg L^{-1} for dry coke and 4.55–147 µg L^{-1} for slurry coke during OSPW input, and 21.3–408 µg L^{-1} for dry coke and 3.41 to 102 µg L^{-1} for slurry coke during ARD input (Figure 4.6, Appendix G). Aqueous Mo concentrations decreased over time after the rapid initial release of Mo from the coke surface was followed by slower leaching of less mobile forms of Mo. Dissolved Mo concentrations within the column effluent followed a general order of ARD > OSPW > DI.

Geochemical modeling indicated that MoO_4^{2-} was the dominant aqueous Mo species during DI and OSPW input for both dry and slurry coke. In contrast, $H_2MoO_4^0$ was the dominant aqueous Mo species under ARD input for both dry and slurry coke (Figure 4.10). Thermodynamic modeling showed a general undersaturated state with respect to metal molybdates such as $NiMoO_4$ and $CaMoO_4$, which are likely to dissolve if present. Consequently, the precipitation of Mo phases does not control Mo mobility in this system. Because of the low concentration of aqueous Mo observed within the system, poly-nuclear species are not expected to form (Figure 4.10).

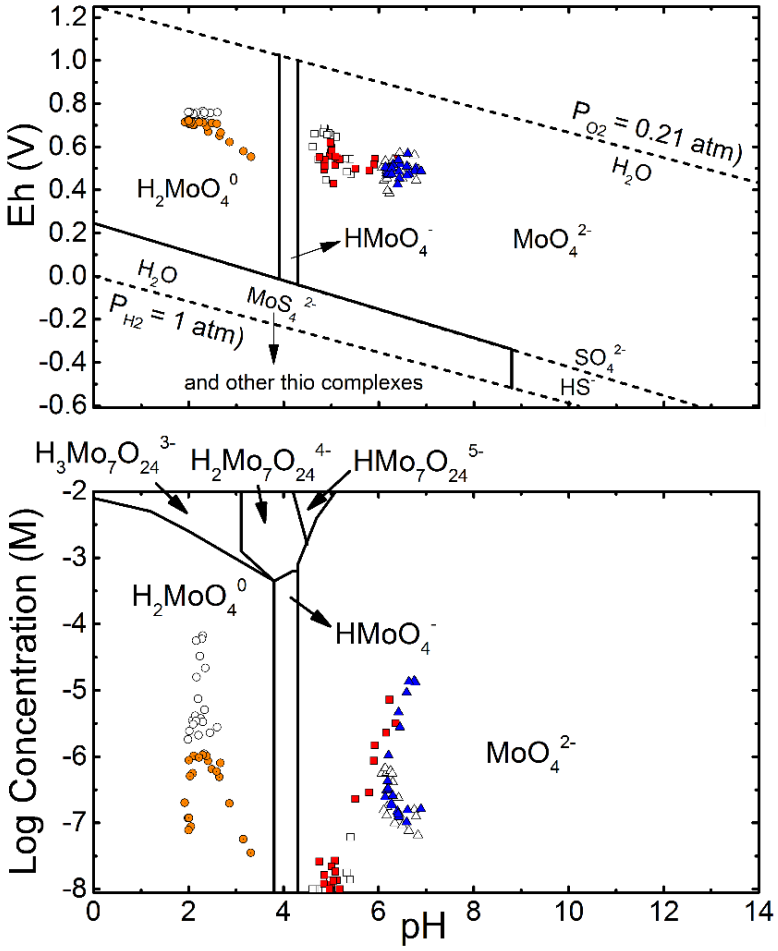

Figure 4.10. Pourbaix (Eh–pH) diagram (top) and Log concentration vs. pH for Mo(VI) (bottom). Squares, triangles, and circles represent data points for deionized (DI), oil sand process-affected water (OSPW), and acid rock drainage (ARD), respectively. Filled symbols represent data points for slurry coke; blank symbols represent data points for dry coke.

Robertson et al. (2019) reported that dissolved Mo concentrations and mobility is controlled by outer-sphere MoO_4^{2-} complexation. Surface complexation of MoO_4^{2-} is greatest when porewater pH is less than the pH_{PZC} (6.7 to 7.2, Appendix E) and the net surface charge is positive. Despite these conditions existing during DI and ARD input, complexation was limited during ARD input when $H_2MoO_4^0$ was predicted to be the dominant aqueous Mo species. An increase in effluent Mo concentrations for the slurry coke during ARD input within the first pore volume was observed (Figure 4.6). This increase could be explained by the initial presence of $HMoO_4^-$ species (up to 30% of aqueous Mo species based on thermodynamic modeling), and net positive surface ($pH < pH_{PZC}$) of coke. Thus, possible attenuation by surface complexation could limit Mo mobility

in the beginning, while the proportion of $HMoO_4^-$ species dropped rapidly to less than 5% after the first pore volume; therefore, Mo mobility was increased over the first pore volume resulting in higher Mo concentrations in the column effluent.

Iron-(hydr)oxides, pyrite, clays, and organic matter are phases within coke that could potentially adsorb MoO_4^{2-} (Goldberg et al., 1996; Bostick et al., 2003; Gustafsson & Tiberg, 2015). Their presence in coke was observed with EMPA and bulk geochemistry analyses (Figure 4.3) and also reported previously by Kessler & Hendry (2006) and Nesbitt et al. (2017). During DI input, these phases could adsorb MoO_4^{2-}, while under increased pH and ionic strength the potential to adsorb MoO_4^{2-} decreases (Goldberg & Forster, 1998; Gustafsson & Tiberg, 2015). Therefore, unfavorable attenuation of aqueous Mo species, the high ionic strength of ARD (I ~ 0.2) and OSPW (I ~ 0.05), and the presence of some anions such as Cl^- and HCO_3^- in OSPW that compete with MoO_4^{2-} for complexation on the coke surface resulted in higher leaching and mobility of Mo during OSPW and ARD input. Meanwhile, the low ionic strength of DI (I < 0.01) and attenuation of MoO_4^{2-} led to low Mo concentrations and leaching (Figure 4.6, Table 4.3). This result is consistent with the significant positive correlation between dissolved Mo concentration and alkalinity (r = 0.61) and EC (r = 0.22) under OSPW and ARD inputs. Also, Puttaswamy & Liber (2012) reported an increase in Mo mobility in the presence of Cl^- and HCO_3^-.

Molybdenum leaching occurred under all water input compositions; however, leaching efficiency was relatively low for all geochemical conditions (Appendix H). Slurry coke had a higher leaching potential compared with dry coke (3.82 vs. 514 µg kg^{-1} during DI, 276 vs. 780 µg kg^{-1} under OSPW, and 758 vs. 610 µg kg^{-1} during ARD inputs; Table 4.3). During DI and OSPW input, over 50% of Mo leaching occurred during the first five pore volumes for both dry and slurry coke as a rapid initial release of Mo phases occurred (Figure 4.8). Under ARD input, leaching was more gradual, and after five pore volumes only 40.4% and 33.5% of leaching occurred for dry and slurry coke, respectively. Molybdenum leaching during ARD input required more time to reach 90% of Mo cumulative mass release, requiring 19.8 pore volumes and 13.8 pore volumes for dry and slurry coke, respectively (Figure 4.8, Appendix H).

4.3.2. Transport Parameters

According to tracer test results and obtained breakthrough curves for the dry coke during DI input (Figure 4.11), the average linear pore water velocity and the dispersivity coefficient were 3.88×10^{-7} m s^{-1} and 0.166 cm, respectively (Table 4.4). However, for columns under ARD input,

no Br^- was detected within the effluent because of the net positive surface and adsorption of Br^-. Also, because of the similarity in flow rates, packed mass in the columns, and the PSD of dry coke and slurry coke for the small columns, the porewater velocity and dispersivity coefficient were similar among the columns. Therefore, the average linear pore water velocity and the dispersivity coefficient were calculated and applied to the small columns (Table 4.4). The residence time of the column was 6.64 d (Table 4.4); this is a particularly important parameter in hydrogeochemical systems because it affects kinetically controlled reactions and is directly linked to cumulative mass discharge.

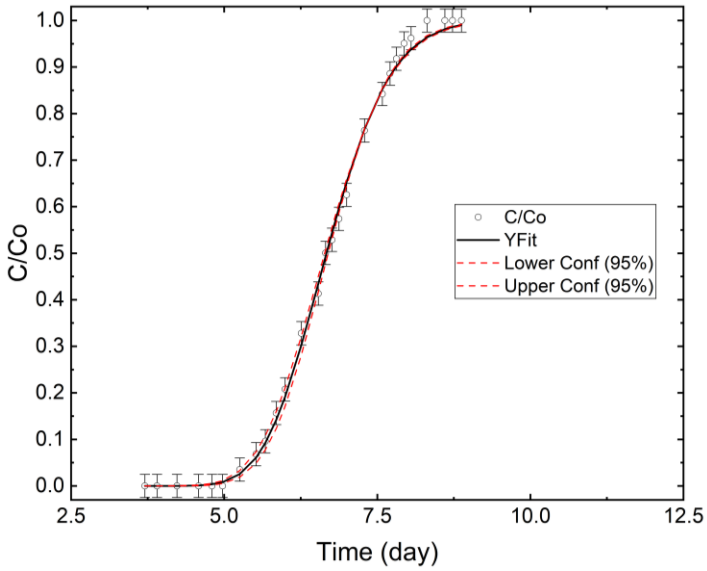

Figure 4.11. Breakthrough curve for dry coke during DI input (black line). Error bars represent the electrode ±2.5% electrode sensitivity. Red dashed lines indicate the lower and higher 95% confidence.

Table 4.4. Calculated hydraulic parameters for dry coke during DI input.

Parameter	Units	Value
Average linear velocity	m s^{-1}	3.88×10^{-7}
Dispersivity	cm	0.166
PV[a]	L	0.33

[a]PV: pore volume

4.4. Large Column

4.4.1. Aqueous Geochemistry

The pH of influent solutions remained relatively constant throughout the experiment with the median value 7.40 for DI, 8.70 for synthetic OSPW, 8.90 for field OSPW, and 2.10 for ARD. The effluent pH ranged from 4.62–5.53 during DI input, 5.88–6.80 for synthetic OSPW input, and 6.6–7.10 for field OSPW input, which was a decrease compared to the influent pH (Figure 4.12). The pH reduction under DI and OSPW influent (both synthetic and field), along with the presence of Fe and S in the column effluent (Figure 4.13), is indicative of acid generation via Fe-S–bearing phase oxidation (i.e., pyrite). Oxidation of Fe-S phases generates protons and releases S, and the presence of Fe-S phases was observed within the coke matrix in the EMPA-EDX spectra (Figure 4.3) and reported previously by Kessler & Hendry (2006). Also, elevated concentrations of Ca, Mg, Sr, and Ba in the column effluent (Appendix G) in addition to the significant positive correlation of Sr with Ca ($r = 0.98$), Mg ($r = 0.84$), and Ba ($r = 0.47$) indicate carbonate dissolution. The pH decrease within the system could lead to carbonate dissolution and mobilize these elements. Although pH differences between the influent and effluent under ARD input were not significant and generally were similar, a slightly higher pH (2.40–2.70) was observed in the effluent during the first pore volume (Figure 4.12).

The influent EC and alkalinity of all solutions was relatively consistent during the experiment. The median EC for the influent was 15.30 µS cm^{-1} for DI, 4.82 mS cm^{-1} for synthetic OSPW, and 4.97 mS cm^{-1} for OSPW. The median EC for the ARD solution used throughout the experiment was 8.94 mS cm^{-1} (Figure 4.12). The median value for influent alkalinity was 9.96 mg L^{-1} (as $CaCO_3$) for DI, 714 mg L^{-1} for synthetic OSPW, and 920 mg L^{-1} for field OSPW. Alkalinity could not be measured for the ARD solution because the influent and porewater pH are less than the pH of the bromocresol green methyl indicator (Figure 4.12).

The EC and alkalinity of the effluent from DI input decreased rapidly from 1350 to 97.0 µS cm^{-1} and from 84.0 to 38.0 mg L^{-1} (as $CaCO_3$) after three pore volumes (Figure 4.12). The EC decreased from 1350 to 53.0 µS cm^{-1} under DI input, whereas it ranged from 4 to 5.10 mS cm^{-1} under OSPW input and 6.40 to 9.60 mS cm^{-1} under ARD input (Figure 4.12). In addition, the alkalinity ranged from 21.8 to 91 mg L^{-1} (as $CaCO_3$) under DI input, while it ranged from 485 to 934 mg L^{-1} (as $CaCO_3$) under OSPW input. During OSPW (both synthetic and field) and ARD input, the differences between column influent and effluent EC values were not measurable (Figure

4.12). Also, a significant positive correlation between pH and EC (r = 0.83) and alkalinity (r = 0.87) was observed during DI and OSPW input, which likely corresponded to carbonate dissolution and acid-generating products such as Fe and S.

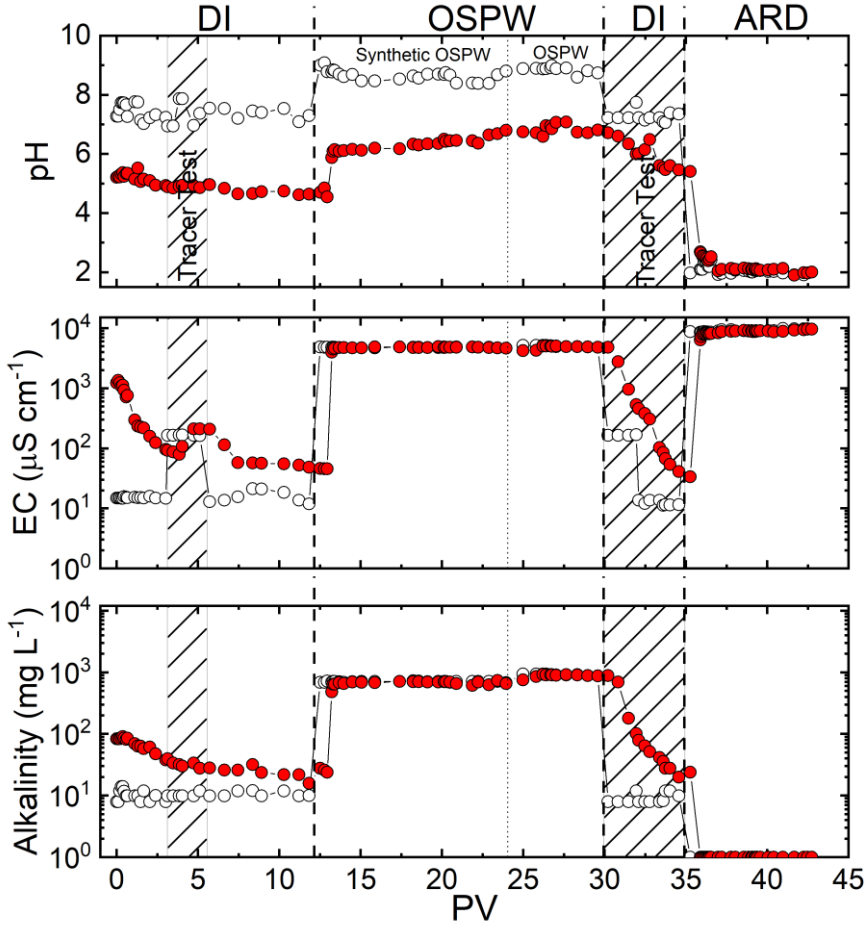

Figure 4.12. Influent (open symbols) and effluent (filled symbols) pH, EC, and alkalinity as a function of pore volume (PV) for the large column experiment during deionized (DI), oil sand process-affected water (OSPW), and acid rock drainage (ARD). The units for alkalinity are mg L^{-1} as $CaCO_3$ and values plotted on the x-axis are equal to zero. Vertical dashed lines indicate transitions between input solution compositions. The vertical black dotted line during OSPW input indicates the transition from synthetic to field OSPW. Hatched areas represent times during which tracer tests were conducted.

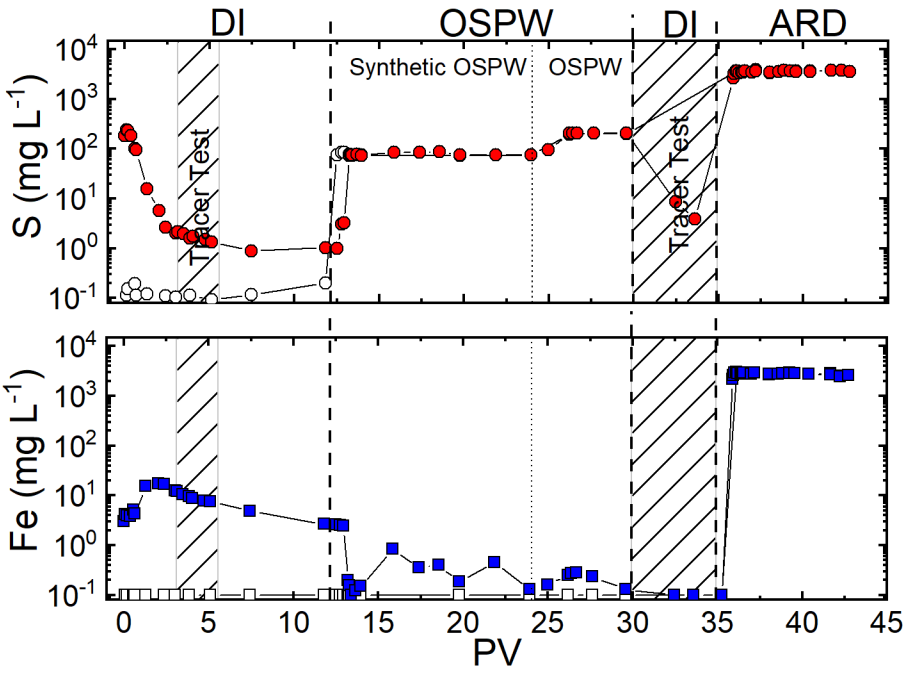

Figure 4.13. Influent (open symbols) and effluent (filled symbols) S and Fe concentrations as a function of pore volume (PV) for the large column experiment during deionized (DI), oil sand process-affected water (OSPW), and acid rock drainage (ARD). Vertical dashed lines indicate transitions between input solution compositions. Vertical black dotted line during OSPW input indicates the transition from synthetic to field OSPW. Hatched areas represent times during which tracer tests were conducted.

4.4.1.1. Vanadium

Influent solutions, including DI, synthetic OSPW, and ARD, did not contain V, while field OSPW contained V at a median concentration of 3 µg L^{-1}. Dissolved V concentrations within column effluent were varied under different water input compositions and followed a general order ARD > OSPW > DI (Figure 4.14). With DI input, V in the effluent generally approached the method detection limit with a maximum concentration of 7.60 µg L^{-1}. Effluent V concentrations were 5.40–97.8 µg L^{-1} for synthetic OSPW and 19.3–31.8 µg L^{-1} for field OSPW. Also, the highest effluent V concentrations were observed with ARD input water (368–6900 µg L^{-1}; Figure 4.14, Appendix G). Extensive V release in the presence of ARD compared with DI and OSPW input water may be due to oxidation of V(III) by Fe(III), as well as from the release of the initial pool of V(V) from the coke particle surfaces, which produced a pool of soluble V(V). Therefore, V(III) and V(V) contribute to dissolved V in fluid petroleum coke leachates. However, octahedral coordinated V(III) and V(V) components comprised a small portion of bulk V speciation (Nesbitt

& Lindsay, 2017). These findings suggest that even if V leaching by DI and OSPW becomes limited, a switch to acidic conditions could promote additional leaching. Aqueous V concentrations decreased over time during input of synthetic OSPW and ARD as the rapid initial release of adsorbed V(V) from the coke particle surfaces was followed by slower leaching of less mobile and available V forms. Vanadium concentrations were significantly correlated with pH values ($r = -0.61$) and EC values ($r = 0.51$), suggesting that the high ionic strength of OSPW ($I \sim 0.05$) and ARD ($I \sim 0.2$) and the low pH of ARD ($pH \sim 2$) resulted in higher V release.

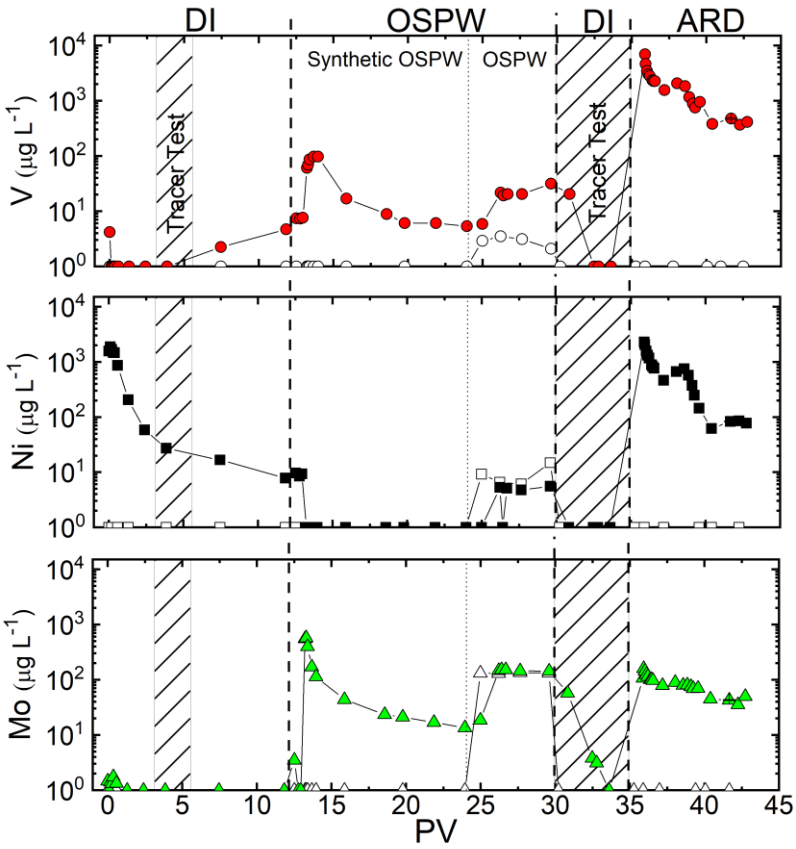

Figure 4.14. Influent (open symbols) and effluent (filled symbols) V, Mo, and Ni aqueous concentrations as a function of pore volume for the large column experiment during deionized (DI), oil sand process-affected water (OSPW), and acid rock drainage (ARD). All concentrations are in µg L^{-1} and values plotted on x-axis are below the method detection limit. Vertical dashed lines indicate a transition between input solution compositions. Vertical black dotted line in the OSPW phase indicates the transition from synthetic to field OSPW. Hatched areas represent times during which tracer tests were conducted.

Based on thermodynamic modeling, $H_2VO_4^-$ was the dominant aqueous V species in the column effluent during DI and OSPW input, whereas VO^{+2} and VO_2^+ were the dominant species during ARD input (Figure 4.15). However, oxidation of aqueous V(IV) to V(V) occurs rapidly under oxic conditions (Jensen-Fontaine, 2012). Therefore, aqueous VO^{+2} present during ARD input could be oxidized further to VO_2^+. Dissolved V(IV) and V(V) within the coke leachate have been reported previously by Li et al. (2007). Also, thermodynamic modeling showed that porewater was consistently undersaturated with respect to calcium vanadate and other V(V) phases. Due to the low concentration of V ($V < 10^{-3.87}$ M), poly-nuclear species are not expected to form (Figure 4.15). Also, poor agreement between the measured and theoretical Eh values is well established (Lindberg & Runnells, 1984) and a slight decrease in the input Eh values (±50 mV) shifted the model prediction to Fe(III)/Fe(II) as the dominant Fe oxidation state.

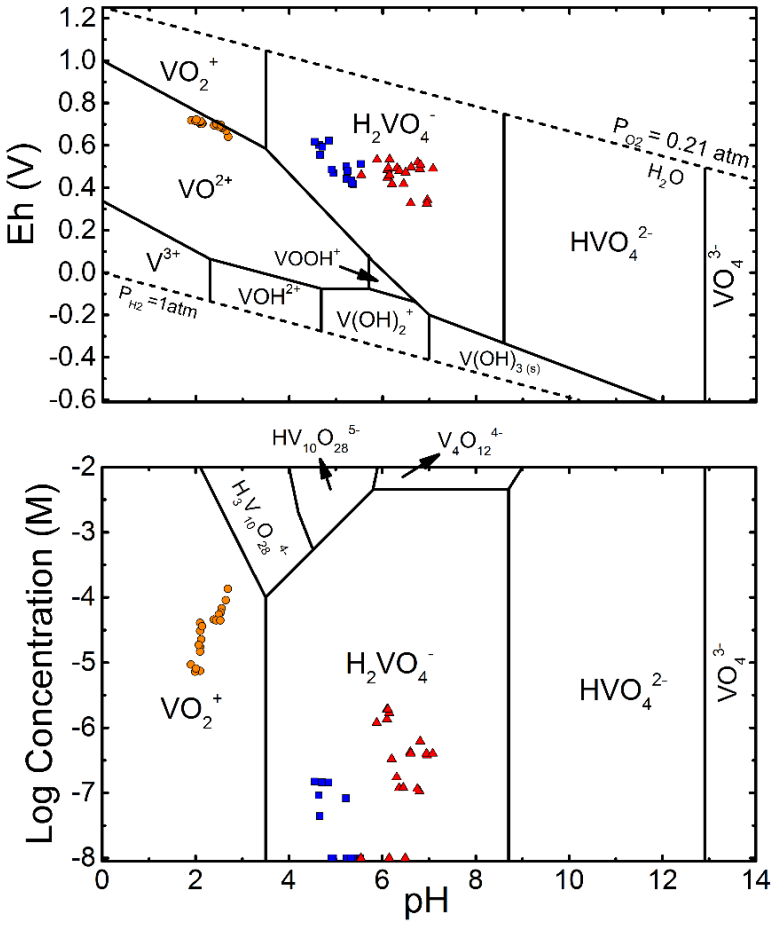

Figure 4.15. Pourbaix (Eh–pH) diagram for vanadium (top) and predominance diagram showing aqueous V(V) speciation as a function of pH and total V concentration (bottom). Blue squares, red triangles, and orange circles represent data points for during deionized (DI), oil sand process-affected water (OSPW), and acid rock drainage (ARD), respectively.

According to porewater pH and coke pH_{PZC}, the net surface charge for coke is positive during DI and ARD input ($pH < pH_{PZC}$), while it is negative during OSPW input ($pH > pH_{PZC}$). Therefore, the adsorption of aqueous $H_2VO_4^-$ likely controlled V mobility and concentrations during DI input. In contrast, adsorption of aqueous $H_2VO_4^-$ and VO_2^+ (or VO^{2+}) species was likely limited during OSPW and ARD input.

Cumulative V release during DI input is the lowest (13 µg kg^{-1}) compared to OSPW input (49 µg kg^{-1} for field OSPW and 123 µg kg^{-1} for synthetic OSPW) and ARD input (4610 µg kg^{-1}; Figure 4.16, Appendix H). Despite high V concentrations, only 0.31% (4350 µg kg^{-1}) of the total V was leached during the experiment and 96% (4160 mg) of leaching occurred during the ARD input. This result is attributed to the large proportion of V associated with porphyrin complexes, which are both stable and resistant to weathering (Lewan & Maynard, 1982; Zuliani et al., 2016).

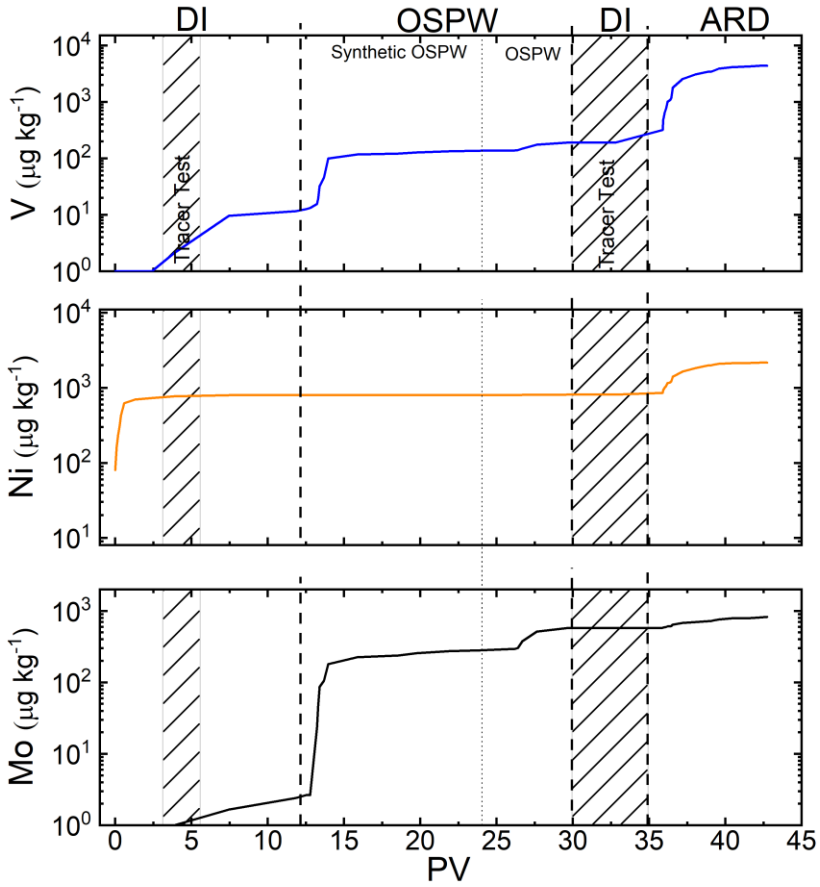

Figure 4.16. Cumulative V, Ni, and Mo release from fluid petroleum coke under sequential input of different water compositions including deionized (DI), oil sand process-affected water (OSPW), and acid rock drainage (ARD) for the large column. All units are in µg L^{-1}.

4.4.1.2. Nickel

Column influent solutions, including DI, synthetic OSPW, and ARD did not contain Ni, while field OSPW contained Ni at a median concentration of 7.86 µg L^{-1}. Dissolved Ni concentrations within the column effluent were varied for different water compositions and followed a general order ARD > DI > OSPW (Figure 4.14). Effluent Ni concentrations during DI input were 7.80–1880 µg L^{-1} compared with 62.4–2300 µg L^{-1} during ARD input. Porewater Ni concentrations were close to the method detection limit under OSPW input, with a maximum concentration of 5.58 µg L^{-1} during field OSPW input (Figure 4.14, Appendix G). Aqueous Ni concentrations decreased over time during ARD and DI input as the rapid initial release of Ni phases from the coke particle surface was followed by slower leaching of less mobile and available inorganic Ni forms including Ni(II)-sulfide and Ni(II)-oxide.

Geochemical modeling indicated that Ni^{2+} accounted for 50 to 90% of dissolved Ni within column effluent under ARD and DI input, while $NiSO_4^0$ comprised the remainder (Figure 4.17). Thermodynamic modeling also showed that Ni^{2+} accounted for ~50% of dissolved Ni in the column effluent under field OSPW input, whereas $NiSO_4^0$ and $NiHCO_3^+$ comprised ~10% and ~30%, respectively. Complexation of Ni with carbonate and sulfate forms non-ionic species ($NiCO_3^0$, $NiSO_4^0$) which may increase Ni mobility and limit Ni sorption. Thermodynamic modeling suggested a general undersaturated state with respect to $NiO_{(s)}$, $NiCO_{3(s)}$, and $Ni(OH)_{2(s)}$ which means these phases were not principal controls on dissolved Ni concentrations.

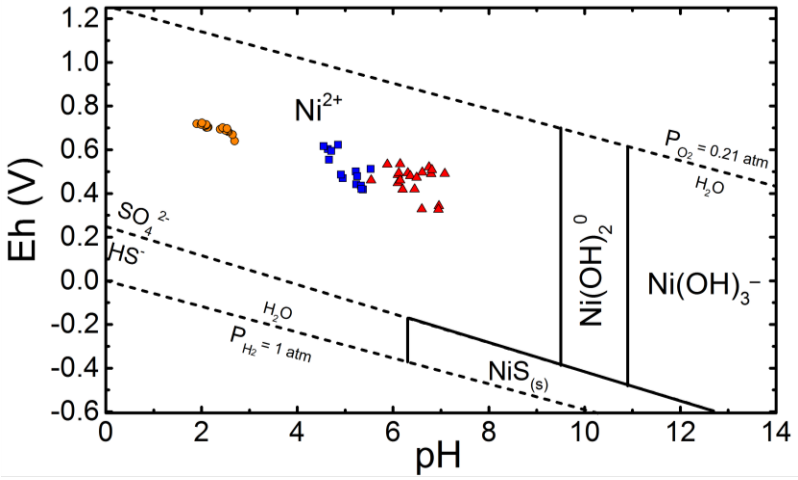

Figure 4.17. Pourbaix (Eh–pH) diagram for Ni. Blue squares, red triangles, and orange circles represent data points for deionized (DI), oil sand process-affected water (OSPW), and acid rock drainage (ARD), respectively.

A significant negative correlation between Ni concentrations and pH values ($r = -0.38$) and alkalinity values ($r = -0.44$) was observed, which suggests that pH-dependent precipitation–dissolution and sorption reactions are principal controls on Ni mobility during the experiment. A similar negative correlation between aqueous Ni concentrations and pH has been reported previously by Puttaswamy & Liber (2011) and Nesbitt et al. (2018). Considering the porewater pH and pH_{PZC} for coke, the net surface charge of coke is negative during OSPW input, while it is positive under DI and ARD input. The net positive surface charge and dominance of cationic or non-ionic species (Ni^{2+} and $NiSO_4^0$) during DI and ARD input enhanced Ni mobility. Ni mobility was limited during OSPW input due to the net negative surface charge and dominance of Ni^{2+} and $NiHCO_3^+$ species. Adsorption of these Ni species onto the coke surface could explain why a lower Ni concentration was observed in the effluent compared with influent during field OSPW input (Figure 4.14).

Nickel mobility under synthetic OSPW input was limited, with a concentration equal to zero in the effluent, while Ni was attenuated within the system during field OSPW input, resulting in a negative cumulative release. Although Ni leaching occurred during DI and ARD input, only 0.40% (2160 μg kg^{-1}) of total Ni was leached during the experiment, with ~37% (800 μg kg^{-1}) and ~ 63% (1360 μg kg^{-1}) leached during DI and ARD input, respectively (Appendix H). This result is attributed to the large proportion of Ni associated with porphyrin complexes, which are both stable and resistant to weathering (Lewan & Maynard, 1982; Zuliani et al., 2016).

4.4.1.3. Molybdenum

Column influent solutions, including DI, synthetic OSPW, and ARD, did not contain Mo, while field OSPW contained Mo at a median concentration of 133 μg L^{-1}. Dissolved Mo concentrations within the column effluent were varied for different water compositions and followed a general order OSPW > ARD > DI (Figure 4.14). Effluent Mo concentrations were 13–574 μg L^{-1} for synthetic OSPW input compared with 57.5–153 μg L^{-1} for field OSPW input. Also, Mo concentrations in the effluent were 35.5–160 μg L^{-1} during ARD input. Porewater Mo concentrations approached the method detection limit during DI input to a maximum concentration of 3.80 μg L^{-1} (Figure 4.14, Appendix G). Aqueous Mo concentrations decreased over time during OSPW and ARD input, as the rapid initial release of Mo phases at the coke particle surfaces was followed by slower leaching of less mobile and available outer-sphere Mo forms.

Thermodynamic modeling suggested that MoO_4^{2-} was the dominant aqueous Mo species under DI and OSPW input, while $H_2MoO_4^0$ was the dominant species in the effluent during ARD input (Figure 4.18). Geochemical modeling indicated a general undersaturated state with respect to metal molybdates, which are likely to dissolve if they are present. In addition, due to the low dissolved Mo concentrations, poly-nuclear species were not expected to form (Figure 4.18).

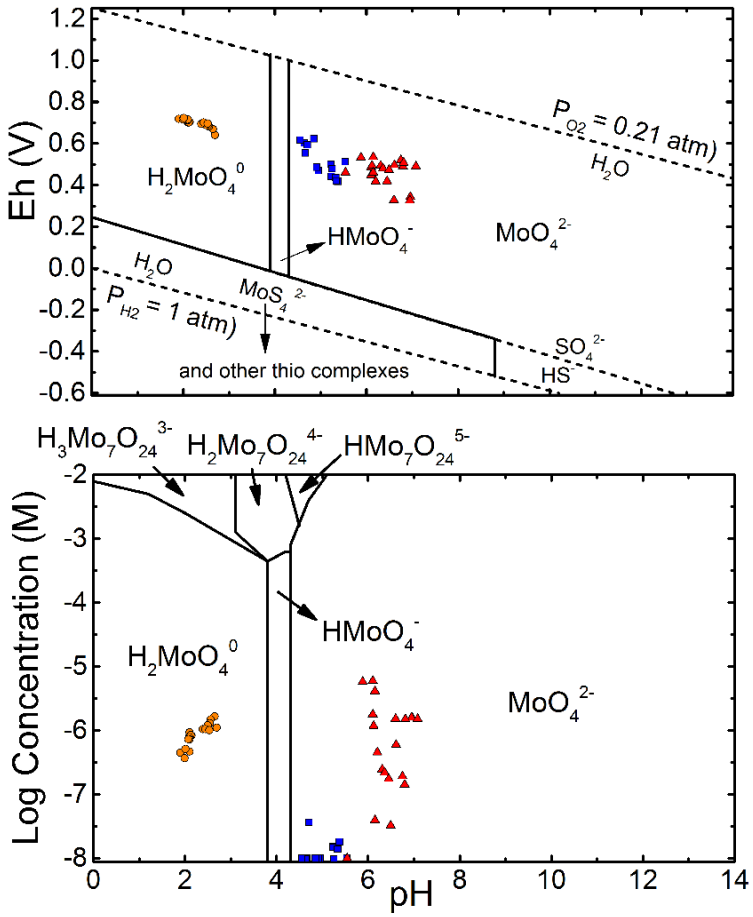

Figure 4.18. Pourbaix (Eh–pH) diagram for vanadium (top) and predominance diagram showing Mo(VI) aqueous speciation as function of pH and concentration (bottom). Blue squares, red triangles, and orange circles represent data points for deionized (DI), oil sand process-affected water (OSPW), and acid rock drainage (ARD), respectively.

Robertson et al. (2019) reported that outer-sphere complexation of MoO_4^{2-} influences dissolved Mo concentrations and mobility in coke deposits. Surface complexation of MoO_4^{2-} is greatest when pore water pH is less than pH_{PZC} (6.7 to 7.2, Appendix E) and the net surface charge is positive. Although these conditions existed during DI and ARD input, complexation was likely limited during ARD input when $H_2MoO_4^0$ was predicted to be the dominant aqueous Mo species.

Therefore, it is unfavorable for $H_2MoO_4^0$ and MoO_4^{2-} to be attenuated under OSPW and ARD input, while MoO_4^{2-} was attenuated during DI input via outer-sphere complexes.

The presence of Fe-(hydr)oxides, pyrite, clays, and organic matter within coke particles was observed by EMPA and bulk geochemistry analyses, and their presence was also previously reported by Kessler & Hendry (2006) and Nesbitt et al. (2017). These phases can potentially adsorb MoO_4^{2-} under mildly acidic conditions (~pH 3–6; Goldberg et al., 1996; Bostick et al., 2003; Gustafsson & Tiberg, 2015). During DI input, these phases could adsorb MoO_4^{2-}, while the increased pH and ionic strength decreased their adsorption capacity (Goldberg & Forster, 1998; Gustafsson & Tiberg, 2015); therefore, MoO_4^{2-} attenuation was unlikely to occur under OSPW and ARD input. A significant positive correlation between dissolved Mo concentrations and EC ($r = 0.26$) and alkalinity ($r = 0.36$) was observed, suggested that the leachable portion of Mo is in outer-sphere MoO_4^{2-} complexes. Additionally, Cl^- and HCO_3^- would compete with MoO_4^{2-} for sorption on the coke surface, therefore their presence within solution would increase Mo mobility (Puttaswamy & Liber, 2012), which is consistent with the higher mobility of Mo observed during OSPW input compared to DI input (Figure 4.14). The high ionic strength of ARD ($I \sim 0.2$) and OSPW ($I \sim 0.05$) and the presence of some anions such as Cl^- and HCO_3^- within the OSPW phases stimulates desorption of MoO_4^{2-} outer-sphere complexes at the coke surface.

Cumulative Mo release during DI and field OSPW inputs were the lowest, at 4 and 2 µg kg^{-1}, respectively. Most Mo leaching occurred under synthetic OSPW and ARD input, at 280 and 235 µg kg^{-1}, respectively (Figure 4.16, Appendix H). However, only 0.69% (520 µg kg^{-1}) of the total Mo within the bulk coke was leached during the experiment. This result is attributed to the large portion of Mo associated with Mo(IV) disulfide, which is strongly resistant to oxidation (Lindsay et al., 2015; Plumlee, 1999).

4.4.2. Geophysical inversion and forward modeling results

4.4.2.1. Inversion modeling of resistivity

The apparent resistivity declined as a solution containing Br^-, with a higher EC (165.5 µS cm^{-1}), was passed through the column, while the decay part exhibited an increase in apparent resistivity as the saturated column was flushed with DI having lower EC (15.5 µS cm^{-1}) (Figure 4.19). The average linear pore water velocities for the injection and decay portions of the first tracer test were $6.98 \pm 0.15 \times 10^{-7}$ and $8.33 \pm 0.27 \times 10^{-7}$ m s^{-1}, and were generally consistent (Table 4.5).

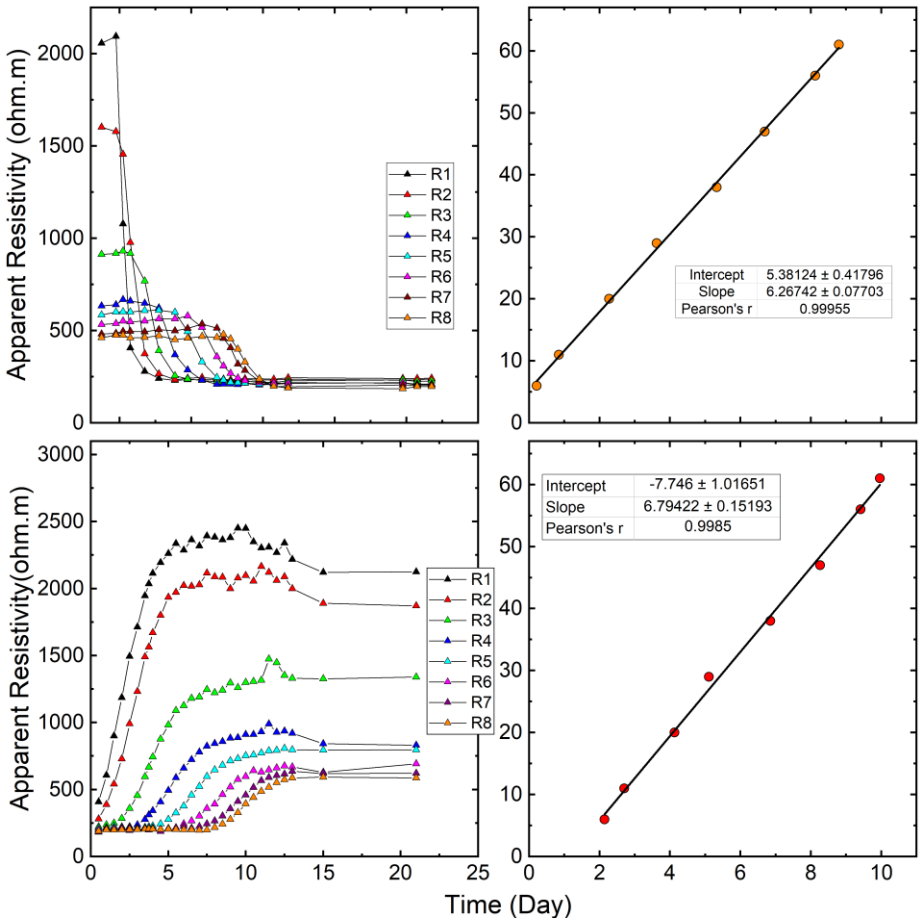

Figure 4.19. Apparent resistivity as function of time (left) and linear regression of mid-point (right) which define the average linear velocity for the first tracer. This includes the injection of the tracer (top) and decay of the first tracer (bottom). Electrodes were configured in a ring position, with R1 to R8 placed from the bottom to top of the column.

Table 4.5. Average linear velocities for the large column, measured based on mid-point theory for the first tracer test including injection and decay.

Array configuration	Units	Injection	Decay
Ring	m s^{-1}	7.26× 10^{-7}	7.87× 10^{-7}
Lateral A-Wenner	m s^{-1}	6.92× 10^{-7}	8.43× 10^{-7}
Lateral B-Wenner	m s^{-1}	6.99× 10^{-7}	8.44× 10^{-7}
Lateral C-Wenner	m s^{-1}	6.83× 10^{-7}	8.22× 10^{-7}
Lateral D-Wenner	m s^{-1}	6.90× 10^{-7}	8.68× 10^{-7}

The line intercept for linear regression in figure 4.19 shows the point of injection (column inlet port) in decay part of tracer; first electrode is located at 6 cm from the bottom of the column.

However since salt is released during the injection part of tracer test, the line intercept for the injection part became irrelevant.

4.4.2.2. Forward modeling of resistivity

The forward modeling using measured hydrodynamic parameters from the tracer test, and reaction rates for individual species (fitting the output concentration from the model with measured aqueous concentration, Appendix A) inside COMSOL Multiphysics was calculated for all rings (1-D). Since the measured apparent resistivity is not associated with a point, rather an average of adjacent region to electrodes, the calculated apparent resistivity ±2.5 cm from the ring is also considered. Results were in good agreement with measured values (Figures 4.13 and 4.14). Calculated apparent resistivity from forward modeling were in good agreement with measured apparent resistivity.

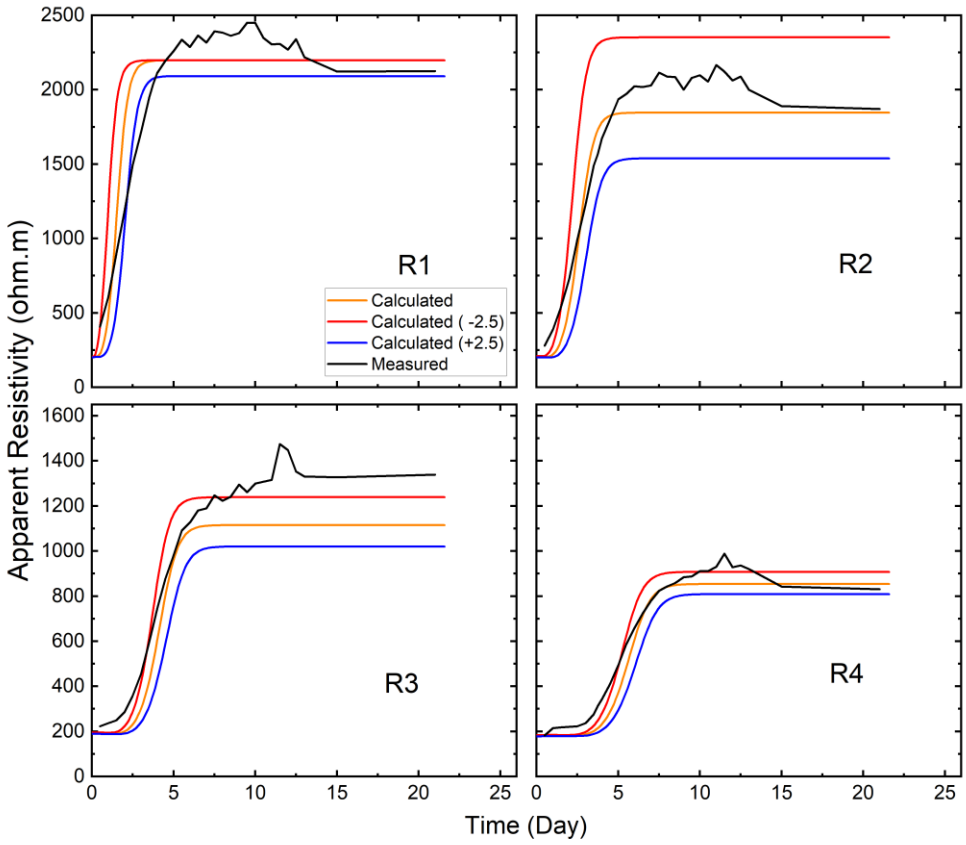

Figure 4.20. Forward modeling results for the first four rings (apparent resistivity vs. time) during the first tracer test. The black line is the measured apparent resistivity associated with the ring positions. Red, blue, and orange lines are the calculated apparent resistivity for that specific level ±2.5 cm.

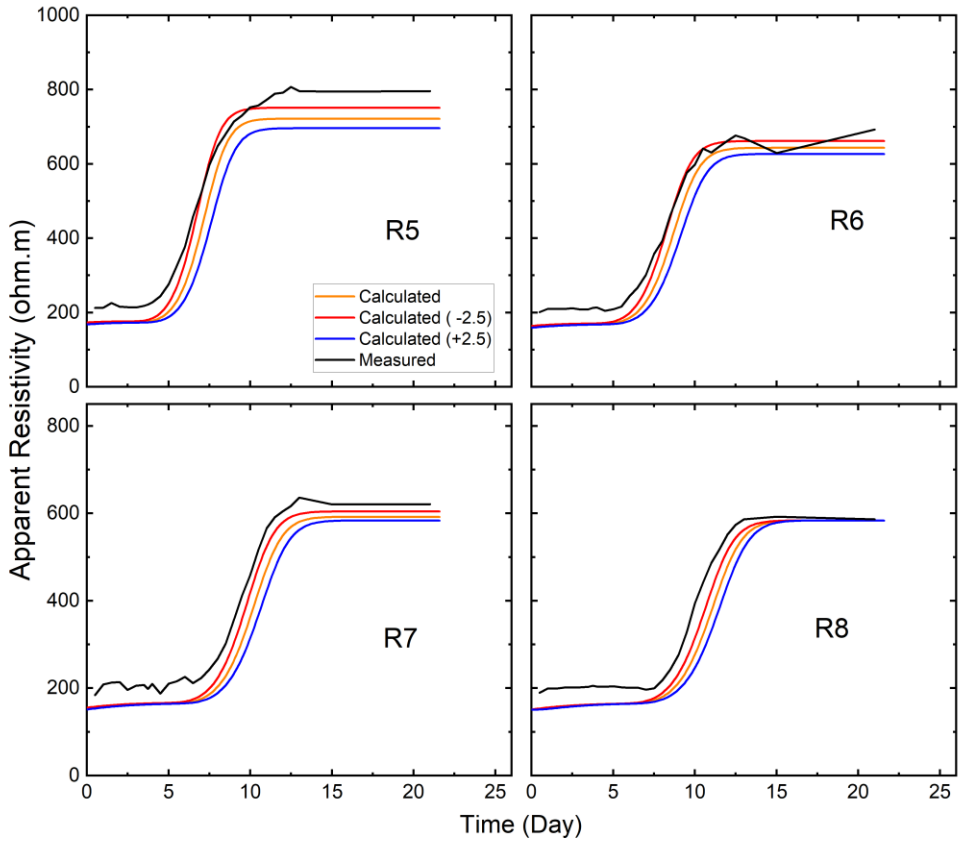

Figure 4.21. Forward modeling results for the first four rings (apparent resistivity vs. time) during the first tracer test (Decay). The black line is the measured apparent resistivity associated with the ring positions. Red, blue, and orange lines are the calculated apparent resistivity for that specific level ±2.5 cm.

4.4.3. Transport properties

According to tracer test results and obtained breakthrough curves for the large column (Figure 4.22), the average linear pore water velocity and the dispersivity coefficients were 6.96 ± 0.163 × 10^{-7} m s^{-1} and 0.5763 ± 0.1661 cm, respectively (Table 4.6, Appendix I). Due to Na^+ interference with the Br^- electrode during the injection part of the second tracer test, which flushed residual OSPW containing up to 1100 mg L^{-1} Na^+ (Appendix G), the associated breakthrough curve was noisy and was removed from our interpretation. In addition, the residence time of the column was 11.02 ± 0.20 d (Table 4.6), which is a particularly important parameter in hydrogeochemical systems because it affects kinetically controlled reactions and is directly linked to cumulative mass discharge.

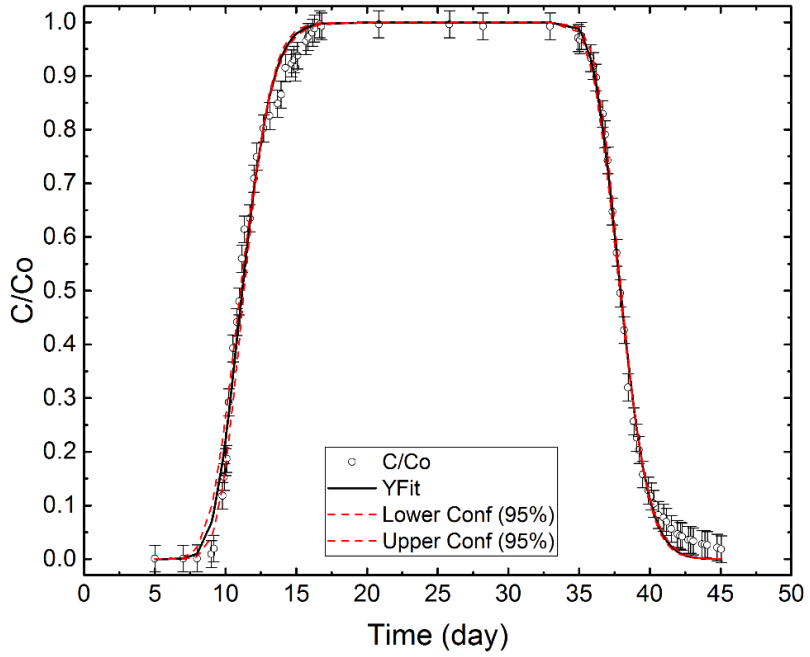

Figure 4.22. Breakthrough curve for the large column as a function of time (black line). Error bars represent the electrode ±2.5% electrode sensitivity. Red dashed lines indicate the lower and higher 95% confidence.

Table 4.6. Calculated hydraulic parameters for the large column including first tracer test injection part (A1), decay part (A2), and second tracer test-decay part (B2).

Parameter	**Units**	**A1**	**A2**	**B2**
Average linear velocity ($\times 10^{-7}$)	m s^{-1}	6.86	7.19	6.83
Dispersivity	cm	0.470	0.448	0.811
PV[a]	L	5.29	5.17	5.40

[a]PV: pore volume

CHAPTER 5: CONCLUSIONS

The objectives of this research were to (i) investigate metal leaching (V, Mo, and Ni) from fluid petroleum coke under the geochemical conditions existing in locations where coke might be stored or used in the mine closure landscape, (ii) examine leaching efficiency and leaching behavior over time, and (iii) establish forward and inverse geophysical modeling to evaluate column transport properties. These objectives were addressed by a series of leaching experiments under water compositions (meteoric water, OSPW, and ARD) that may interact with petroleum coke at mine closure, and by linking geochemical factors to metal (V, Mo, and Ni) mobility.

This study concluded that V, Mo, and Ni are contaminants of potential concern within these closure systems. Leaching of V and Mo during ARD and OSPW input was enhanced by oxic conditions and/or high ionic strength of the solutions along with limited sorption. In the presence of meteoric water, sorption attenuated V and Mo within the coke leachates. High net positive surface charge of coke particles during ARD input along with the presence of V and Mo in their cationic states (VO_2^+/VO^{2+} and $H_2MoO_4^0$) limited sorption, and therefore increased the mobility of these metals. The high ionic strength of OSPW promoted desorption of Mo(VI) from outer-sphere surface complexes. Finally, we attributed enhanced Ni leaching in the presence of meteoric water and ARD to the limited potential for sorption and to the enhanced solubility of the hydroxide or carbonate phases. The findings of this study complement those of earlier studies by Kessler and Hendry (2006), Nesbitt (2016), and Swerhone (2018), and suggest that even if leaching in the presence of meteoritic water is limited, switching to acidic conditions (by encountering ARD water) could result in abundant V, Ni, and Mo leaching. The results from this research study can be used to optimize mine closure design with respect to metal leaching and mobility.

Although metal leaching from fluid petroleum coke occurs through interactions with different water compositions, leaching efficiency was generally low with less than 1% of bulk V, Ni, and Mo concentrations leached. This is consistent with previous research by Kessler and Hendry (2006) and Nesbitt (2016) that show low metal leaching rates from fluid petroleum coke. The solid-phase fraction that hosts readily leachable metals is either volumetrically small, or the coke grains contain these metals in a way that is largely inaccessible to porewater. Also, more fractures, broken pieces, and particle attachment were observed in slurry coke compared with dry

coke, which could explain why slurry coke exhibited a higher leaching potential under all geochemical conditions. In addition, the residual OSPW in slurry coke, which contains a small amount of metals, could contribute to the apparent metal leaching and should be considered as another source of metal leaching. Metal leaching (i.e, V, Ni, and Mo) decreased during the experiment, which suggests that the leachable portion was limited.

Geophysical techniques (i.e., SP and RS) are helpful tools to study flow and transport phenomena and could be used to characterize transport mechanisms in subsurface such as flow pathways and velocity. These techniques provide necessary information to evaluate possible contamination within subsurface since they are sensitive to variation in electrical properties such as a possible leak from dam or tailings and will help manage, design, and optimize remediation strategies. Using non-invasive and indirect methods with high sampling density in addition to possible automated data acquisition makes geophysical methods important tools for subsurface monitoring. However, these techniques cannot be used alone and they must be accompanied by additional data from the other in situ tests (e.g., chemical analysis of pore water, pumping tests) to verify the geoelectrical results.

REFERENCES

Adamson, A. (1973). *Textbook of Physical Chemistry*. Academic Press inc.

AER. (2015). *Alberta's Energy Reserves 2014 and Supply/Demand Outlook 2015– 2024*. Alberta Energy Regulator.

AER. (2019). *ST: Alberta Mineable Oil Sands Plant Statistic (Calgary)*.

Ahmed, A. S., Jardani, A., Revil, A., & Dupont, J. P. (2016). Specific storage and hydraulic conductivity tomography through the joint inversion of hydraulic heads and self-potential data. *Advances in Water Resources*, *89*, 80–90. https://doi.org/10.1016/j.advwatres.2016.01.006

Alam, S., Cossio, M., Robinson, L., Wang, X., Kenney, J. P. L., Konhauser, K. O., MacKenzie, M. D., Ok, Y. S., & Alessi, D. S. (2016). Removal of organic acids from water using biochar and petroleum coke. *Environmental Technology & Innovation*, *6*, 141–151. https://doi.org/10.1016/j.eti.2016.08.005

Allison, J. D., Brown, D. S., & Novo-Gradac, K. J. (1991). *MINTEQA2/PRODEFA2. A geochemical assessment model for environmental systems U.S. EPA, Athens, GA 30613, USA*.

Archie, G. E. (1942). The Electrical Resistivity Log as an Aid in Determining Some Reservoir Characteristics. *Transactions of the AIME*, *146*(01), 54–62. https://doi.org/10.2118/942054-G

Aureli, F., Ciardullo, S., Pagano, M., Raggi, A., & Cubadda, F. (2008). Speciation of vanadium(IV) and (V) in mineral water by anion exchange liquid chromatography-inductively coupled plasma mass spectrometry after EDTA complexation. *Journal of Analytical Atomic Spectrometry*, *23*(7), 1009–1016. https://doi.org/10.1039/B805234B

Baken, S., Larsson, M. A., Gustafsson, J. P., Cubadda, F., & Smolders, E. (2012). Ageing of vanadium in soils and consequences for bioavailability. *European Journal of Soil Science*, *63*(6), 839–847. https://doi.org/10.1111/j.1365-2389.2012.01491.x

Baker, L. F., Ciborowski, J. J. H., & MacKinnon, M. D. (2012). Petroleum coke and soft tailings sediment in constructed wetlands may contribute to the uptake of trace metals by algae and aquatic invertebrates. *Science of The Total Environment*, *414*, 177–186. https://doi.org/10.1016/j.scitotenv.2011.10.011

Binley, A., Cassiani, G., Middleton, R., & Winship, P. (2002). Vadose zone flow model parameterisation using cross-borehole radar and resistivity imaging. *Journal of Hydrology*, *267*(3), 147–159. https://doi.org/10.1016/S0022-1694(02)00146-4

Binley, A., Hubbard, S. S., Huisman, J. A., Revil, A., Robinson, D. A., Singha, K., & Slater, L. D. (2015). The emergence of hydrogeophysics for improved understanding of subsurface processes over multiple scales. *Water Resources Research*, *51*(6), 3837–3866. https://doi.org/10.1002/2015WR017016

Blackmore, D. P. T., Ellis, J., & Riley, P. J. (1996). Treatment of a vanadium-containing effluent by adsorption/coprecipitation with iron oxyhydroxide. *Water Research*, *30*(10), 2512–2516. https://doi.org/10.1016/0043-1354(96)00080-2

Blanchard, P. E. R., Hayes, J. R., Grosvenor, A. P., Rowson, J., Hughes, K., & Brown, C. (2015). Investigating the Geochemical Model for Molybdenum Mineralization in the JEB Tailings Management Facility at McClean Lake, Saskatchewan: An X-ray Absorption Spectroscopy Study. *Environmental Science & Technology*, *49*(11), 6504–6509. https://doi.org/10.1021/acs.est.5b00528

Bolève, A., Janod, F., Revil, A., Lafon, A., & Fry, J.-J. (2011). Localization and quantification of leakages in dams using time-lapse self-potential measurements associated with salt tracer injection. *Journal of Hydrology*, *403*(3), 242–252. https://doi.org/10.1016/j.jhydrol.2011.04.008

Borch, T., Kretzschmar, R., Kappler, A., Cappellen, P. V., Ginder-Vogel, M., Voegelin, A., & Campbell, K. (2010). Biogeochemical Redox Processes and their Impact on Contaminant Dynamics. *Environmental Science & Technology*, *44*(1), 15–23. https://doi.org/10.1021/es9026248

Bostick, B. C., Fendorf, S., & Helz, G. R. (2003). Differential Adsorption of Molybdate and Tetrathiomolybdate on Pyrite (FeS2). *Environmental Science & Technology*, *37*(2), 285–291. https://doi.org/10.1021/es0257467

Buglyó, P., Crans, D. C., Nagy, E. M., Lindo, R. L., Yang, L., Smee, J. J., Jin, W., Chi, L.-H., Godzala, M. E., & Willsky, G. R. (2005). Aqueous Chemistry of the VanadiumIII (VIII) and the VIII−Dipicolinate Systems and a Comparison of the Effect of Three Oxidation States of Vanadium Compounds on Diabetic Hyperglycemia in Rats. *Inorganic Chemistry*, *44*(15), 5416–5427. https://doi.org/10.1021/ic048331q

Burke, I. T., Mayes, W. M., Peacock, C. L., Brown, A. P., Jarvis, A. P., & Gruiz, K. (2012). Speciation of Arsenic, Chromium, and Vanadium in Red Mud Samples from the Ajka Spill

Site, Hungary. *Environmental Science & Technology*, *46*(6), 3085–3092. https://doi.org/10.1021/es3003475

CAPP. (2018). *Canadian Association of Petroleum Producers (CAPP)*. https://www.capp.ca

Chalaturnyk, R. J., Scott, J. D., & Özüm, B. (2002). Management of Oil Sands Tailings. *Petroleum Science and Technology*, *20*(9–10), 1025–1046. https://doi.org/10.1081/LFT-120003695

Chung. (1996). *Leachability of cokes from Syncrude stockpiles*. *March*, 50–53.

Cilia, C. R. C. 1992-. (2018). *Characterizing the Physical and Chemical Mass Transport of Dissolved Salts in Layered Oil Sands Waste Undergoing Reclamation* [Thesis, University of Saskatchewan]. https://harvest.usask.ca/handle/10388/8323

Conlan, M. J. W., Mayer, K. U., Blaskovich, R., & Beckie, R. D. (2012). Solubility controls for molybdenum in neutral rock drainage. *Geochemistry: Exploration, Environment, Analysis*, *12*(1), 21–32. https://doi.org/10.1144/1467-7873/10-RA-043

Cordero, P. R. F., Bennett, R. M., Bautista, G. S., Aguilar, J. P. P., & Dedeles, G. R. (2015). Degradation of Nickel Protoporphyrin Disodium and Vanadium Oxide Octaethylporphyrin by Philippine Microbial Consortia. *Bioremediation Journal*, *19*(2), 93–103. https://doi.org/10.1080/10889868.2013.827616

Cruywagen, J. J. (1999). Protonation, Oligomerization, and Condensation Reactions of Vanadate(V), Molybdate(vi), and Tungstate(vi). In A. G. Sykes (Ed.), *Advances in Inorganic Chemistry* (Vol. 49, pp. 127–182). Academic Press. https://doi.org/10.1016/S0898-8838(08)60270-6

Cruywagen, J. J., Heyns, J. B. B., & Westra, A. N. (1996). Protonation Equilibria of Mononuclear Vanadate: Thermodynamic Evidence for the Expansion of the Coordination Number in VO2+. *Inorganic Chemistry*, *35*(6), 1556–1559. Scopus.

Das, A. K., Chakraborty, R., Cervera, M. L., & de la Guardia, M. (2007). A review on molybdenum determination in solid geological samples. *Talanta*, *71*(3), 987–1000. https://doi.org/10.1016/j.talanta.2006.07.017

Dechaine, G. P., & Gray, M. R. (2010). Chemistry and Association of Vanadium Compounds in Heavy Oil and Bitumen, and Implications for Their Selective Removal. *Energy & Fuels*, *24*(5), 2795–2808. https://doi.org/10.1021/ef100173j

Elvingson, K., González Baró, A., & Pettersson, L. (1996). Speciation in Vanadium Bioinorganic Systems. 2. An NMR, ESR, and Potentiometric Study of the Aqueous

H+−Vanadate−Maltol System. *Inorganic Chemistry*, *35*(11), 3388–3393. https://doi.org/10.1021/ic951195s

Essilfie-Dughan, J., Pickering, I. J., Hendry, M. J., George, G. N., & Kotzer, T. (2011). Molybdenum Speciation in Uranium Mine Tailings Using X-Ray Absorption Spectroscopy. *Environmental Science & Technology*, *45*(2), 455–460. https://doi.org/10.1021/es102954b

Fedorak, P. M., & Coy, D. L. (2006). Oil sands cokes affect microbial activities. *Fuel*, *85*(12), 1642–1651. https://doi.org/10.1016/j.fuel.2006.02.015

Gamal El-Din, M., Fu, H., Wang, N., Chelme-Ayala, P., Pérez-Estrada, L., Drzewicz, P., Martin, J. W., Zubot, W., & Smith, D. W. (2011). Naphthenic acids speciation and removal during petroleum-coke adsorption and ozonation of oil sands process-affected water. *Science of The Total Environment*, *409*(23), 5119–5125. https://doi.org/10.1016/j.scitotenv.2011.08.033

Genuchten, M. T. V. (1982). *Analytical Solutions of the One-dimensional Convective-dispersive Solute Transport Equation*. U.S. Department of Agriculture, Agricultural Research Service.

Gibson, J. J., Fennell, J., Birks, S. J., Yi, Y., Moncur, M. C., Hansen, B., & Jasechko, S. (2013). Evidence of discharging saline formation water to the Athabasca River in the oil sands mining region, northern Alberta. *Canadian Journal of Earth Sciences*, *50*(12), 1244–1257. https://doi.org/10.1139/cjes-2013-0027

Goldberg, S., & Forster, H. S. (1998). FACTORS AFFECTING MOLYBDENUM ADSORPTION BY SOILS AND MINERALS. *Soil Science*, *163*(2), 109–114.

Goldberg, S., Forster, H. S., & Godfrey, C. L. (1996). Molybdenum Adsorption on Oxides, Clay Minerals, and Soils. *Soil Science Society of America Journal*, *60*(2), 425–432. https://doi.org/10.2136/sssaj1996.03615995006000020013x

Gray, M. R. (2015). *Upgrading Oilsands bitumen and Heavy Oil* (1st ed.). The University of Alberta Press, Edmonto, Alberta.

Grosjean, E., Adam, P., Connan, J., & Albrecht, P. (2004). Effects of weathering on nickel and vanadyl porphyrins of a Lower Toarcian shale of the Paris basin11Associate editor: G. Logan. *Geochimica et Cosmochimica Acta*, *68*(4), 789–804. https://doi.org/10.1016/S0016-7037(03)00496-4

Gustafsson, J. P. (2018). *Visual MINTEQ version.3.1 https://vminteq.lwr.kth.se/*. https://vminteq.lwr.kth.se/

Gustafsson, J. P. (2019). Vanadium geochemistry in the biogeosphere –speciation, solid-solution interactions, and ecotoxicity. *Applied Geochemistry*, *102*, 1–25. https://doi.org/10.1016/j.apgeochem.2018.12.027

Gustafsson, J. P., & Tiberg, C. (2015). Molybdenum binding to soil constituents in acid soils: An XAS and modelling study. *Chemical Geology*, *417*, 279–288. https://doi.org/10.1016/j.chemgeo.2015.10.016

Har, S. H. (1981). *Characterization of oil sands fluid coke*. ERA. https://doi.org/10.7939/R3B853P38

Hein, F. J., & Cotterill, D. K. (2006). The Athabasca Oil Sands—A Regional Geological Perspective, Fort McMurray Area, Alberta, Canada. *Natural Resources Research*, *15*(2), 85–102. https://doi.org/10.1007/s11053-006-9015-4

Helz, G. R., Miller, C. V., Charnock, J. M., Mosselmans, J. F. W., Pattrick, R. A. D., Garner, C. D., & Vaughan, D. J. (1996). Mechanism of molybdenum removal from the sea and its concentration in black shales: EXAFS evidence. *Geochimica et Cosmochimica Acta*, *60*, 3631–3642. https://doi.org/10.1016/0016-7037(96)00195-0

Holden, A. A., Mayer, K. U., & Ulrich, A. C. (2012). Evaluating methods for quantifying cation exchange in mildly calcareous sediments in Northern Alberta. *Applied Geochemistry*, *27*(12), 2511–2523.

Huang, J.-H., Huang, F., Evans, L., & Glasauer, S. (2015). Vanadium: Global (bio)geochemistry. *Chemical Geology*, *C*(417), 68–89. https://doi.org/10.1016/j.chemgeo.2015.09.019

Hubbard, S., & Linde, N. (2011). *Hydrogeophysics. In: Wilderer P (ed) Treatise on water science, 1. Academic, Oxford, pp 401–434*.

Huerta-Diaz, M. A., Tessier, A., & Carignan, R. (1998). Geochemistry of trace metals associated with reduced sulfur in freshwater sediments. *Applied Geochemistry*, *13*(2), 213–233. https://doi.org/10.1016/S0883-2927(97)00060-7

Hummel, W., & Curti, E. (2003). Nickel Aqueous Speciation and Solubility at Ambient Conditions: A Thermodynamic Elegy. *Monatshefte Für Chemie / Chemical Monthly*, *134*(7), 941–973. https://doi.org/10.1007/s00706-003-0010-8

Jack, T. R., Sullivan, E. A., & Zajic, J. E. (1979). Comparison of the structure and composition of cokes from the thermal cracking of Athabasca Oil Sands bitumen. *Fuel*, *58*(8), 585–588. https://doi.org/10.1016/0016-2361(79)90007-3

Jensen-Fontaine, M. (2012). *Vanadium Speciation in Samples Relevant to the Athabasca Oil Sands Region. MSC. Thesis*. University of Alberta, Edmonton, AB.

Jensen-Fontaine, M., Norwood, W. P., Brown, M., Dixon, D. G., & Le, X. C. (2014). Uptake and Speciation of Vanadium in the Benthic Invertebrate Hyalella azteca. *Environmental Science & Technology*, *48*(1), 731–738. https://doi.org/10.1021/es403252k

Kaminsky, H. (2014). Demystifying the Methylene Blue Index. *Fourth International Oil Sands Tailings Conference*, 221–229.

Kasperski, K. L., & Mikula, R. J. (2011). Waste Streams of Mined Oil Sands: Characteristics and Remediation. *Elements*, *7*(6), 387–392. https://doi.org/10.2113/gselements.7.6.387

Kessler, S., & Hendry, M. J. (2006). Geochemistry and leaching of coke from Syncrude and Suncore sites. *University of Saskatchewan, Geological Science, Saskatoon*.

Kuznetsov, P., Kuznetsova, A., Foght, J. M., & Siddique, T. (2015). Oil sands thickened froth treatment tailings exhibit acid rock drainage potential during evaporative drying. *Science of The Total Environment*, *505*, 1–10. https://doi.org/10.1016/j.scitotenv.2014.09.093

Larson, J. W. (1995). Thermochemistry of Vanadium(5+) in Aqueous Solutions. *Journal of Chemical & Engineering Data*, *40*(6), 1276–1280. https://doi.org/10.1021/je00022a030

Lewan, M. D. (1984). Factors controlling the proportionality of vanadium to nickel in crude oils. *Geochimica et Cosmochimica Acta*, *48*(11), 2231–2238. https://doi.org/10.1016/0016-7037(84)90219-9

Lewan, M. D., & Maynard, J. B. (1982). Factors controlling enrichment of vanadium and nickel in the bitumen of organic sedimentary rocks. *Geochimica et Cosmochimica Acta*, *46*(12), 2547–2560. https://doi.org/10.1016/0016-7037(82)90377-5

Li, X. S., Glasauer, S., & Le, X. C. (2007). Speciation of vanadium in oilsand coke and bacterial culture by high performance liquid chromatography inductively coupled plasma mass spectrometry. *Analytica Chimica Acta*, *648*(1), 128. https://doi.org/10.1016/j.aca.2009.06.053

Li, X. S., Glasauer, S., & Le, X. C. (2009). Erratum to "Speciation of vanadium in oilsand coke and bacterial culture by high performance liquid chromatography inductively coupled plasma mass spectrometry" [Anal. Chim. Acta 602 (2007) 17–22]. *Analytica Chimica Acta*, *648*(1), 128. https://doi.org/10.1016/j.aca.2009.06.053

Li, X. S., & Le, X. C. (2007). Speciation of vanadium in oilsand coke and bacterial culture by high performance liquid chromatography inductively coupled plasma mass spectrometry. *Analytica Chimica Acta*, *602*(1), 17–22. https://doi.org/10.1016/j.aca.2007.09.004

Light, T. S. (1972). Standard solution for redox potential measurements. *Analytical Chemistry*, *44*(6), 1038–1039. https://doi.org/10.1021/ac60314a021

Lindberg, R. D., & Runnells, D. D. (1984). Ground water redox reactions: An analysis of equilibrium state applied to eh measurements and geochemical modeling. *Science (New York, N.Y.)*, *225*(4665), 925–927. https://doi.org/10.1126/science.225.4665.925

Lindsay, M. B. J., Moncur, M. C., Bain, J. G., Jambor, J. L., Ptacek, C. J., & Blowes, D. W. (2015). Geochemical and mineralogical aspects of sulfide mine tailings. *Applied Geochemistry*, *57*, 157–177. https://doi.org/10.1016/j.apgeochem.2015.01.009

Lindsay, M. B. J., Vessey, C. J., & Robertson, J. M. (2019). Mineralogy and geochemistry of oil sands froth treatment tailings: Implications for acid generation and metal(loid) release. *Applied Geochemistry*, *102*, 186–196. https://doi.org/10.1016/j.apgeochem.2019.02.001

Liu, J., Xu, Z., & Masliyah, J. (2005). Processability of Oil Sand Ores in Alberta. *Energy & Fuels*, *19*(5), 2056–2063. https://doi.org/10.1021/ef050091r

Luther, G. W., Meyerson, A. L., Krajewski, J. J., & Hires, R. (1980). Metal sulfides in estuarine sediments. *Journal of Sedimentary Research*, *50*(4), 1117–1120. https://doi.org/10.1306/212F7B94-2B24-11D7-8648000102C1865D

Martínez-Pagán, P., Jardani, A., Revil, A., & Haas, A. (2010). Self-potential monitoring of a salt plume. *GEOPHYSICS*, *75*(4), WA17–WA25. https://doi.org/10.1190/1.3475533

Masliyah, J., Zhou, Z. J., Xu, Z., Czarnecki, J., & Hamza, H. (2004). Understanding Water-Based Bitumen Extraction from Athabasca Oil Sands. *The Canadian Journal of Chemical Engineering*, *82*(4), 628–654. https://doi.org/10.1002/cjce.5450820403

McCann, N., Imle, M., & Hasse, H. (2015). Carbonate complexes of vanadate. *Polyhedron*, *95*, 81–85. https://doi.org/10.1016/j.poly.2015.03.004

McCann, N., Wagner, M., & Hasse, H. (2013). A thermodynamic model for vanadate in aqueous solution – equilibria and reaction enthalpies. *Dalton Transactions*, *42*(7), 2622–2628. https://doi.org/10.1039/C2DT31993D

Nakata, C., Qualizza, C., MacKinnon, M., & Renault, S. (2011). Growth and Physiological Responses of Triticum aestivum and Deschampsia caespitosa Exposed to Petroleum Coke. *Water, Air, & Soil Pollution*, *216*(1), 59–72. https://doi.org/10.1007/s11270-010-0514-x

Naudet, V., & Revil, A. (2005). A sandbox experiment to investigate bacteria-mediated redox processes on self-potential signals. *Geophysical Research Letters*, *32*(11). https://doi.org/10.1029/2005GL022735

Nesbitt, J. A. (2016). *Geochemical Investigation of fluid petroleum coke deposits at an oil sands mine in northern Alberta, Canada*. University of Saskatchewan Press, Saskatchewan,Canada.

Nesbitt, J. A., & Lindsay, M. B. J. (2017). Vanadium Geochemistry of Oil Sands Fluid Petroleum Coke. *Environmental Science & Technology*, *51*(5), 3102–3109. https://doi.org/10.1021/acs.est.6b05682

Nesbitt, J. A., Lindsay, M. B. J., & Chen, N. (2017). Geochemical characteristics of oil sands fluid petroleum coke. *Applied Geochemistry*, *76*, 148–158. https://doi.org/10.1016/j.apgeochem.2016.11.023

Nesbitt, J. A., Robertson, J. M., Swerhone, L. A., & Lindsay, M. B. J. (2018). Nickel geochemistry of oil sands fluid petroleum coke deposits, Alberta, Canada. *FACETS*. https://doi.org/10.1139/facets-2017-0115

Nordstrom, D. K. (1977). Thermochemical redox equilibria of ZoBell's solution. *Geochimica et Cosmochimica Acta*, *41*, 1835–1841. https://doi.org/10.1016/0016-7037(77)90215-0

Ntarlagiannis, D., Williams, K. H., Slater, L., & Hubbard, S. (2005). Low-frequency electrical response to microbial induced sulfide precipitation. *Journal of Geophysical Research: Biogeosciences*, *110*(G2). https://doi.org/10.1029/2005JG000024

Pajdowski, L. (1966). A spectrophotometric study of the hydrolysis of vanadium (III) ion. *Journal of Inorganic and Nuclear Chemistry*, *28*(2), 433–442. https://doi.org/10.1016/0022-1902(66)80322-6

Pajdowski, L., & Jeżowska-Trzebiatowska, B. (1966). A magnetochemical study of the hydrolysis of vanadium (III) ion. *Journal of Inorganic and Nuclear Chemistry*, *28*(2), 443–446. https://doi.org/10.1016/0022-1902(66)80323-8

Parkhurst, D. L., & Appelo, C. A. J. (2013). *Description of Input and Examples for PHREEQC Version 3—A Computer Program for Speciation, Batch-Reaction, One-Dimensional Transport, and Inverse Geochemical Calculations. In: Techniques and Methods 6-A43, U.S. Geological Survey, Denver, USA, 497 pp.*

Peacock, C. L., & Sherman, D. M. (2004). Vanadium(V) adsorption onto goethite (α-FeOOH) at pH 1.5 to 12: A surface complexation model based on ab initio molecular geometries and EXAFS spectroscopy. *Geochimica et Cosmochimica Acta*, *68*(8), 1723–1733. https://doi.org/10.1016/j.gca.2003.10.018

Perkins, T. K., & Johnston, O. C. (1963). A Review of Diffusion and Dispersion in Porous Media. *Society of Petroleum Engineers Journal*, *3*(01), 70–84. https://doi.org/10.2118/480-PA

Plumlee, G. S. (1999). *The Environmental Geology of Mineral Deposits. In: Plumlee, G.S., Logdson, M.J. (Eds.), The Envronmental Geochemistry of Mineral Deposits, Part A. Processes. Techniques, and Health Issues, pp. 71-116. Littleton*. 46.

Pourrezaei, P., Alpatova, A., Chelme-Ayala, P., Perez-Estrada, L. A., Jensen-Fontaine, M., Le, X. C., & Gamal El-Din, M. (2014). Impact of petroleum coke characteristics on the adsorption of the organic fractions from oil sands process-affected water. *International Journal of Environmental Science and Technology*, *11*(7), 2037–2050. https://doi.org/10.1007/s13762-013-0406-x

Price, J. S., McLaren, R. G., & Rudolph, D. L. (2010). Landscape restoration after oil sands mining: Conceptual design and hydrological modelling for fen reconstruction. *International Journal of Mining, Reclamation and Environment*, *24*(2), 109–123. https://doi.org/10.1080/17480930902955724

Puttaswamy, N., & Liber, K. (2011). Identifying the causes of oil sands coke leachate toxicity to aquatic invertebrates. *Environmental Toxicology and Chemistry*, *30*(11), 2576–2585. https://doi.org/10.1002/etc.653

Puttaswamy, N., & Liber, K. (2012). Influence of inorganic anions on metals release from oil sands coke and on toxicity of nickel and vanadium to Ceriodaphnia dubia. *Chemosphere*, *86*(5), 521–529. https://doi.org/10.1016/j.chemosphere.2011.10.018

Puttaswamy, N., Turcotte, D., & Liber, K. (2010). Variation in toxicity response of Ceriodaphnia dubia to Athabasca oil sands coke leachates. *Chemosphere*, *80*(5), 489–497. https://doi.org/10.1016/j.chemosphere.2010.04.071

Revil, A., Karaoulis, M., Johnson, T., & Kemna, A. (2012). Review: Some low-frequency electrical methods for subsurface characterization and monitoring in hydrogeology. *Hydrogeology Journal*, *20*(4), 617–658. https://doi.org/10.1007/s10040-011-0819-x

Rickard, D. (2012). Chapter 7—Metal Sequestration by Sedimentary Iron Sulfides. In D. Rickard (Ed.), *Developments in Sedimentology* (Vol. 65, pp. 287–317). Elsevier. https://doi.org/10.1016/B978-0-444-52989-3.00007-6

Robertson, J. M., Nesbitt, J. A., & Lindsay, M. B. J. (2019). Aqueous- and solid-phase molybdenum geochemistry of oil sands fluid petroleum coke deposits, Alberta, Canada. *Chemosphere*, *217*, 715–723. https://doi.org/10.1016/j.chemosphere.2018.11.064

Rubin, Y., & Hubbard, S. (2005). *Hydrogeophysics. Water and Science Technology Library 50, Springer, Houten, The Netherlands*.

Santamarina, J. C., Klein, K. A., Wang, Y. H., & Prencke, E. (2002). Specific surface: Determination and relevance. *Canadian Geotechnical Journal*, *39*(1), 233–241.

Sill, W. R. (1983). Self-potential modeling from primary flows. *GEOPHYSICS*, *48*(1), 76–86. https://doi.org/10.1190/1.1441409

Simhayov, R. B., Price, J. S., Smeaton, C. M., Parsons, C., Rezanezhad, F., & Van Cappellen, P. (2017). Solute pools in Nikanotee Fen watershed in the Athabasca oil sands region. *Environmental Pollution*, *225*, 150–162. https://doi.org/10.1016/j.envpol.2017.03.038

Singha, K., Day-Lewis, F. D., Johnson, T., & Slater, L. D. (2015). Advances in interpretation of subsurface processes with time-lapse electrical imaging. *Hydrological Processes*, *29*(6), 1549–1576. https://doi.org/10.1002/hyp.10280

Slater, L., Binley, A., Versteeg, R., Cassiani, G., Birken, R., & Sandberg, S. (2002). A 3D ERT study of solute transport in a large experimental tank. *Journal of Applied Geophysics*, *49*(4), 211–229. https://doi.org/10.1016/S0926-9851(02)00124-6

Smedley, P. L., & Kinniburgh, D. G. (2017). Molybdenum in natural waters: A review of occurrence, distributions and controls. *Applied Geochemistry*, *84*, 387–432. https://doi.org/10.1016/j.apgeochem.2017.05.008

Smith, R. M., Martell, A. E., & Motekaitis, R. J. (2004). *NIST critically selected stability constants of metal complexes database. NIST, Gaithersburg, MD, USA NIST standard reference database 46, version 8.0.*

Sobkowicz, J., McKenna, G., & Dawson, R. (2012). *Oil Sands Tailings Technology Deployment Roadmap*. https://www.cosia.ca/uploads/documents/id10/Tailings%20Roadmap%20Volume%202%20June%202012.pdf

Strong, D., & Filby, R. H. (1987). Vanadyl Porphyrin Distribution in the Alberta Oil-Sand Bitumens. In *Metal Complexes in Fossil Fuels* (Vol. 344, pp. 154–172). American Chemical Society. https://doi.org/10.1021/bk-1987-0344.ch010

Swerhone, L. A. 1993-. (2018). *Trace Element Mobility in Layered Oil Sands Mine Wastes* [Thesis, University of Saskatchewan]. https://harvest.usask.ca/handle/10388/9657

Vessey, C. J., & Lindsay, M. B. J. (2020). Aqueous Vanadate Removal by Iron(II)-Bearing Phases under Anoxic Conditions. *Environmental Science & Technology*, *54*(7), 4006–4015. https://doi.org/10.1021/acs.est.9b06250

Vessey, C. J., Schmidt, M. P., Abdolahnezhad, M., Peak, D., & Lindsay, M. B. J. (2020). Adsorption of (Poly)vanadate onto Ferrihydrite and Hematite: An In Situ ATR–FTIR Study. *ACS Earth and Space Chemistry*, *4*(4), 641–649. https://doi.org/10.1021/acsearthspacechem.0c00027

Vitt, D. H., Halsey, L. A., & Thormann, M. N. (1996). *Peatland inventory of Alberta, Phase 1: Overview of peatland resources in the natural regions and subregions of the province. Edmonton: Alberta Environmental Protection*.

Wällstedt, T., Björkvald, L., & Gustafsson, J. P. (2010). Increasing concentrations of arsenic and vanadium in (southern) Swedish streams. *Applied Geochemistry*, *25*(8), 1162–1175. https://doi.org/10.1016/j.apgeochem.2010.05.002

Wang, D., & Sañudo Wilhelmy, S. A. (2009). Vanadium speciation and cycling in coastal waters. *Marine Chemistry*, *117*(1), 52–58. https://doi.org/10.1016/j.marchem.2009.06.001

Wanty, R. B., & Goldhaber, M. B. (1992). Thermodynamics and kinetics of reactions involving vanadium in natural systems: Accumulation of vanadium in sedimentary rocks. *Geochimica et Cosmochimica Acta*, *56*(4), 1471–1483. https://doi.org/10.1016/0016-7037(92)90217-7

Wehrli, B., & Stumm, W. (1989). Vanadyl in natural waters: Adsorption and hydrolysis promote oxygenation. *Geochimica et Cosmochimica Acta*, *53*(1), 69–77. https://doi.org/10.1016/0016-7037(89)90273-1

Williams, K. H., Ntarlagiannis, D., Slater, L. D., Dohnalkova, A., Hubbard, S. S., & Banfield, J. F. (2005). Geophysical Imaging of Stimulated Microbial Biomineralization. *Environmental Science & Technology*, *39*(19), 7592–7600. https://doi.org/10.1021/es0504035

Wright, M. T., & Belitz, K. (2010). Factors Controlling the Regional Distribution of Vanadium in Groundwater. *Groundwater*, *48*(4), 515–525. https://doi.org/10.1111/j.1745-6584.2009.00666.x

Wright, M. T., Stollenwerk, K. G., & Belitz, K. (2014). Assessing the solubility controls on vanadium in groundwater, northeastern San Joaquin Valley, CA. *Applied Geochemistry*, *48*, 41–52. https://doi.org/10.1016/j.apgeochem.2014.06.025

Xu, N., Braida, W., Christodoulatos, C., & Chen, J. (2013). A Review of Molybdenum Adsorption in Soils/Bed Sediments: Speciation, Mechanism, and Model Applications. *Soil and Sediment Contamination: An International Journal*, *22*(8), 912–929. https://doi.org/10.1080/15320383.2013.770438

Yuan-Hui, L., & Gregory, S. (1974). Diffusion of ions in sea water and in deep-sea sediments. *Geochimica et Cosmochimica Acta*, *38*(5), 703–714. https://doi.org/10.1016/0016-7037(74)90145-8

Zajic, Jack TR, Sullivan EA, & Woodfielld G. (1977). *Metals, microbes and bituminous sands: Chemical and microbially-assisted leaching of Athabasca oil sands cokes. Alberta Oil Sands Technology and Research Authority (AOSTRA), Edmonton, Alberta, Canada. Agreement #20.*

ZoBell, C. E. (1946). Studies on Redox Potential of Marine Sediments. *AAPG Bulletin*, *30*(4), 477–513. https://doi.org/10.1306/3D933808-16B1-11D7-8645000102C1865D

Zubot, W. (2010). *Removal of Naphthenic Acid from oil Sands Process Water using Petroleum Coke*. University of Alberta, Dept. of Civil & Environmental Engineering, Lake Louise, Alberta, Canada.

Zubot, W., MacKinnon, M. D., Chelme-Ayala, P., Smith, D. W., & Gamal El-Din, M. (2012). Petroleum coke adsorption as a water management option for oil sands process-affected water. *Science of The Total Environment*, *427–428*, 364–372. https://doi.org/10.1016/j.scitotenv.2012.04.024

28, 364–372. https://doi.org/10.1016/j.scitotenv.2012.04.024

Zuliani, J. E., Miyata, T., Mizoguchi, T., Feng, J., Kirk, D. W., & Jia, C. Q. (2016). Characterization of vanadium in oil sands fluid petroleum coke using electron microscopy. *Fuel*, *178*, 124–128. https://doi.org/10.1016/j.fuel.2016.03.015

APPENDIX A: FORWARD AND INVERSE GEOPHYSICAL MODELING

A.1. Electrical Resistivity

The electrical conductivity of a porous material, σ_0 (express in S m^{-1}), is the reciprocal of the electrical resistivity, ρ_0 (express in ohm.m). At the macroscopic scale, the total electrical current density J (A m^{-2}) which represent the flux of electrical charge (C m^{-2} s^{-1}) within a saturated porous media with brine is given by equation A.1 (Sill, 1983).

$$J = \sigma_0 \mathrm{E} + J_s \qquad (A.1)$$

Equation A.1 relates the conduction current density J (in A m^{-2}) to the electrical field E (express in V m^{-1} and could be written as $\mathrm{E} = -\nabla\psi$). Where J is the total electrical current density, the second term (J_S) is cancelled because the self-potential field automatically is cancelled during the resistivity measurements. Therefore, equation A.1 could be written as:

$$J = \sigma_0 \mathrm{E} \qquad (\mathrm{A}.2)$$

$$J = \sigma_0 (-\nabla \psi) \qquad (A.3)$$

$$\nabla * E = 0 \qquad (A.4)$$

The equation A.3 is used to satisfy A.4 in the low-frequency limit of the Maxwell equation and ψ in equation A.3 is the electrical potential (express in V). In addition, the continuity equation could be written as below:

$$\nabla . J = \xi \qquad (\mathrm{A}.5)$$

Where ξ is correspond to volumetric charge source term ($\xi > 0$) or sink term ($\xi < 0$) and is express in A m^{-3}. The continuity equation is simply $\nabla \cdot \mathrm{J} = 0$ at outside area where the current is injected or retrieved. This leads to the Poisson equation, which could be solved using boundary conditions.

$$J = \sigma_0 (-\nabla \psi) \qquad (A.6)$$

$$\nabla . J = \nabla(-\sigma_0 \nabla \psi) = 0 \qquad (A.7)$$

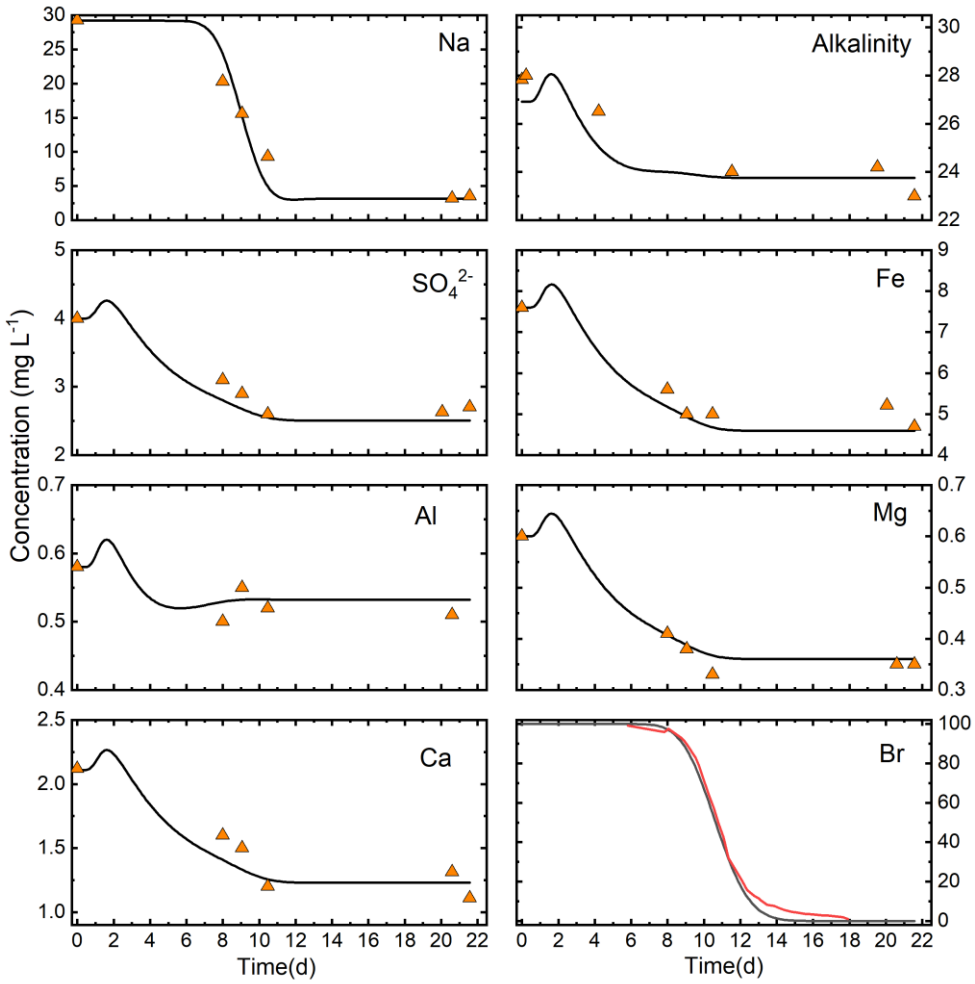

Figure A.1. Measured concentrations in the large column effluent (orange triangles) and calculated concentrations in forward modeling using COMSOL Multiphysics (black line) for the first tracer test-Decay part. Concentrations of Na, SO_4^{2-}, Al, Ca, Fe, and Mg quantified with inductively coupled plasma–optical emission spectroscopy (ICP-OES), while alkalinity was determined by titration. The red line is the concentration of Br within the column effluent measured with bromide electrode.

APPENDIX B: MASS PACKED INSIDE COLUMNS

Table B.1. Masses of materials used in packing the small columns.

Column	Sand (g)	Coke (g)	Sand (g)
DC - DI[a]	226.13	822.81	249.46
SC - DI	245.76	781.72	228.36
DC - OPSW[b]	215.51	804.12	233.51
SC - OSPW	225.04	791.12	239.84
DC - ARD[c]	221.13	765.35	255.54
SC - ARD	230.67	789.99	224

[a]DI: Deionized water

[b]OSPW: Oil sand process-affected water

[c]ARD: Acid rock drainage

Table B.2. Masses of materials used in packing the large column.

Length (cm)	Material	Weight (kg)
8.5 (top)	Sand	3.20
10	Coke	2.11
10	Coke	2.23
10	Coke	2.23
10	Coke	1.96
10	Coke	2.12
8.5 (base)	Sand	3.00

APPENDIX C: CATION EXCHANGE CAPACITY

Methods from Holden et al. (2012) and Santamarina et al. (2002) were combined to measure the cation exchange capacity (CEC) of the coke particles. Frist, 90 g of oven dried fresh dry and slurry coke were soaked with 0.5 L Milli-Q water in a 1 L clean beaker and stirred for 20 min. Since we expected a very low CEC value for fresh dry coke, it was titrated with 0.0001 N methylene blue (MB), while the slurry coke was titrated with 0.001 N MB. In contrast with original methods, 0.0001 N and 0.001 N MB were used in this experiment instead of 0.01 N MB (to prevent the formation of dimers or other orientations of the methylene blue molecules which could over-estimate the CEC value; also, the lower concentration results in a more sensitive end point). MB was added in 1 mL increments and stirred for 1 min. A glass stir rod was used to place one drop of the suspension on Whatman 42 ashless filter paper (spot test). At each step, 5 mL of suspension was centrifuged, then 2 mL of the solution was pipetted into 3 mL cuvettes and the absorption was measured using a DR2800 Spectrophotometer at a single wavelength of 664 nm (titration method). Based on the MB standard curve, MB concentration in the solution was measured. The centrifuged solution was returned into the beaker, the amount of absorbed MB was plotted against the added MB, and the divergent point of the graph compared with line 45 is the point of complete cation replacement, meaning all available sites are occupied with MB. MB was added until the final point was reached (consistent halo), meaning all available sites on the surface are replaced with methylene blue molecules. Adding MB was continued even after the halo point to see if the halo was consistent. Because of non-linear methylene blue absorption, Absorbance should be lower than 1, otherwise dilution should be performed. Finally, the CEC value is measured based on amount of MB to reach the halo point and the divergent point (Spot and titration method).

Following Kaminsky (2014), 1 g of oven dried sample was soaked in 50 mL Milli-Q water inside a clean 250 mL beaker (n = 8). One beaker was titrated with 0.0001 N MB (due to very low CEC values and the small amount of coke particles that were used in this part of the experiment) until it reached the end halo point (spot test). At this point, four beakers were titrated with smaller amount of MB than the end point (in 1 mL increments), and three were titrated with a higher amounts than the end point (in 1 mL increments). All beakers were stirred for 2 h and one drop was placed on Whatman 42 ashless filter paper for each beaker to get the halo point (spot test). The beakers were allowed to settle overnight. The next day, 10 mL from each beaker was centrifuged and the MB concentration inside each beaker was measured using a DR2800

Spectrophotometer. The amount of absorbed MB was plotted against the added MB, and the point of complete cation replacement was identified (titration test).

Table C.1. Summary of CEC method (no dispersion).

Reference	Dry Coke	Slurry Coke
Holden, 2012	90 g in 0.5 L, titrated with 0.0001 N	90 g in 0.5 L, titrated with 0.001 N
Kaminsky, 2014 (No acidifying, no dispersion)	1 g in 50 mL titrated with 0.0001 N	1 g in 50 mL titrated with 0.0001 N
	2 g in 50 mL titrated with 0.0001 N	2 g in 50 mL titrated with 0.0001 N
	3 g in 50 mL titrated with 0.0001 N	3 g in 50 mL titrated with 0.0001 N

As fluid petroleum coke does not have a high amount of clay, the dispersion procedure is not needed for our samples. Also, acidifying the samples would dissolve the iron particles on the coke surface which could change the CEC value; therefore, samples were not acidified. As a result, the Kaminsky method was not followed exactly here (no acidifying, no dispersion). Finally, the CEC for both spot and titration methods was measured (equation C.1).

$$CEC\ \left(\frac{meq}{100gr}\right) = \left(\frac{mLsof\ MB * Normality\ of\ MB}{Mass\ of\ dried\ sample\ (gr)}\right) * 100 \qquad (C.1)$$

Table C.2. CEC values for fresh dry coke (no dispersion).

	Titration method	Spot test
1 g, 50 mL MQ[a], 0.0001 N MB	0.02 meq/100 g	0.04 meq/100 g
2 g, 50 mL MQ, 0.0001 N MB	0.03 meq/100 g	0.03 meq/100 g
3 g, 50 mL MQ, 0.0001 N MB	0.02 meq/100 g	0.017 meq/100 g
90 g, 500 mL MQ, 0.0001 N MB	0.049 meq/100 g	0.053 meq/100 g

[a]MQ: Milli-Q water

Table C.3. CEC for fresh slurry coke (no dispersion).

	Titration method	Spot test
1 g, 50 mL MQ[a], 0.0001 N MB	0.19 meq/100 g	0.2 meq/100 g
2 g, 50 mL MQ, 0.0001 N MB	0.205 meq/100 g	0.21 meq/100 g
3 g, 50 mL MQ, 0.0001 N MB	0.20 meq/100 g	0.21 meq/100 g
90 g, 500 mL MQ, 0.001 N MB	0.20 meq/100 g	0.211 meq/100 g

[a]MQ: Milli-Q water

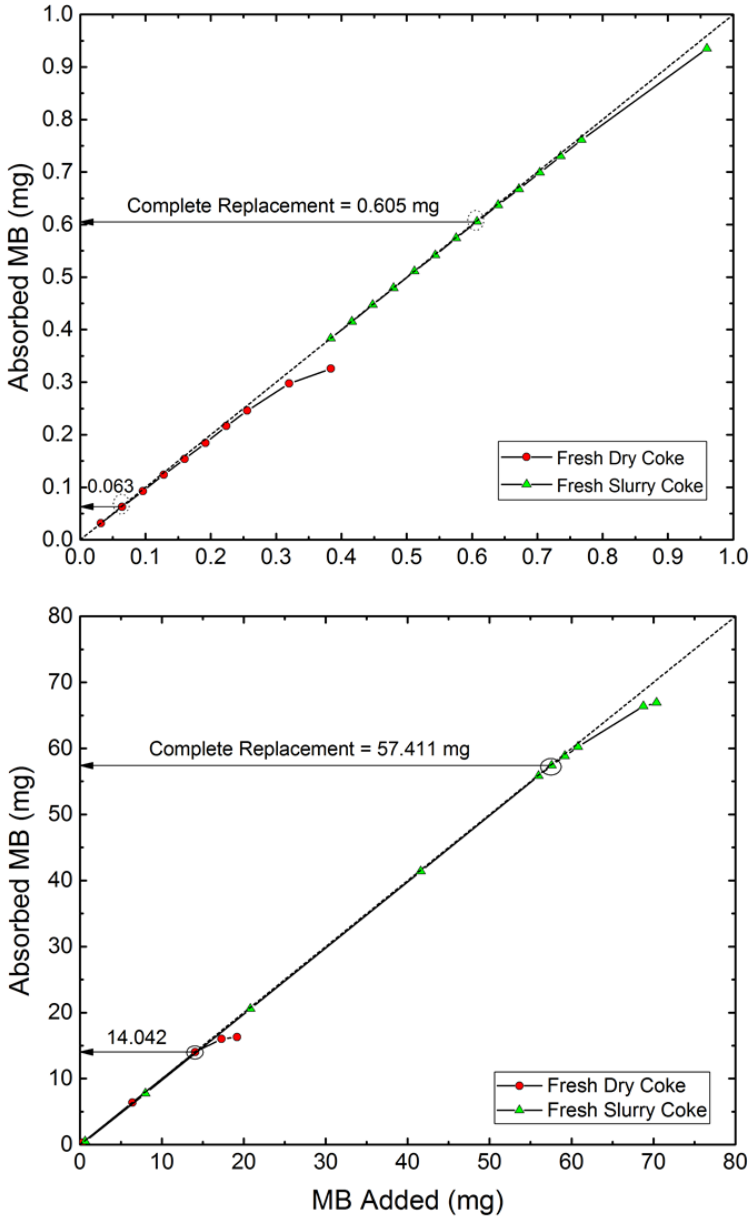

Figure C.1. CEC of fresh dry and fresh slurry coke (titration method). 1 g coke, 50 mL Milli-Q water (MQ), no dispersant (top); 90 g coke, 500 mL MQ, no dispersant (bottom). The normality of methylene blue (MB) was 0.0001 in all cases except for the 90 g of slurry where 0.001 N was used due to the high CEC value.

APPENDIX D: VANADIUM (V) REACTIONS AND FORMATION CONSTANT

Table D.1. Aqueous V(V) reactions and equilibrium constants considered for thermodynamic modeling.

Reaction	log K	Reference
$VO_2^+ + 2H_2O \leftrightarrow VO_4^{3-} + 4H^+$	–29.38	a, b*
$VO_2^+ + 2H_2O \leftrightarrow HVO_4^{2-} + 3H^+$	–15.89	a, b *
$VO_2^+ + 2H_2O \leftrightarrow H_2VO_4^- + 2H^+$	–7.14	a, b *
$2VO_2^+ + 3H_2O \leftrightarrow V_2O_7^{4-} + 6H^+$	–32.88	a, b *
$2VO_2^+ + 3H_2O \leftrightarrow HV_2O_7^{3-} + 5H^+$	–21.58	a, b *
$2VO_2^+ + 3H_2O \leftrightarrow H_2V_2O_7^{2-} + 4H^+$	–11.98	a, b *
$3VO_2^+ + 4H_2O \leftrightarrow HV_3O_{10}^{4-} + 7H^+$	–26.71	c, d*
$4VO_2^+ + 5H_2O \leftrightarrow V_4O_{13}^{6-} + 10H^+$	–43.01	a, b *
$4VO_2^+ + 5H_2O \leftrightarrow HV_4O_{13}^{5-} + 9H^+$	–32.23	a, b *
$4VO_2^+ + 4H_2O \leftrightarrow V_4O_{12}^{4-} + 8H^+$	–20.96	a, b *
$5VO_2^+ + 5H_2O \leftrightarrow V_5O_{15}^{5-} + 10H^+$	–27.43	a, b *
$6VO_2^+ + 6H_2O \leftrightarrow V_6O_{18}^{6-} + 12H^+$	–34.55	a, b *
$10VO_2^+ + 8H_2O \leftrightarrow V_{10}O_{28}^{6-} + 16H^+$	–24.76	a, b *
$10VO_2^+ + 8H_2O \leftrightarrow HV_{10}O_{28}^{5-} + 15H^+$	–17.4	a, b *
$10VO_2^+ + 8H_2O \leftrightarrow H_2V_{10}O_{28}^{4-} + 14H^+$	–13.2	a, b *
$10VO_2^+ + 8H_2O \leftrightarrow H_3V_{10}O_{28}^{3-} + 13H^+$	–8.52	a, b *

[a](Cruywagen et al., 1996)

[b](Cruywagen, 1999)

[c](McCann et al., 2013)

[d](McCann et al., 2015)

[e](Smith et al., 2004)

[f](Larson, 1995)

[g](Elvingson et al., 1996)

*Used in this stud

APPENDIX E: PH POINT OF ZERO CHARGE

Table E.1. Summary of pH of point of zero charge (pH_{PCZ}) for fresh dry coke.

DC1[a]			DC2			DC3		
Initial pH	**Final pH**	**ΔpH**	**Initial pH**	**Final pH**	**ΔpH**	**Initial pH**	**Final pH**	**ΔpH**
2.05	2.42	0.37	2.04	2.5	0.46	2.26	2.47	0.21
2.97	3.23	0.26	3.08	3.36	0.28	3.23	3.3	0.07
3.95	4.26	0.31	4.02	4.37	0.35	4.04	4.64	0.6
4.95	5.31	0.36	5.22	5.56	0.34	4.87	5.63	0.76
5.79	6.14	0.35	6.14	6.38	0.24	5.83	6.13	0.3
7.25	6.77	−0.48	6.73	6.77	0.04	6.88	6.84	−0.04
7.78	6.96	−0.82	8.26	7.04	−1.22	7.7	7.18	−0.52
9.3	8.01	−1.29	9.1	7.21	−1.89	8.82	7.58	−1.24
10.04	9.07	−0.97	9.97	8.34	−1.63	10.3	10.08	−0.22
pH_{PZC}	**6.4**			**6.78**			**6.76**	

[a]DC: Dry coke

Table E.2. Summary of pH of point of zero charge (pH_{PCZ}) for fresh slurry coke.

SC1[a]			SC2			SC3		
Initial pH	**Final pH**	**ΔpH**	**Initial pH**	**Final pH**	**ΔpH**	**Initial pH**	**Final pH**	**ΔpH**
2.04	2.53	0.49	2.04	2.51	0.47	2.28	2.35	0.07
3.05	3.42	0.37	3.13	3.54	0.41	3.24	3.6	0.36
3.91	5.1	1.19	4.04	5.74	1.7	4.03	5.84	1.81
4.84	6.85	2.01	5.04	6.62	1.58	4.75	6.61	1.86
6.24	6.74	0.5	6.26	7.16	0.9	5.8	6.77	0.97
7.23	7.31	0.08	7.05	6.92	−0.13	6.88	7.26	0.38
7.88	7.38	−0.5	8.11	7.51	−0.6	8.01	7.35	−0.66
9.14	7.79	−1.35	9.04	7.64	−1.4	8.92	7.84	−1.08
9.73	8.55	−1.18	9.77	8.3	−1.47	10.3	9.98	−0.32
pH_{PZC}	**7.32**			**6.95**			**7.29**	

[a]SC: Slurry coke

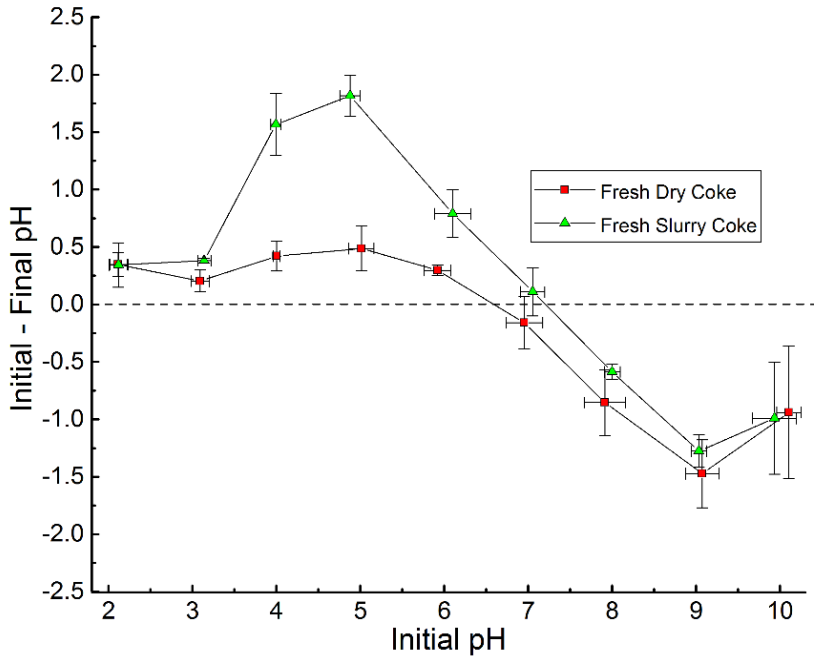

Figure E.1. The pH point of zero charge (pH_{PCZ}) for fresh coke particles (dry and slurry coke).

Table E.3. Summary of point of zero charge (pH_{PCZ}) for leached dry coke (DC) under Deionized water (DI). Column solid samples were divided into four zones (1 to 4) from bottom to top.

DCA – Zone 1			DCA – Zone 4		
Initial pH	**Final pH**	**ΔpH**	**Initial pH**	**Final pH**	**ΔpH**
2.29	2.3	0.01	2.3	2.31	0.01
3.2	3.21	0.01	3.19	3.19	0
4.15	4.2	0.05	4.01	4.09	0.08
5.28	5.38	0.1	5.24	5.31	0.07
6.12	6	−0.12	6.07	5.83	−0.24
7.07	6.74	−0.33	7.09	6.44	−0.65
8.24	7.06	−1.18	8.24	6.72	−1.52
9.18	7.45	−1.73	9.23	7.07	−2.16
9.99	9.33	−0.66	9.92	8.78	−1.14
pH_{PZC}	**5.66**		**5.43**		

Table E.4. Summary of pH of point of zero charge (pH_{PCZ}) for leached slurry coke (SC) under deionized water (DI). Column solid samples were divided into four zones (1 to 4) from bottom to top.

SCD – Zone 1			SCD – Zone 4		
Initia pH	**Final pH**	**ΔpH**	**Initia pH**	**Final pH**	**ΔpH**
2.29	2.32	0.03	2.29	2.48	0.19
3.2	3.59	0.39	3.19	3.3	0.11
4.04	4.39	0.35	3.98	4.43	0.45
5.21	5.42	0.21	5.25	5.79	0.54
6.08	5.94	−0.14	6.01	5.76	−0.25
7.01	6.5	−0.51	6.92	6.25	−0.67
8.23	6.72	−1.51	8.11	6.68	−1.43
9.24	7.8	−1.44	9.19	6.91	−2.28
9.91	8.22	−1.69	9.93	7.66	−2.27
pH_{PZC}	**5.73**		**5.77**		

Table E.5. Summary of pH of point of zero charge (pH_{PCZ}) for leached dry coke (DC) under oil sand process-affected water (OSPW). Column solid samples were divided into four zones (1 to 4) from bottom to top.

DCC – Zone 1			**DCC – Zone 1**		
Initial pH	**Final pH**	**ΔpH**	**Initial pH**	**Final pH**	**ΔpH**
2.22	2.23	0.01	2.3	2.48	0.19
3.06	3.1	0.04	3.17	3.3	0.11
3.84	3.99	0.15	3.99	4.43	0.45
5.12	5.54	0.42	4.71	5.79	0.54
6	6.18	0.18	6.18	5.76	−0.25
6.95	6.78	−0.17	7.08	6.25	−0.67
8.23	7.09	−1.14	8.11	6.68	−1.43
8.88	7.51	−1.37	8.79	6.91	−2.28
9.94	9.45	−0.49	9.84	7.66	−2.27
pH_{PZC}	**6.49**		**6.45**		

Table E.6. Summary of pH of point of zero charge (pH_{PCZ}) for leached dry coke (DC) under oil sand process-affected water (OSPW). Column solid samples were divided into four zones (1 to 4) from bottom to top.

DCC – Zone4			DCC – Zone4			DCC – Zone4		
Initial pH	**Final pH**	**ΔpH**	**Initial pH**	**Final pH**	**ΔpH**	**Initial pH**	**Final pH**	**ΔpH**
2.21	2.21	0	2.29	2.35	0.06	2.28	2.29	0.01
3.06	3.09	0.03	3.24	3.38	0.14	3.24	3.41	0.17
3.82	4.6	0.78	4.14	4.46	0.32	4.03	4.34	0.31
5.11	5.32	0.21	4.78	5.4	0.62	4.89	5.58	0.69
5.79	5.91	0.12	5.85	6.21	0.36	5.8	6.11	0.31
6.76	6.26	−0.5	6.89	6.6	−0.29	6.88	6.61	−0.27
8.25	6.63	−1.62	8.06	7.29	−0.77	7.8	7.15	−0.65
8.83	6.89	−1.94	8.96	7.75	−1.21	9.07	7.76	−1.31
9.94	8.68	−1.26	10.28	10.08	−0.2	10.3	10.08	−0.22
pH_{PZC}	**5.98**		**6.43**			**6.38**		

Table E.7. Summary of pH of point of zero charge (pH_{PCZ}) for leached slurry coke (SC) under oil sand process-affected water (OSPW). Column solid samples were divided into four zones (1 to 4) from bottom to top.

SCF – Zone 1			SCF – Zone 1			SCF – Zone 4		
Initial pH	**Final pH**	**ΔpH**	**Initial pH**	**Final pH**	**ΔpH**	**Initial pH**	**Final pH**	**ΔpH**
2.2	2.21	0.01	2.3	2.35	0.05	2.2	2.22	0.02
3.06	3.2	0.14	3.16	3.59	0.43	3.05	3.24	0.19
3.82	4.45	0.63	4.02	5.02	1	3.82	4.53	0.71
5.11	6.44	1.33	5.2	6.38	1.18	5.16	5.81	0.65
5.77	6.37	0.6	6.26	6.61	0.35	5.77	6.04	0.27
6.71	6.94	0.23	6.95	6.9	−0.05	6.9	6.41	−0.49
8.26	7.22	−1.04	7.7	7.08	−0.62	8.26	6.59	−1.67
8.83	7.31	−1.52	8.73	7.27	−1.46	8.86	6.87	−1.99
9.91	9.21	−0.7	9.87	7.58	−2.29	9.9	7.93	−1.97
pH_{PZC}	**6.99**		**6.86**			**6.17**		

Table E.8. Summary of pH of point of zero charge (pH_{PCZ}) for leached dry coke (DC) under acid rock drainage (ARD). Column solid samples were divided into four zones (1 to 4) from bottom to top.

DCB – Zone 1		
Initial pH	**Final pH**	**ΔpH**
2.3	2.44	0.14
3.2	3.33	0.13
4.09	4.1	0.01
4.92	4.48	−0.44
6.14	5.06	−1.08
7.17	5.77	−1.4
7.71	6.32	−1.39
8.81	6.43	−2.38
9.85	7.49	−2.36
pH_{PZC}	**4.11**	

Table E.9. Summary of pH of point of zero charge (pH_{PCZ}) for leached dry coke (DC) under acid rock drainage (ARD). Column solid samples were divided into four zones (1 to 4) from bottom to top.

DCB – Zone4			DCB – Zone4			DCB – Zone4		
Initial pH	**Final pH**	**ΔpH**	**Initial pH**	**Final pH**	**ΔpH**	**Initial pH**	**Final pH**	**ΔpH**
2.3	2.31	0.01	2.24	2.32	0.08	2.28	2.32	0.04
3.17	3.47	0.3	3.2	3.35	0.15	3.23	3.13	−0.1
4.06	4.48	0.42	4.27	4.46	0.19	4.02	4.22	0.2
4.71	4.98	0.27	4.73	4.74	0.01	4.86	4.86	0
6.19	5.57	−0.62	5.88	5.49	−0.39	5.97	5.68	−0.29
7.08	6.39	−0.69	7.3	6.86	−0.44	6.89	6.62	−0.27
7.74	6.79	−0.95	7.72	6.94	−0.78	7.97	6.94	−1.03
8.78	6.93	−1.85	9.18	7.99	−1.19	8.98	7.33	−1.65
9.89	7.76	−2.13	9.89	8.8	−1.09	10.28	9.86	−0.42
pH_{PZC}	**5.16**		**4.76**			**4.86**		

Table E.10. Summary of pH of point of zero charge (pH_{PCZ}) for leached slurry coke (SC) under acid rock drainage (ARD). Column solid samples were divided into four zones (1 to 4) from bottom to top.

SCE – Zone 1			**SCE – Zone 4**		
Initial pH	**Final pH**	**ΔpH**	**Initial pH**	**Final pH**	**ΔpH**
2.28	2.61	0.33	2.27	2.59	0.32
3.3	3.62	0.32	3.3	3.69	0.39
3.82	4.24	0.42	4.09	4.6	0.51
5.09	5.26	0.17	4.9	5.35	0.45
5.96	6.32	0.36	6.04	6.54	0.5
7.14	6.94	−0.2	7.08	7.13	0.05
8.11	7.12	−0.99	7.84	7.38	−0.46
9.01	7.6	−1.41	8.99	7.92	−1.07
9.74	8.14	−1.6	9.74	8.92	−0.82
pH_{PZC}	**6.72**		**7.15**		

Table E.11. Summary of pH of point of zero charge (pH_{PCZ}) for big column (sequential input solution, i.e., deionized water, oil sand process-affected water, and acid rock drainage). Column solid samples were divided into five zones (1 to 5) from bottom to top.

LC – Zone1			LC – Zone 5		
Initial pH	**Final pH**	**ΔpH**	**Initial pH**	**Final pH**	**ΔpH**
2.26	2.55	0.29	2.26	2.53	0.27
3.3	3.74	0.44	3.28	3.6	0.32
3.99	4.69	0.7	4.02	4.66	0.64
5.26	5.54	0.28	5.3	5.92	0.62
6.03	6.68	0.65	6.1	6.79	0.69
7.04	7.31	0.27	7.05	7.35	0.3
7.74	7.7	−0.04	7.74	7.76	0.02
8.96	8.77	−0.19	8.99	8.85	−0.14
9.75	9.55	−0.2	9.75	9.53	−0.22
pH_{PZC}	**7.65**		**7.9**		

[a]LC: Large column

Table E.12. Summary of pH of point of zero charge (pH_{PCZ}) for big column (sequential input solution, i.e., deionized water, oil sand process-affected water, and acid rock drainage). Column solid samples were divided into five zones (1 to 5) from bottom to top.

LC[a] – Zone3			LC – Zone3			LC – Zone3		
Initial pH	**Final pH**	**ΔpH**	**Initial pH**	**Final pH**	**ΔpH**	**Initial pH**	**Final pH**	**ΔpH**
2.26	2.56	0.3	2.3	2.35	0.05	2.24	2.3	0.06
3.28	3.64	0.36	3.27	3.38	0.11	3.25	3.39	0.14
4.03	4.77	0.74	4.09	4.36	0.27	4.04	4.33	0.29
5.28	5.89	0.61	5.04	5.12	0.08	4.76	4.95	0.19
6.06	6.75	0.69	6	6.08	0.08	6.02	6.02	0
7.06	7.36	0.3	6.85	6.69	−0.16	6.92	6.62	−0.3
7.74	7.7	−0.04	8.21	7.22	−0.99	8.08	7.11	−0.97
9.01	8.79	−0.22	8.93	7.66	−1.27	8.7	7.49	−1.21
9.78	9.6	−0.18	10.23	10.01	−0.22	10.26	10.01	−0.25
pH_{PZC}	**7.66**		**6.28**			**6.02**		

[a]LC: Large column

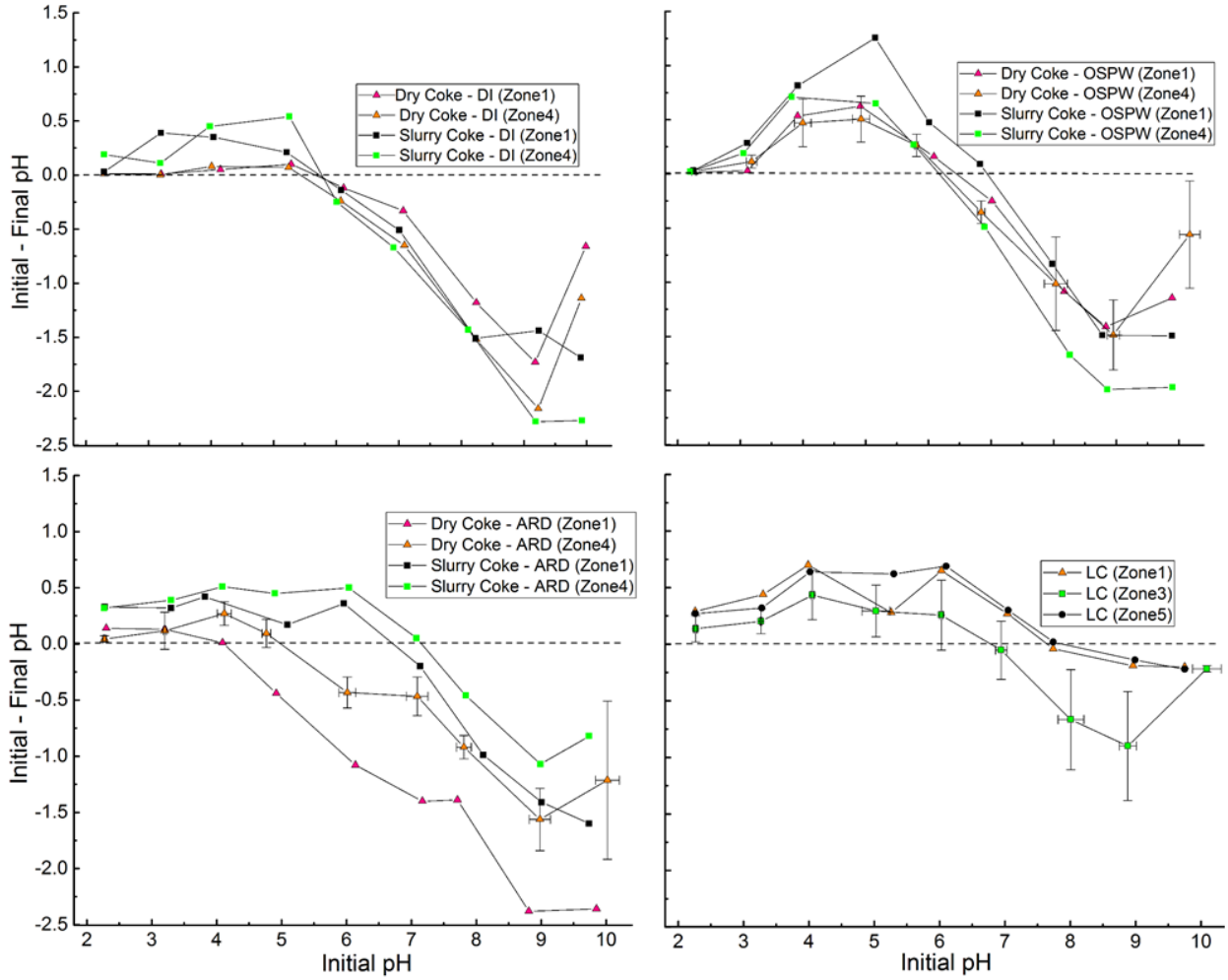

Figure E.2. The pH point of zero charge (pH_{PZC}) results for leached coke particle. Samples were obtained from zones 1 and 4 of the columns (Zone 1 is the area close to inflow, and zone 4 is close to the outflow).

Table E.13. The pH point of zero charge (pH_{PZC}) results for the small columns (leached samples).

Sample code	Zone 1	Zone 4
DC - DI[a]	5.66	5.43
SC - DI	5.73	5.77
DC - OSPW[b]	6.46	6.26 ±0.2
SC - OSPW	6.93	6.17
DC - ARD[c]	4.11	4.93 ± 0.17
SC - ARD	6.72	7.15

[a]DI: Deionized water
[b]OSPW: oil sand processing affected water
[c]ARD
DC: Dry coke
SC: Slurry coke

Table E.14. The pH point of zero charge (pH_{PZC}) results for the large column in different zones. Column solid samples were divided into five zones (1 to 5) from bottom to top.

	Zone 1	Zone 3	Zone 5
Large Column	7.65	6.65 ± 0.72	7.9

APPENDIX F: BULK ELEMENTAL ANALYSES

Table F.1. Bulk elemental analyses for the columns (LC: large column, SC: small columns). All values are in mg kg^{-1}.

Sample ID	C LECO	S LCEO	Si	Al	Fe	Ca	Zr	V	Ti	K
LC-10	788000	79800	14023	7463	5176	1930	2690	1360	1379	1079
LC-20	819000	79800	13556	7251	5036	1858	5380	1350	1379	996
LC-30	782000	79800	12620	7039	5386	1930	2030	1410	1438	1079
LC-40	778000	79900	13089	7039	5595	1930	2450	1430	1438	1162
LC-50	782400	80100	12154	6881	5316	1930	1580	1420	1379	1079
DC-A1	798000	78300	11686	6828	4966	1787	2590	1300	1319	996
DC-A3	778000	84700	14958	7198	5386	2430	1360	1350	1319	1079
SC-D1	793500	79800	13089	7251	5106	2073	3800	1380	1438	1079
SC-D2	801000	79200	11686	6933	4896	2001	1870	1350	1379	996
DC-B2	822000	80200	11686	6881	4966	1787	1380	1320	1319	996
DC-B3	791000	80600	13089	6986	5246	2073	1620	1420	1498	1079
SC-E1	784000	80200	13556	7198	5456	2359	2720	1460	1558	1079
SC-E2	812000	79900	12154	6881	5106	2073	1570	1400	1438	1079
DC-C1	780000	79000	11686	6881	4896	1858	1300	1320	1319	1079
DC-C2	785000	79400	11686	6828	5456	1787	1840	1320	1319	996
SC-F1	793000	80300	12621	6881	5176	2073	2570	1400	1438	1079
SC-F3	786000	80500	13556	7039	5316	2073	4300	1400	1498	1079

LC : Large column

DC: Dry coke

SC : Slurry coke

Continue Table **F.1.**

Sample ID	Mg	Na	Ni	P	Sr	Ba	Mo	Mn	Ce
LC-10	784.0	445.1	513.0	218.2	76.0	85.0	72.5	77.4	55.0
LC-20	723.7	445.1	552.0	261.9	78.0	76.0	73.2	77.4	43.0
LC-30	784.0	519.3	573.0	261.9	78.0	90.0	77.3	77.4	34.0
LC-40	784.0	445.1	549.0	305.5	82.0	75.0	78.0	77.4	35.0
LC-50	784.0	445.1	528.0	261.9	83.0	73.0	76.6	77.4	33.0
DC-A1	784.0	445.1	516.0	261.9	79.0	76.0	75.5	77.4	34.0
DC-A3	784.0	519.3	540.0	305.5	79.0	80.0	72.8	77.4	37.0
SC-D1	844.3	667.7	537.0	261.9	83.0	76.0	77.0	77.4	41.0
SC-D2	784.0	667.7	519.0	261.9	77.0	78.0	71.9	77.4	53.0
DC-B2	723.7	445.1	523.0	261.9	79.0	90.0	70.9	77.4	31.0
DC-B3	844.3	667.7	540.0	218.2	80.0	85.0	73.7	77.4	85.0
SC-E1	844.3	741.9	573.0	261.9	84.0	90.0	85.0	77.4	44.0
SC-E2	844.3	667.7	528.0	261.9	85.0	86.0	75.4	77.4	39.0
DC-C1	723.7	445.1	534.0	261.9	80.0	77.0	73.0	77.4	35.0
DC-C2	784.0	445.1	537.0	218.2	78.0	75.0	74.3	77.4	77.0
SC-F1	784.0	667.7	543.0	261.9	80.0	82.0	74.4	77.4	38.0
SC-F3	844.3	741.9	564.0	261.9	80.0	87.0	77.2	77.4	47.0

LC : Large column

DC: Dry coke

SC : Slurry coke

Continue Table **F.1.**

Sample ID	Cr	Zn	Y	Nd	La	Cu	Th	Be	Pb	Co
LC-10	43.0	31.0	15.2	13.7	17.0	10.2	7.9	7.1	8.4	5.2
LC-20	40.0	34.0	19.6	14.2	17.0	13.0	6.8	8.3	6.0	6.0
LC-30	50.0	41.0	15	13.6	16.0	13.8	5.7	8.6	6.4	6.6
LC-40	55.0	36.0	16	14.1	16.0	10.7	6.2	8.5	6.7	6.6
LC-50	55.0	30.0	13.5	14.5	16.0	10.3	5.8	8.1	5.8	6.5
DC-A1	41.0	40.0	14.7	13.4	15.0	33.0	5.5	8.3	4.4	5.1
DC-A3	58.0	38.0	14.1	13.8	16.0	12.6	7.0	7.6	4.5	6.1
SC-D1	46.0	39.0	17.2	14.5	17.0	15.9	7.0	7.7	7.3	5.5
SC-D2	43.0	34.0	14.3	15.1	15.0	12.9	6.8	7.7	4.2	5.6
DC-B2	43.0	33.0	12.8	12.4	14.0	16.6	5.3	8.2	6.0	5.9
DC-B3	42.0	45.0	15	37.8	36.0	10.1	89.4	7.8	10.3	6.6
SC-E1	38.0	64.0	16.6	15.0	19.0	12.5	8.7	7.3	5.4	5.5
SC-E2	44.0	37.0	13.7	16.0	19.0	14.0	5.8	7.8	6.0	5.4
DC-C1	39.0	33.0	12.9	14.2	17.0	16.6	5.6	7.7	11.4	5.4
DC-C2	42.0	56.0	15.9	16.7	22.0	14.3	5.2	7.2	5.6	6.2
SC-F1	64.0	33.0	16.1	15.2	18.0	102.0	7.5	8.0	6.8	5.4
SC-F3	55.0	57.0	20.3	17.4	21.0	43.8	13.6	8.6	7.0	5.0

LC : Large column

DC: Dry coke

SC : Slurry coke

Continue Table **F.1.**

Sample ID	Sn	U	Cd	As	Ag	Cs
LC-10	2.0	3.5	1.7	2.2	0.9	0.2
LC-20	1.1	3.8	3.7	2.5	0.4	0.2
LC-30	3.7	3.3	1.5	2.5	0.6	0.2
LC-40	1.4	2.8	1.8	1.9	1.0	0.2
LC-50	1.6	3.1	0.7	2.4	2.0	0.2
DC-A1	3.7	3.6	2.1	3.5	1.2	0.2
DC-A3	0.8	2.3	0.8	3.0	0.7	0.2
SC-D1	1.4	4.2	3.1	2.5	2.0	0.1
SC-D2	1.3	2.1	1.1	2.0	1.5	0.1
DC-B2	3.8	2.3	1.0	2.4	2.1	0.2
DC-B3	1.8	3.1	1.6	12.6	5.9	0.2
SC-E1	1.3	3.7	1.7	2.5	1.9	0.2
SC-E2	1.3	3.4	1.4	3.6	0.9	0.2
DC-C1	1.7	2.6	0.8	2.3	1.0	0.2
DC-C2	1.5	2.9	1.7	1.8	2.1	0.2
SC-F1	1.8	3.1	2.1	10.1	3.6	0.2
SC-F3	4.6	3.6	2.8	14.7	4.8	0.2

LC : Large column

DC: Dry coke

SC : Slurry coke

APPENDIX G: AQUEOUS GEOCHEMISTRY DATA FOR COLUMNS

Table G.1. Measurements of the large column influent.

PV[a]	pH	Eh	EC[b] (µS cm^{-1})	Alkalinity (mg L^{-1})
0.01	7.28	515.6	15.0	8.00
0.10	7.28	515.6	15.0	8.00
0.19	7.51	405.4	15.0	11.90
0.28	7.74	408.4	14.8	13.94
0.37	7.74	408.4	14.8	13.94
0.46	7.73	390.5	15.8	11.83
0.59	7.66	403.7	15.4	9.96
0.65	7.27	401.9	15.0	9.96
1.12	7.77	523.0	15.4	9.96
1.29	7.76	513.2	15.0	9.92
1.48	7.15	468.7	15.2	7.97
1.66	7.03	463.4	14.9	11.93
2.03	7.23	473.7	15.9	7.98
2.40	7.33	506.5	14.8	10.00
3.03	7.24	498.8	14.8	7.95
3.14	6.95	488.4	165.5	9.92
3.48	6.95	488.4	165.5	9.92
3.84	7.87	455.8	166.2	9.92
4.04	7.87	455.8	166.2	9.92
4.74	6.97	413.6	165.1	9.90
5.11	7.37	508.5	163.2	11.98
5.72	7.55	570.9	13.0	9.96
6.62	7.54	571.0	13.7	9.96
7.44	7.21	548.2	15.5	11.88
8.36	7.46	558.2	21.4	12.00
8.91	7.41	563.7	21.3	9.94
10.28	7.54	546.39	18.6	11.93
11.20	7.09	534.9	13.8	9.94
11.84	7.30	563.6	11.9	10.00
12.51	9.00	425.6	4840.0	694.00
12.78	9.09	415.9	4830.0	687.25
12.94	8.79	420.3	4830.0	718.56
13.24	8.78	429.4	4820.0	698.41

PV[a]	pH	Eh	EC[b] (µS cm^{-1})	Alkalinity (mg L^{-1})
13.31	8.85	379.65	4810.0	710.58
13.41	8.83	392.41	4800.0	715.71
13.69	8.70	440.40	4760.0	706.11
13.96	8.62	388.33	4770.0	688.98
14.50	8.69	421.99	4700.0	704.59
15.06	8.47	424.19	4700.0	718.00
15.87	8.47	424.19	4700.0	718.00
17.40	8.54	423.34	4840.0	714.29
18.23	8.64	426.40	4810.0	731.06
18.56	8.57	410.20	4810.0	718.56
19.11	8.70	451.88	4760.0	707.17
19.77	8.70	451.88	4760.0	717.13
20.13	8.69	424.90	4880.0	716.00
20.23	8.75	426.00	4830.0	716.00
20.48	8.67	407.87	4830.0	693.00
20.88	8.40	385.20	4880.0	714.30
21.87	8.40	385.20	4880.0	714.30
22.23	8.39	366.49	4830.0	715.71
22.88	8.39	366.49	4830.0	715.71
23.41	8.68	396.51	4680.0	714.29
23.94	8.81	461.90	4610.0	685.48
24.98	8.89	286.31	5170.0	938.12
25.79	8.90	286.31	5170.0	938.12
26.22	8.88	286.31	5170.0	938.12
26.39	8.89	286.31	5170.0	938.12
26.67	8.92	290.11	5080.0	924.15
26.76	8.99	332.70	4970.0	920.32
27.03	8.89	370.71	4900.0	910.89
27.65	8.91	394.15	4930.0	909.82
28.31	8.60	359.13	4900.0	914.51
28.96	8.82	447.63	4880.0	885.83
29.59	8.74	426.73	4810.0	878.73
30.20	7.23	521.37	165.5	7.95
30.84	7.23	521.37	165.5	7.95
31.46	7.23	521.37	165.5	7.95
31.95	7.75	491.19	168.5	11.95
32.10	7.23	522.09	13.7	7.95
32.47	7.15	520.80	12.1	8.00
32.76	7.23	522.09	13.7	7.95
33.38	7.23	522.09	13.7	7.95
33.61	7.09	524.80	11.2	8.22

PV[a]	pH	Eh	EC[b] (µS cm^{-1})	Alkalinity (mg L^{-1})
33.74	7.06	505.19	11.6	11.93
34.02	7.40	511.2	11.4	11.98
34.56	7.35	488.4	11.5	9.92
35.26	1.98	826.6	8770	–
35.89	2.10	828.6	8540	–
35.93	2.10	828.6	8540	–
36.02	2.10	828.6	8540	–
36.11	2.36	827.1	8700	–
36.20	2.35	826.8	8610	–
36.31	2.34	831.0	8670	–
36.39	2.20	829.8	8510	–
36.45	2.20	829.8	8510	–
36.54	2.42	827.7	8530	–
36.98	1.93	818.1	8940	–
37.19	1.97	830.9	9350	–
37.77	1.97	830.6	9350	–
38.03	2.07	825	8950	–
38.57	2.06	815.6	9060	–
38.85	2.04	826.6	8950	–
39.04	2.01	826.0	8940	–
39.10	2.01	826.0	8940	–
39.24	2.06	832.1	8790	–
39.30	2.06	832.6	8930	–
39.40	2.06	832.6	8930	–
39.57	2.06	830.4	9010	–
40.05	2.03	829.8	9030	–
40.39	2.03	829.8	9030	–
40.96	1.98	790.2	9880	–
41.67	1.92	788.6	9720	–
42.24	1.91	787.9	9700	–
42.47	1.98	812.5	9700	–
42.73	2.01	722.7	9580	–

[a]PV: Pore volume

[b]EC: Electrical conductivity

Table G.2. Major cations concentrations in the large column influent quantified with inductively coupled plasma–optical emission spectroscopy (ICP-OES).

PV[a]	Ca	Fe	K	Mg	Na	S
	mg L^{-1}	mg L^{-1}	mg L^{-1}	mg L^{-1}	mg L^{-1}	mg L^{-1}
0.10	0.03	ud[*]	0.07	ud	3.27	0.11
0.19	ud	ud	0.02	0.01	3.26	0.15
0.59	0.05	ud	0.02	0.02	3.24	0.19
0.65	0.05	ud	0.02	ud	3.22	0.11
1.29	0.04	ud	0.01	ud	3.18	0.12
2.40	0.05	ud	0.02	ud	3.20	0.11
3.03	0.09	ud	0.02	0.01	3.16	0.10
3.84	0.17	ud	0.04	0.01	29.64	0.11
5.11	0.12	ud	0.04	0.01	29.24	0.09
7.44	0.04	ud	0.02	ud	3.33	0.12
11.84	0.06	0.00	0.02	ud	2.59	0.20
12.51	2.57	ud	22.89	19.09	1100	75.5
12.78	2.30	ud	22.38	20.20	1130	84.2
12.94	8.05	ud	22.13	20.32	1130	83.6
13.24	5.86	ud	23.30	19.69	1140	77.4
13.31	5.85	ud	22.43	18.84	1120	73.4
13.41	5.60	ud	22.38	18.62	1150	73.1
13.69	4.51	ud	22.96	19.23	1150	75.6
13.96	6.10	ud	22.85	18.98	1120	74.0
19.77	3.46	ud	20.25	18.48	1050	71.8
23.94	3.70	ud	21.14	18.63	1110	74.03
26.22	5.72	ud	12.13	6.33	1140	191.3
27.65	6.10	ud	12.80	6.73	1170	204.0
29.59	6.06	ud	12.45	6.55	1155	197.0
36.11	394.0	2907	2.19	203.52	208	3680
37.19	400.8	2947	0.48	206.51	214	3820
38.03	422.2	2705	4.76	189.20	195	3349
39.24	395.9	2901	0.10	208.00	216	3687
39.57	386.3	2841	0.10	210.97	220	3649
40.39	427.6	2744	ud	195.80	196	3609
41.67	424.8	2796	ud	200.60	205	3758
42.24	412.3	2533	ud	199.01	202	3718

[a]PV: Pore volume

[*]ud: concentrations below method detection limit

Table G.3. Trace element concentrations in the large column influent quantified by inductively coupled plasma–optical mass spectroscopy (ICP-MS).

PV[a]	Al µg L^{-1}	Ba µg L^{-1}	Ca µg L^{-1}	Fe µg L^{-1}	K µg L^{-1}	Mg µg L^{-1}	Mo µg L^{-1}
0.008	ud*	ud	ud	ud	ud	ud	ud
0.098							
0.189	ud	ud	ud	ud	ud	34.86	ud
0.280							
0.370							
0.461							
0.586	ud	ud	ud	ud	ud	20.04	ud
0.654							
1.119							
1.293	ud	ud	ud	ud	ud	15.58	ud
1.478							
1.660							
2.032							
2.399							
3.028							
3.141							
3.478							
3.841	ud	ud	ud	ud	ud	ud	0.87
4.037							
4.741							
5.111							
5.722							
6.616							
7.444	ud	ud	ud	ud	ud	ud	ud
8.360							
8.914							
10.280							
11.205							
11.836	ud	ud	ud	ud	ud	13.75	1.45
12.509	ud	ud	2405.62	ud	19439.84	19579.28	ud
12.781							
12.944							
13.235	ud	ud	5723.39	ud	19974.97	20103.20	1.43
13.309	ud	ud	5537.93	ud	20550.58	20187.39	5.30
13.405	ud	ud	5327.62	ud	20222.52	20709.48	6.20
13.688	ud	ud	4214.13	ud	20374.04	20457.02	9.09
13.957	ud	ud	5970.17	ud	20491.69	20674.02	4.67
14.498							

PV[a]	Al µg L^{-1}	Ba µg L^{-1}	Ca µg L^{-1}	Fe µg L^{-1}	K µg L^{-1}	Mg µg L^{-1}	Mo µg L^{-1}
15.055							
15.867	ud	ud	10199.32	85.00	18658.24	22751.89	ud
17.399							
18.229							
18.558							
19.112							
19.766	ud	ud	3214.70	ud	20327.02	20873.20	3.30
20.128							
20.227							
20.483							
20.879							
21.873							
22.234							
22.884							
23.412							
23.937	5.10	ud	3869.03	30.60	21092.14	21647.54	1.13
24.981							
25.786							
26.217	ud	194.28	6079.58	ud	12935.66	7750.27	130.13
26.391							
26.674							
26.757							
27.026							
27.649	ud	184.17	6022.83	ud	11243.30	6521.16	135.42
28.313							
28.957							
29.589	ud	198.98	5961.82	ud	11388.54	6598.75	132.56
30.199							
30.838							
31.464							
31.950							
32.097							
32.469							
32.764							
33.381							
33.608							
33.740							
34.016							
34.564							
35.263							
35.887							

PV[a]	Al µg L^{-1}	Ba µg L^{-1}	Ca µg L^{-1}	Fe µg L^{-1}	K µg L^{-1}	Mg µg L^{-1}	Mo µg L^{-1}
35.932							
36.017							
36.114							
36.203							
36.308							
36.386							
36.450							
36.541							
36.979							
37.187	ud	ud	411586.72	2871972.50	448.23	152469.93	13.89
37.770							
38.030							
38.575							
38.854							
39.036							
39.100							
39.238							
39.297							
39.405							
39.575	17.76	7.91	396506.64	2708032.28	198.84	154211.38	13.00
40.055							
40.391	9.43	4.21	421093.72	2815343.49	ud	219364.14	5.95
40.960							
41.669							
42.244	ud	3.49	421899.76	2639015.81	ud	226615.52	5.06
42.470							
42.731							

[a]PV: Pore volume

*ud: concentrations below method detection limit

Continue **Table G.3**

PV[a]	Ni µg L^{-1}	Sr µg L^{-1}	V µg L^{-1}
0.008	ud*	ud	ud
0.098			
0.189	ud	0.7877	ud
0.280			
0.370			
0.461			
0.586	ud	0.5158	ud
0.654			
1.119			
1.293	ud	0.3160	ud
1.478			
1.660			
2.032			
2.399			
3.028			
3.141			
3.478			
3.841	ud	ud	ud
4.037			
4.741			
5.111			
5.722			
6.616			
7.444	ud	ud	ud
8.360			
8.914			
10.280			
11.205			
11.836	ud	ud	ud
12.509	ud	1.2470	ud
12.781			
12.944			
13.235	ud	2.2478	ud
13.309	ud	2.2287	ud
13.405	ud	2.3208	ud
13.688	ud	2.2134	2.1848
13.957	ud	2.5894	ud
14.498			
15.055			

PV[a]	Ni µg L^{-1}	Sr µg L^{-1}	V µg L^{-1}
15.867	ud	2.7712	ud
17.399			
18.229			
18.558			
19.112			
19.766	ud	1.4671	ud
20.128			
20.227			
20.483			
20.879			
21.873			
22.234			
22.884			
23.412			
23.937	ud	3.8174	ud
24.981			
25.786			
26.217	6.5430	400.1590	3.5087
26.391			
26.674			
26.757			
27.026			
27.649	6.1168	377.8602	3.1128
28.313			
28.957			
29.589	14.8575	378.1048	2.0988
30.199			
30.838			
31.464			
31.950			
32.097			
32.469			
32.764			
33.381			
33.608			
33.740			
34.016			
34.564			
35.263			
35.887			
35.932			

PV[a]	Ni µg L^{-1}	Sr µg L^{-1}	V µg L^{-1}
36.017			
36.114			
36.203			
36.308			
36.386			
36.450			
36.541			
36.979			
37.187	12.6531	108.1936	5.2454
37.770			
38.030			
38.575			
38.854			
39.036			
39.100			
39.238			
39.297			
39.405			
39.575	13.3172	105.0670	2.2428
40.055			
40.391	30.9286	84.7556	ud
40.960			
41.669			
42.244	31.6309	88.6235	ud
42.470			
42.731			

[a]PV: Pore volume

*ud: concentrations below method detection limit

Table G.4. Measurements performed on the large column effluent.

PV[a]	pH	Eh	EC[b] (µS cm^{-1})	Alkalinity (mg L^{-1})
0.01	5.22	500.89	1227.00	84.00
0.10	5.25	479.02	1348.00	83.67
0.19	5.23	442.11	1225.00	83.50
0.28	5.33	435.94	1083.00	87.13
0.37	5.37	418.12	1120.00	91.09
0.46	5.25	417.41	926.00	85.49
0.59	5.34	419.85	718.00	81.35
0.65	5.35	419.15	757.00	85.83
1.12	5.15	469.29	296.90	69.72
1.29	5.53	512.02	235.40	63.87
1.48	5.07	445.32	228.00	63.49
1.66	5.15	424.22	218.60	57.88
2.03	5.10	440.19	158.80	61.51
2.40	4.95	470.23	124.10	47.62
3.03	4.94	480.01	96.50	37.85
3.14	4.89	483.38	93.10	39.76
3.48	4.85	474.63	87.80	33.80
3.84	4.91	486.47	80.00	32.00
4.04	4.95	517.04	107.90	30.00
4.74	4.94	453.30	211.40	33.86
5.11	4.86	491.81	212.10	27.83
5.72	4.97	539.09	209.00	28.00
6.62	4.84	539.00	115.00	26.00
7.44	4.66	554.83	58.00	25.84
8.36	4.67	597.94	57.60	31.75
8.91	4.73	573.64	56.80	23.76
10.28	4.75	577.86	55.70	21.78
11.20	4.62	566.42	52.90	21.87
11.84	4.64	602.83	48.50	15.87
12.51	4.71	594.49	46.60	27.72
12.78	4.85	623.19	45.90	25.84
12.94	4.55	616.92	46.20	23.90
13.24	5.88	533.14	4000.00	485.15
13.31	6.10	447.81	4480.00	640.72
13.41	6.15	534.82	4650.00	641.43
13.69	6.10	485.36	4720.00	683.17
13.96	6.12	494.03	4720.00	657.37

PV[a]	pH	Eh	EC[b] (µS cm^{-1})	Alkalinity (mg L^{-1})
14.50	6.16	468.38	4690.00	695.83
15.06	6.13	431.65	4670.00	693.84
15.87	6.20	418.43	4880.00	684.63
17.40	6.18	441.83	4840.00	710.32
18.23	6.34	514.96	4740.00	703.19
18.56	6.31	493.49	4760.00	709.16
19.11	6.35	484.76	4740.00	699.60
19.77	6.36	479.85	4890.00	695.83
20.13	6.50	461.56	4760.00	709.16
20.23	6.43	506.89	4820.00	706.00
20.48	6.45	417.72	4830.00	697.21
20.88	6.46	374.76	4810.00	660.00
21.87	6.45	418.79	4840.00	618.76
22.23	6.37	397.55	4810.00	695.83
22.88	6.65	441.53	4750.00	632.41
23.41	6.69	412.91	4670.00	738.52
23.94	6.80	489.88	4610.00	657.64
24.98	6.75	520.22	4230.00	758.48
25.79	6.72	519.11	4280.00	860.00
26.22	6.60	328.04	5060.00	934.39
26.39	6.96	343.00	5040.00	909.68
26.67	6.95	325.73	5010.00	914.51
26.76	6.86	457.34	4980.00	912.35
27.03	7.07	425.19	5010.00	894.21
27.65	7.08	490.25	4910.00	914.51
28.31	6.74	429.13	4900.00	906.93
28.96	6.72	484.11	4850.00	892.86
29.59	6.81	508.03	4820.00	876.49
30.20	6.72	499.02	4790.00	892.00
30.84	6.61	496.90	2765.00	701.79
31.46	6.35	386.29	965.00	180.87
31.95	6.00	474.25	534.00	101.39
32.10	6.01	452.24	460.00	79.37
32.47	6.15	460.32	380.00	64.53
32.76	6.49	472.39	308.00	51.69
33.38	5.61	458.26	103.60	41.75
33.61	5.54	460.54	86.00	35.76
33.74	5.48	466.83	68.00	27.78
34.02	5.61	470.56	54.20	27.83

PV[a]	pH	Eh	EC[b] (µS cm^{-1})	Alkalinity (mg L^{-1})
34.56	5.46	472.29	41.40	19.96
35.26	5.41	537.38	33.90	24.00
35.89	2.69	640.62	6370.00	–
35.93	2.65	669.59	7260.00	–
36.02	2.56	682.60	7850.00	–
36.11	2.54	688.14	8020.00	–
36.20	2.50	688.38	8050.00	–
36.31	2.47	692.11	8210.00	–
36.39	2.39	694.35	8040.00	–
36.45	2.44	701.34	8020.00	–
36.54	2.53	696.69	8120.00	–
36.98	2.05	701.42	8380.00	–
37.19	2.10	704.98	8750.00	–
37.77	2.13	705.53	8850.00	–
38.03	2.10	702.34	8920.00	–
38.57	2.14	703.64	9110.00	–
38.85	2.12	701.84	9080.00	–
39.04	2.10	705.74	9050.00	–
39.10	2.10	715.33	8760.00	–
39.24	2.10	712.08	8870.00	–
39.30	2.12	711.30	9040.00	–
39.40	2.09	713.01	9000.00	–
39.57	2.07	711.74	9050.00	–
40.05	2.08	710.85	8960.00	–
40.39	2.10	715.66	8670.00	–
40.96	2.13	715.68	8880.00	–
41.67	1.90	718.39	9250.00	–
42.24	1.99	715.72	9370.00	–
42.47	1.98	719.74	9610.00	–
42.73	2.01	722.65	9580.00	–

[a]PV: Pore volume

[b]EC: Electrical conductivity

Table G.5. Major cations concentrations in the large column effluent quantified with inductively coupled plasma–optical emission spectroscopy (ICP-OES).

PV[a]	Ca mg L^{-1}	Fe mg L^{-1}	K mg L^{-1}	Mg mg L^{-1}	Na mg L^{-1}	S mg L^{-1}
0.01	151.4	3.0	13.4	44.9	30.0	182.5
0.10	178.4	4.1	15.1	57.7	33.3	239.1
0.19	160.9	4.0	11.7	56.7	31.0	228.8
0.28						
0.37	133.9	3.8	8.8	47.0	24.3	183.1
0.46						
0.59	79.8	5.2	5.2	27.6	14.7	99.9
0.65	87.4	4.3	5.7	25.4	15.2	93.6
1.12						
1.29	18.5	15.3	1.1	5.4	4.8	15.8
1.48						
1.66						
2.03	9.1	17.3	0.5	2.5	3.7	5.6
2.40	6.0	16.8	0.4	1.4	3.5	2.6
3.03	4.2	12.5	0.3	0.9	3.4	2.0
3.14	4.1	11.9	0.3	1.0	3.6	2.1
3.48	3.5	10.3	0.3	0.9	3.6	2.0
3.84	3.1	9.4	0.3	0.8	3.3	1.6
4.04	2.8	8.8	0.3	0.8	9.7	1.7
4.74	2.3	7.7	0.3	0.7	29.2	1.5
5.11	2.1	7.6	0.3	0.6	29.3	1.3
5.72	1.8	0.0	0.3	0.0	30.4	0.1
6.62						
7.44	1.3	4.9	0.2	0.4	3.2	0.9
8.36	1.1	0.0	0.2	0.0	3.5	0.1
8.91						
10.28						
11.20						
11.84	0.7	2.7	0.1	0.2	3.6	1.0
12.51	0.6	2.6	0.1	0.2	3.5	1.0
12.78	0.6	2.5	ud	0.3	2.1	3.0
12.94	0.6	2.4	ud	0.3	2.1	3.2
13.24	0.5	0.2	12.6	5.7	939.1	73.4
13.31	0.7	0.2	17.1	13.0	1044.0	75.3
13.41	1.4	0.1	20.0	16.3	1104.2	75.0
13.69	2.6	0.1	23.0	18.3	1130.7	77.5
13.96	2.8	0.1	21.7	18.4	1115.0	73.2
14.50						
15.06						

PV[a]	Ca mg L^{-1}	Fe mg L^{-1}	K mg L^{-1}	Mg mg L^{-1}	Na mg L^{-1}	S mg L^{-1}
15.87	5.3	0.8	21.9	20.2	1111.4	84.4
17.40	8.6	0.4	22.2	20.6	1116.2	85.0
18.23						
18.56	6.1	0.4	22.1	19.9	1109.9	85.9
19.11						
19.77	6.4	0.2	21.4	18.4	1027.0	75.7
20.13						
20.23						
20.48						
20.88						
21.87	5.5	0.4	21.1	19.3	1052.2	74.9
22.23						
22.88						
23.41						
23.94	5.5	0.1	20.9	18.2	1052.0	74.6
24.98	4.3	0.2	20.4	17.9	1072.6	94.1
25.79						
26.22	5.8	0.2	13.2	6.8	1168.3	205.1
26.39	5.8	0.3	13.2	6.9	1195.2	206.1
26.67	5.9	0.3	12.9	6.7	1179.2	204.8
26.76						
27.03						
27.65	5.9	0.2	12.9	6.7	1207.0	202.4
28.31						
28.96						
29.59	6.1	0.1	12.6	6.7	1200.4	203.2
30.20						
30.84						
31.46						
31.95						
32.10						
32.47	3.8	ud[*]	ud	0.7	61.5	8.7
32.76						
33.38						
33.61	2.7	ud	ud	0.6	9.8	3.9
33.74						
34.02						
34.56						
35.26						
35.89	331.4	2141.0	5.2	154.1	143.8	2610.0
35.93	387.9	2592.4	5.5	193.0	188.5	3236.5

PV[a]	Ca mg L^{-1}	Fe mg L^{-1}	K mg L^{-1}	Mg mg L^{-1}	Na mg L^{-1}	S mg L^{-1}
36.02	408.1	2944.2	4.2	206.1	206.7	3647.0
36.11	415.1	2973.2	2.2	210.0	215.6	3607.9
36.20	415.4	2831.6	ud	194.5	199.0	3372.7
36.31						
36.39	418.7	2787.9	ud	193.4	197.1	3396.9
36.45	421.6	2772.8	ud	192.4	196.6	3386.6
36.54	406.7	2906.8	0.2	204.6	207.4	3665.2
36.98	423.8	2754.1	ud	191.3	194.5	3385.2
37.19	400.2	2874.2	0.0	208.6	214.7	3665.4
37.77						
38.03	428.0	2777.9	ud	193.3	191.7	3473.1
38.57	430.6	2786.9	ud	194.8	193.3	3571.6
38.85	400.6	2856.7	ud	209.5	215.7	3703.5
39.04						
39.10						
39.24	391.2	2792.3	ud	206.3	209.8	3591.1
39.30						
39.40						
39.57	391.0	2838.9	ud	204.6	212.7	3567.3
40.05						
40.39	417.0	2723.8	ud	195.4	197.9	3568.7
40.96						
41.67	409.3	2692.1	ud	202.1	204.8	3738.7
42.24	407.8	2458.8	ud	202.9	208.5	3759.2
42.47						
42.73	414.7	2625.6	ud	207.3	219.3	3489.1

[a]PV: Pore volume

*ud: concentrations below method detection limit

Table G.6. Trace elements concentrations in the large column effluent quantified with inductively coupled plasma–optical mass spectroscopy (ICP-MS).

PV[a]	Al µg L^{-1}	Ca µg L^{-1}	Fe µg L^{-1}	K µg L^{-1}	Mg µg L^{-1}	Mo µg L^{-1}
0.01	105.48	147174.26	3370.9	11090.4	54234.3	1.48
0.10	128.61	175767.97	4329.6	12275.2	64847.1	0.93
0.19	110.72	157206.82	4327.5	10696.4	57978.2	1.42
0.28	99.53	139058.44	3935.7	9409.1	51054.1	1.33
0.37	106.81	139343.60	4226.1	8907.9	51086.6	1.75
0.46						
0.59	104.76	82753.74	5596.5	5081.8	30322.3	1.34
0.65						
1.12						
1.29	108.43	18247.19	17100.3	1007.0	6367.7	ud
1.48						
1.66						
2.03						
2.40	149.46	6039.99	18089.4	381.7	1608.0	ud
3.03						
3.14						
3.48						
3.84	328.72	3030.63	10459.2	260.3	911.0	ud
4.04						
4.74						
5.11						
5.72						
6.62						
7.44	936.88	1379.98	5217.4	160.8	475.8	ud
8.36						
8.91						
10.28						
11.20						
11.84	657.72	363.27	2600.4	134.2	254.9	0.93
12.51	632.51	378.25	2765.6	184.1	297.1	3.50
12.78	797.90	778.87	2784.3	134.5	282.3	ud
12.94	800.76	765.27	2666.6	131.4	269.4	ud
13.24	ud	ud	184.9	11592.4	6057.3	556.90
13.31	ud	383.90	87.0	16006.5	14918.1	574.42
13.41	ud	1200.01	96.2	18350.0	17952.0	396.36
13.69	ud	2492.35	102.8	19901.5	19595.3	171.25
13.96	ud	2565.00	149.9	20224.2	20309.7	113.47
14.50						

PV[a]	Al µg L^{-1}	Ca µg L^{-1}	Fe µg L^{-1}	K µg L^{-1}	Mg µg L^{-1}	Mo µg L^{-1}
15.06						
15.87	ud	6104.22	939.0	18027.2	22537.0	43.68
17.40						
18.23						
18.56	ud	6980.80	469.6	18107.0	22490.6	23.65
19.11						
19.77	ud	6448.92	174.4	20747.7	20987.7	21.10
20.13						
20.23						
20.48						
20.88						
21.87	ud	5494.52	469.1	21039.5	22499.2	16.85
22.23						
22.88						
23.41						
23.94	ud	6594.25	213.4	21258.3	21687.4	13.62
24.98	ud	4029.14	175.1	20528.1	20641.2	18.51
25.79						
26.22	81.23	5604.07	276.3	11735.4	6809.2	146.96
26.39	87.59	5840.90	250.7	11666.6	6750.8	152.46
26.67	84.66	5675.93	322.0	11814.0	6725.4	152.86
26.76						
27.03						
27.65	71.04	6070.23	279.1	11380.1	6822.2	145.49
28.31						
28.96						
29.59	33.35	5728.02	115.5	11536.9	6555.9	144.10
30.20						
30.84	49.73	3916.55	387.2	6824.7	4045.6	57.54
31.46						
31.95						
32.10						
32.47	ud	4149.70	18.8	612.2	868.1	3.80
32.76	ud	3780.51	15.3	603.7	817.5	3.12
33.38						
33.61	ud	2734.47	ud	216.7	532.8	ud
33.74						
34.02						
34.56						
35.26						
35.89	111282.08	333392.51	2125587.9	5333.4	138717.8	106.67

PV[a]	Al µg L^{-1}	Ca µg L^{-1}	Fe µg L^{-1}	K µg L^{-1}	Mg µg L^{-1}	Mo µg L^{-1}
35.93	71515.93	392416.69	2707871.4	5157.1	138962.9	160.09
36.02	75417.75	428966.75	2859191.4	4254.7	202112.5	143.11
36.11	62237.46	423177.15	2886653.3	2378.6	197812.1	124.63
36.20	56351.75	426371.24	2852285.9	1266.9	199436.9	115.44
36.31						
36.39	38273.18	398328.78	2718276.3	288.7	171206.6	101.20
36.45	36286.92	403037.35	2708776.9	632.7	172241.0	100.95
36.54	38799.62	422835.87	2783567.0	180.7	191085.7	97.26
36.98						
37.19	16302.63	395565.97	2759230.0	ud	150297.4	79.26
37.77						
38.03	25417.61	420454.12	2802226.7	191.7	199533.1	89.94
38.57	27030.73	422366.82	2825316.2	27.3	193079.0	80.22
38.85	11646.03	401771.43	2679858.0	ud	151540.7	81.08
39.04						
39.10	11118.13	426658.89	2637178.5	58.4	193040.4	75.26
39.24	7174.76	402611.05	2670206.7	ud	150791.8	69.62
39.30						
39.40						
39.57	7961.73	390860.54	2643944.3	ud	144261.2	70.45
40.05						
40.39	4884.27	418657.70	2775081.3	ud	220425.6	45.12
40.96						
41.67	4229.25	420990.11	2786574.2	ud	222400.9	42.91
42.24	4394.72	427813.46	2653989.7	ud	228359.3	35.48
42.47						
42.73	2604.51	369524.60	3046525.7	ud	153530.6	49.61

[a]PV: Pore volume

*ud: concentrations below method detection limit

Continue **Table G.6**

PV[a]	Ni µg L^{-1}	Sr µg L^{-1}	V µg L^{-1}
0.01	1582.34	1443.60	4.21
0.10	1876.33	1854.50	ud*
0.19	1697.23	1596.33	ud
0.28	1485.12	1372.81	ud
0.37	1463.03	1392.03	ud
0.46			

PV[a]	Ni µg L^{-1}	Sr µg L^{-1}	V µg L^{-1}
0.59	866.00	853.18	ud
0.65			
1.12			
1.29	205.88	236.83	ud
1.48			
1.66			
2.03			
2.40	58.48	64.28	ud
3.03			
3.14			
3.48			
3.84	27.30	29.71	ud
4.04			
4.74			
5.11			
5.72			
6.62			
7.44	16.71	16.36	2.24
8.36			
8.91			
10.28			
11.20			
11.84	7.76	9.94	4.69
12.51	9.67	10.20	7.40
12.78	8.50	10.12	7.35
12.94	9.34	10.08	7.62
13.24	ud	13.04	61.02
13.31	ud	16.61	68.91
13.41	ud	22.95	86.19
13.69	ud	22.54	97.91
13.96	ud	16.38	97.70
14.50			
15.06			
15.87	ud	9.84	16.87
17.40			
18.23			
18.56	ud	7.86	8.90
19.11			
19.77	ud	7.44	6.08
20.13			
20.23			

PV[a]	Ni µg L^{-1}	Sr µg L^{-1}	V µg L^{-1}
20.48			
20.88			
21.87	ud	6.72	6.11
22.23			
22.88			
23.41			
23.94	ud	8.14	5.38
24.98	ud	4.69	5.90
25.79			
26.22	5.29	272.34	21.66
26.39	ud	300.67	19.33
26.67	5.09	321.13	20.44
26.76			
27.03			
27.65	4.76	351.65	20.47
28.31			
28.96			
29.59	5.58	362.78	31.72
30.20			
30.84	ud	228.55	20.46
31.46			
31.95			
32.10			
32.47	ud	123.38	ud
32.76	ud	123.56	ud
33.38			
33.61	ud	51.96	ud
33.74			
34.02			
34.56			
35.26			
35.89	2303.04	793.10	6904.08
35.93	2070.21	782.08	4618.69
36.02	1581.94	645.33	3477.44
36.11	1319.45	572.96	2997.98
36.20	1175.69	535.82	2796.60
36.31			
36.39	882.69	481.01	2341.73
36.45	822.43	461.52	2259.74
36.54	766.79	399.60	2265.99
36.98			

PV[a]	Ni µg L^{-1}	Sr µg L^{-1}	V µg L^{-1}
37.19	462.87	259.56	1555.83
37.77			
38.03	664.99	213.00	2073.32
38.57	750.64	236.13	1840.40
38.85	576.51	171.88	1158.85
39.04			
39.10	374.86	137.91	884.78
39.24	249.93	123.37	750.91
39.30			
39.40			
39.57	145.20	137.06	945.96
40.05			
40.39	62.40	75.49	379.19
40.96			
41.67	83.74	105.05	475.23
42.24	85.70	106.27	367.66
42.47			
42.73	78.09	104.60	414.89

[a]PV: Pore volume

*ud: concentrations below method detection limit

Table G.7. Measurements of the column influent for columns under deionized water (DI) water input.

PV[a]	pH	Eh	EC[b] (µS cm^{-1})	Alkalinity (mg L^{-1})
0.15	7.39	519.91	16.75	11.88
0.54	7.21	512.30	16.31	9.98
1.27	7.21	564.80	16.37	9.96
1.93	7.32	547.38	20	11.90
2.74	7.22	554.20	19.87	12.00
3.45	7.33	548.84	18.69	9.96
4.64	7.37	552.76	16.05	11.93
4.91	7.3	551.99	16.37	11.90
5.61	7.34	558.94	15.92	11.95
6.29	7.3	536.69	15.92	11.90
6.54	7.54	531.76	15.96	11.95
6.93	7.28	557.23	15.89	11.88
8.00	7.02	560.02	11.19	11.90
8.63	7.32	559.60	11.53	11.95
10.01	7.13	554.99	11.09	11.95
10.55	7.32	577.38	10.54	12.00
11.62	7.2	561.73	10.48	11.90
12.60	7.03	554.42	10.48	9.94
13.53	7.03	501.02	10.78	9.92
14.60	7.17	508.85	10.46	11.86
15.57	7.09	541.53	10.62	11.98
16.81	7.05	545.65	10.24	9.94
17.30	7.08	520.90	10.52	11.98
18.13	7.03	552.76	10.42	9.96
19.21	7.28	527.21	10.7	9.90
20.05	7.18	579.10	10.05	10.00
20.99	7.22	496.38	9.96	11.88
21.97	7.16	519.20	10.27	10.00
23.04	7.04	500.20	10.63	11.98
24.02	7.06	516.22	10.47	9.92
24.56	7.29	539.78	10.28	15.97
25.59	7.58	582.20	10.33	10.14
27.16	7.2	542.20	10.33	11.93
28.20	7.06	336.55	10.57	7.97
28.63	7.06	336.55	10.57	7.97
29.16	7.61	491.63	12.99	10.00
30.11	7.13	540.38	11.27	11.90

[a]PV: Pore volume [b]EC: Electrical conductivity

Table G.8. Major cation concentrations quantified with inductively coupled plasma–optical emission spectroscopy (ICP-OES) in the influent columns during deionized water (DI) input.

PV[a]	Ca	Fe	K	Mg	Na	S
	mg L^{-1}	mg L^{-1}	mg L^{-1}	mg L^{-1}	mg L^{-1}	mg L^{-1}
0.15	0.1076	0.0008	ud*	ud	3.6425	0.1406
0.54						
1.27						
1.93						
2.74						
3.45	ud	ud	ud	ud	4.1461	0.2306
4.64	0.3086	ud	ud	0.0222	3.452	0.1797
4.91						
5.61						
6.29						
6.54						
6.93						
8.00						
8.63	ud	ud	ud	0.0526	2.3465	ud
10.01						
10.55						
11.62						
12.60						
13.53						
14.60						
15.57						
16.81	ud	ud	ud	0.024	2.0431	ud
17.30						
18.13						
19.21						
20.05						
20.99						
21.97						
23.04						
24.02						
24.56	0.1801	1.7124	ud	0.0413	2.1644	0.9162
25.59						
27.16						
28.20						
28.63						
29.16						
30.11						

[a]PV: Pore volume *ud: concentrations below method detection limit

Table G.9. Trace element concentrations quantified with inductively coupled plasma–optical mass spectroscopy (ICP-MS) in the influent columns under deionized water (DI) input.

PV[a]	Al µg L^{-1}	Ca µg L^{-1}	Fe µg L^{-1}	K µg L^{-1}	Mg µg L^{-1}	Mo µg L^{-1}	Ni µg L^{-1}	Sr µg L^{-1}	V µg L^{-1}
0.15	ud*	236.2997	ud	ud	18.87074	ud	ud	ud	ud
0.54									
1.27									
1.93									
2.74									
3.45	ud	ud	ud	268.0786	ud	ud	ud	ud	ud
4.64	ud	ud	ud	ud	17.0132	10.3759	ud	1.137551	10.93637
4.91									
5.61									
6.29									
6.54									
6.93									
8.00									
8.63	ud	ud	ud	309.2808	ud	ud	ud	ud	ud
10.01									
10.55	ud	ud	ud	ud	ud	1.2397	ud	ud	ud
11.62									
12.60									
13.53									
14.60									
15.57									
16.81	ud	ud	87.98654	ud	ud	ud	ud	0.358052	ud
17.30									
18.13									
19.21									
20.05									
20.99									
21.97									
23.04									
24.02									
24.56	ud	250.2149	ud	ud	22.2224	ud	ud	ud	ud
25.59									
27.16									
28.20									
28.63									
29.16									
30.11									

[a]PV: Pore volume *ud: concentrations below method detection limit

Table G.10. Measurements of the column effluent for dry coke under deionized water (DI) water input.

PV[a]	pH	Eh	EC[b] (µS cm^{-1})	Alkalinity (mg L^{-1})
0.20	5.41	471.38	1350.00	91.80
0.76	5.33	484.45	1103.00	83.17
1.37	5.40	543.48	734.00	63.62
2.25	5.29	543.85	351.00	57.65
3.13	5.10	646.31	206.90	37.85
3.97	4.98	655.72	148.10	32.00
5.15	4.87	683.40	94.90	25.95
5.59	5.06	663.59	75.50	25.95
6.34	4.84	687.31	53.20	23.81
6.76	4.95	664.58	50.20	15.84
8.11	4.93	684.54	46.90	19.80
8.38	4.85	686.93	42.20	28.00
8.92	4.78	674.00	41.80	23.86
9.60	4.83	666.18	41.60	19.96
11.09	4.88	593.48	41.00	25.90
11.67	4.98	631.14	43.00	23.76
12.82	4.92	538.00	47.00	23.86
13.88	4.83	527.00	44.50	20.00
14.89	4.85	503.82	43.40	23.90
16.04	4.94	511.51	39.70	19.80
17.08	4.69	537.54	38.10	17.89
17.98	4.73	541.50	36.70	19.88
18.96	4.64	641.70	39.40	11.95
19.85	4.48	666.14	34.20	9.96
21.01	4.65	660.88	30.50	8.00
21.92	4.65	642.25	29.28	11.98
22.93	4.76	584.84	27.74	7.95
23.99	4.61	600.68	27.53	7.98
25.15	4.73	578.28	26.90	11.93
26.20	4.79	621.69	26.39	13.86
26.79	4.99	571.88	26.21	11.93
27.90	4.91	656.37	29.63	11.93
29.59	5.23	677.82	21.86	13.97
30.72	4.89	446.10	28.55	15.94
31.18	4.95	440.72	28.90	7.92
31.75	5.08	579.00	26.89	11.93
32.77	5.01	593.68	25.08	11.90

[a]PV: Pore volume [b]EC: Electrical conductivity

Table G.11. Major cation concentrations quantified with inductively coupled plasma–optical emission spectroscopy (ICP-OES) in the effluent from the column with dry coke during deionized water (DI) input

PV[a]	Ca mg L^{-1}	Fe mg L^{-1}	K mg L^{-1}	Mg mg L^{-1}	Na mg L^{-1}	S mg L^{-1}
0.20	153.098	1.1411	9.6767	44.1964	28.1859	205.017
0.76	140.019	0.5048	7.9509	41.4668	23.9898	186.269
1.37	85.8402	0.3654	4.7538	25.7821	15.02	113.067
2.25	36.4146	0.2561	1.9085	10.5747	7.6783	44.4198
3.13	17.0934	ud*	0.8759	4.4216	6.4193	17.5751
3.97	9.3372	ud	0.4641	2.2264	4.6375	8.9647
5.15	3.3758	ud	0.1974	0.6916	4.4756	3.6988
5.59						
6.34						
6.76	2.6308	ud	0.1303	0.4088	3.5496	2.5744
8.11						
8.38	1.6797	ud	0.1006	0.3155	3.4499	2.1819
8.92						
9.60	1.3988	ud	0.0918	0.2804	3.4733	1.9751
11.09						
11.67						
12.82						
13.88						
14.89						
16.04						
17.08						
17.98	0.6661	2.6919	0.0648	0.1544	2.145	1.1382
18.96						
19.85						
21.01						
21.92						
22.93						
23.99						
25.15						
26.20						
26.79	0.4741	1	0.0589	0.0861	2.0357	0.9352
27.90						
29.59						
30.72						
31.18						
31.75						
32.77						

PV[a]	Ca mg L^{-1}	Fe mg L^{-1}	K mg L^{-1}	Mg mg L^{-1}	Na mg L^{-1}	S mg L^{-1}

[a]PV: Pore volume

[*]ud: concentrations below method detection limit

Table G.12. Measured trace element concentrations by inductively coupled plasma–optical mass spectroscopy (ICP-MS) in the column effluent of dry coke during deionized water (DI) input.

PV[a]	Al µg L^{-1}	Ba µg L^{-1}	Ca µg L^{-1}	Fe µg L^{-1}	K µg L^{-1}	Mg µg L^{-1}	Mo µg L^{-1}
0.20	1054.275	91.74679	154137.1	705.559	10028.72	45653.01	5.840619
0.76	667.2488	71.08876	143165.7	228.201	7273.45	40742.02	1.709189
1.37	417.2087	79.95081	90139.74	105.5381	4692.112	27106.05	1.343012
2.25	280.5544	136.1495	38451.79	83.23877	2482.725	11191.9	0.42341
3.13	341.7888	147.2257	18057.61	ud*	943.5826	4720.394	0.088688
3.97	378.2515	95.36391	9861.231	ud	835.8972	2297.662	0.046641
5.15	532.2681	33.98953	3414.056	ud	460.4621	689.3829	1.105943
5.59							
6.34							
6.76	534.5595	13.83465	2421.763	ud	413.7555	393.5976	ud
8.11							
8.38	519.3816	7.175108	1406.816	ud	314.5221	272.8473	ud
8.92							
9.60	422.6193	3.73292	978.0133	ud	245.8684	251.3244	ud
11.09							
11.67	245.4292	11.93428	612.044	3672.676	119.9397	169.6521	1.307504
12.82							
13.88							
14.89	205.2262	11.00734	577.1923	4372.482	105.1816	161.0456	ud
16.04							
17.08							
17.98	379.3356	7.41353	959.0691	2612.146	134.0637	199.5036	ud
18.96							
19.85							
21.01	333.2151	5.214426	ud	28.42845	ud	56.72896	ud
21.92							
22.93							
23.99	150.1144	5.82896	339.7015	642.598	101.5996	66.58981	ud
25.15							
26.20							
26.79	167.3255	6.068675	849.5905	990.348	116.149	122.1432	ud
27.90	315.224	5.230376	ud	133.154	87.15805	73.48673	ud
29.59							
30.72	73.82423	4.91311	260.9747	180.4152	103.115	91.98495	ud
31.18							
31.75							
32.77	29.68547	3.541036	ud	290.6957	93.28657	35.14159	ud

[a]PV: Pore volume [*]ud: concentrations below method detection limit

Continue **Table G.12**

PV[a]	Ni µg L^{-1}	Sr µg L^{-1}	V µg L^{-1}
0.20	1518.014	1356.268	2.85914
0.76	1309.339	1219.821	1.69427
1.37	862.4461	793.3181	0.75707
2.25	424.1191	367.3264	0.32684
3.13	164.5841	180.308	0.13950
3.97	94.09077	96.10793	0.03108
5.15	31.23911	32.44571	0.02171
5.59			
6.34			
6.76	16.93774	19.00091	ud
8.11			
8.38	13.53808	12.63892	ud
8.92			
9.60	15.20986	10.99505	0.14709
11.09			
11.67	19.55996	10.77307	ud
12.82			
13.88			
14.89	12.49163	8.233506	ud
16.04			
17.08			
17.98	9.186417	7.296629	0
18.96			
19.85			
21.01	6.453192	5.282249	ud
21.92			
22.93			
23.99	6.631212	4.9268	ud
25.15			
26.20			
26.79	5.796183	5.236307	ud
27.90	15.5856	5.045025	ud
29.59			
30.72	7.067825	6.027377	ud
31.18			
31.75			
32.77	ud	3.09064	ud

[a]PV: Pore volume

[*]ud: concentrations below method detection limit

Table G.13. Measurements of the column effluent for the slurry coke during deionized water (DI) input.

PV[a]	pH	Eh	EC[b] ($\mu S\ cm^{-1}$)	Alkalinity ($mg\ L^{-1}$)
0.15	6.23	498.13	2623	633.66
0.54	6.17	437.60	1873	524.00
1.27	6.36	546.75	1346	474.00
1.93	6.16	490.01	1064	358.00
2.74	5.92	544.21	721	318.73
3.45	5.9	517.62	524	188.87
4.64	5.51	498.64	266	86.00
4.91	5.8	490.80	250.8	95.24
5.61	5.17	534.15	115.8	49.90
6.29	5.08	515.33	81.5	37.77
6.54	4.96	509.32	75.4	29.94
6.93	5.13	546.32	75.6	35.71
8.00	4.98	565.11	60	25.64
8.63	5	590.58	60.2	25.69
10.01	4.85	543.20	55.8	27.61
10.55	4.98	619.88	54.3	26.00
11.62	4.9	566.13	52.1	27.72
12.60	4.78	536.01	51.6	19.65
13.53	4.85	493.21	52.1	25.95
14.60	4.86	511.82	51.3	27.72
15.57	4.77	516.84	50.6	27.83
16.81	4.97	557.84	48.4	28.35
17.30	5.02	539.31	41.9	27.94
18.13	4.8	550.25	37.3	21.87
19.21	4.86	539.70	38.4	19.80
20.05	4.9	538.78	36.9	11.93
20.99	4.94	511.24	35.6	19.96
21.97	4.75	551.75	34.3	19.76
23.04	4.77	546.80	33.2	17.96
24.02	4.92	561.91	31.9	23.76
24.56	5.18	541.22	29.55	21.83
25.59	5.01	583.05	34.9	20.87
27.16	5.17	605.01	24.27	21.87
28.20	5.05	429.48	31.3	9.94
28.63	4.99	415.66	30.9	15.84
29.16	5.16	543.64	28.58	17.89
30.11	5.09	554.70	28.81	15.94

[a]PV: Pore volume [b]EC: Electrical conductivity

Table G.14. Major cation concentrations quantified with inductively coupled plasma–optical emission spectroscopy (ICP-OES) in the effluent of the column with slurry coke during deionized water (DI) input.

PV[a]	Ca mg L^{-1}	Fe mg L^{-1}	K mg L^{-1}	Mg mg L^{-1}	Na mg L^{-1}	S mg L^{-1}
0.15	118.138	0.0096	18.6966	39.6136	478.885	128.645
0.54	92.139	0.0632	12.7794	25.0059	292.136	72.6721
1.27	67.1619	0.0583	9.3507	19.665	197.916	52.4042
1.93	52.8426	0.024	6.9687	15.4788	141.058	38.7931
2.74	44.7308	0.0618	4.384	13.2805	73.9878	22.4317
3.45	36.922	0.1263	4.5081	10.4282	42.058	14.8552
4.64	15.0576	1.2333	2.0291	3.5237	14.686	4.7629
4.91	18.2035	0.9032	2.4726	4.3124	20.57	6.8061
5.61						
6.29	4.0144	4.1782	0.7669	0.6718	4.86	1.0312
6.54						
6.93	2.8672	5.1197	0.6114	0.512	4.6385	0.8882
8.00						
8.63	2.4321	2.5611	0.5461	0.4007	4.3777	0.7749
10.01						
10.55	1.8311	3.9294	0.4061	0.2925	3.0917	0.4205
11.62						
12.60						
13.53	1.337	4.4143	0.3285	0.2318	2.8969	0.3447
14.60						
15.57						
16.81	1.2982	4.8224	0.2542	0.1917	2.3388	ud*
17.30						
18.13						
19.21	1.0412	1.7513	0.2698	0.1668	2.8423	0.5175
20.05						
20.99						
21.97						
23.04						
24.02						
24.56	0.6739	1.6966	0.1854	0.1189	2.2889	ud
25.59	0.7791	0.5292	0.2423	0.131	2.77	0.5183
27.16						
28.20	0.7374	0.789	0.3099	0.1946	3.0825	0.2291
28.63						
29.16						
30.11	0.52075	0.7419	0.18875	0.08945	2.99695	0.18805

PV[a]	Ca mg L^{-1}	Fe mg L^{-1}	K mg L^{-1}	Mg mg L^{-1}	Na mg L^{-1}	S mg L^{-1}

[a]PV: Pore volume

[*]ud: concentrations below method detection limit

Table G.15. Measured trace element concentrations by inductively coupled plasma–optical mass spectroscopy (ICP-MS) in the column effluent with slurry coke during deionized water (DI) input.

PV[a]	Al µg L^{-1}	Ba µg L^{-1}	Ca µg L^{-1}	Fe µg L^{-1}	K µg L^{-1}	Mg µg L^{-1}	Mo µg L^{-1}
0.15	ud*	341.0929	126323.7244	47.4769	17346.9214	39114.3154	693.7751
0.54							
1.27	ud	268.5195	76980.7550	78.8840	8728.0681	20876.8206	306.3904
1.93	ud	272.4810	57131.0877	40.8729	6507.5718	15821.1319	219.9579
2.74	ud	316.4384	48697.5861	70.0613	4214.0754	13775.3808	142.5299
3.45	9.1204	378.0643	40031.3614	140.7836	4306.2566	10734.3382	83.0690
4.64	237.6502	565.8068	16330.9556	1390.9374	1984.9616	3954.1621	22.1265
4.91	114.2764	592.2015	19887.8391	958.8048	2296.8779	4289.2272	27.5753
5.61							
6.29	366.7105	304.6301	4154.7846	4657.9454	669.6022	681.8169	2.6033
6.54							
6.93	355.1652	190.0017	2914.4741	5655.0260	577.7165	474.6586	1.3078
8.00							
8.63	411.4080	112.3786	3166.6357	2746.3574	556.0781	371.4513	1.1242
10.01							
10.55	469.2789	65.1652	1529.6811	4121.5779	385.9877	229.1018	0.9078
11.62							
12.60							
13.53	566.1211	39.6569	1392.1488	4954.5034	332.2235	220.9555	1.1583
14.60							
15.57							
16.81	748.1048	29.9156	1292.9647	3959.4417	292.2019	228.3194	ud
17.30							
18.13							
19.21	667.9247	23.1274	814.5564	1925.4341	280.3157	107.5349	1.5688
20.05							
20.99							
21.97	618.3642	17.9689	508.3928	1698.7350	240.2733	84.9139	2.5230
23.04							
24.02							
24.56	691.3165	15.2348	693.6084	1761.9543	236.6949	132.7037	ud
25.59	480.1833	15.8531	229.3530	609.2824	219.2522	61.8705	2.1172
27.16							
28.20	263.8925	14.0889	536.6676	818.9251	267.1752	132.0911	1.2924
28.63							
29.16							
30.11	350.5555	10.7390	251.7175	772.0037	192.6040	33.8566	1.7714

[a]PV: Pore volume *ud: concentrations below method detection limit

Continue **Table G.15**

PV[a]	Ni µg L^{-1}	Sr µg L^{-1}	V µg L^{-1}
0.15	107.6154	2993.4854	6759.3779
0.54			
1.27	97.2664	1378.7967	2791.0315
1.93	99.6794	1003.7842	2098.8847
2.74	123.0122	896.5544	1352.2646
3.45	174.5479	673.2756	817.5767
4.64	654.5728	276.8757	273.3856
4.91	580.9526	302.2118	297.0199
5.61			
6.29	284.8549	55.2044	53.9074
6.54			
6.93	178.6023	41.5887	38.5921
8.00			
8.63	109.1615	34.2211	24.7332
10.01			
10.55	61.6328	25.4306	18.5820
11.62			
12.60			
13.53	45.8005	20.2658	11.0673
14.60			14.0000
15.57			
16.81	35.5087	17.2071	14.2719
17.30			
18.13			
19.21	23.3730	13.0213	19.8938
20.05			
20.99			
21.97	16.9728	10.8099	17.3967
23.04			
24.02			
24.56	16.1193	9.1957	14.9984
25.59	30.6232	9.2272	19.4799
27.16			
28.20	13.5086	11.6826	24.2236
28.63			
29.16			
30.11	9.7229	7.3844	20.1441

[a]PV: Pore volume

*ud: concentrations below method detection limit

Table G.16. Measurements of the columns influent during oil sand process-affected water (OSPW) input.

PV[a]	pH	Eh	EC[b] (mS cm^{-1})	Alkalinity (mg L^{-1})
0.18	8.57	475.91	4.9	726.73
0.44	8.52	429.81	4.88	706.35
0.62	8.47	465.99	4.86	704.37
1.42	8.61	446.45	4.85	707.75
1.94	8.61	485.42	4.84	709.16
2.48	8.76	436.54	4.81	712.30
3.31	8.74	436.88	4.83	710.89
3.58	8.82	424.39	4.81	714.00
4.43	8.75	416.85	4.77	694.44
5.39	8.79	416.36	4.72	715.14
6.67	8.81	463.04	4.7	714.57
7.63	8.82	408.30	4.93	712.87
8.73	8.8	454.52	4.81	716.57
9.73	8.4	443.80	4.88	718.56
10.42	8.46	439.85	4.8	710.58
11.51	8.5	430.00	4.78	713.72
12.36	8.48	465.86	4.75	703.19
13.47	8.55	468.22	4.89	714.00
14.34	8.42	523.75	4.86	738.52
15.30	8.28	480.84	4.86	718.56
16.31	8.35	436.95	4.83	714.29
17.41	8.36	412.28	4.83	734.13
18.41	8.39	419.42	4.78	695.83
19.10	8.24	456.18	4.73	714.29
20.04	8.5	534.30	4.66	732.60
21.64	8.5	534.30	4.66	732.60
22.72	8.74	449.94	4.92	710.32
23.16	8.74	449.94	4.92	710.32
23.70	9.03	387.33	4.86	711.46
24.68	9.01	353.59	4.88	694.44
25.43	8.59	361.33	4.92	718.56
26.42	8.76	467.14	4.84	712.00
27.40	8.88	412.93	4.81	708.58
28.34	8.79	475.83	4.84	717.06
29.32	8.95	469.82	4.88	704.37
30.28	8.35	432.01	4.76	712.87
31.26	8.54	469.56	5.05	705.18
32.29	8.69	488.76	4.93	702.97

PV[a]	pH	Eh	EC[b] (mS cm^{-1})	Alkalinity (mg L^{-1})
33.24	8.45	435.36	4.92	691.70
34.21	8.59	506.78	4.88	674.60
35.06	8.45	435.36	4.92	691.70

[a]PV: Pore volume

[b]EC: Electrical conductivity

Table G.17. Major cation concentrations quantified by inductively coupled plasma–optical emission spectroscopy (ICP-OES) in the column influent during OSPW input.

PV[a]	Ca mg L^{-1}	Fe mg L^{-1}	K mg L^{-1}	Mg mg L^{-1}	Na mg L^{-1}	S mg L^{-1}
0.18						
0.44						
0.62	7.951	ud*	21.177	19.1367	1060.51	78.1026
1.42						
1.94						
2.48						
3.31	6.4873	ud	21.5442	19.6679	1083.6	81.7178
3.58						
4.43						
5.39	6.5222	ud	20.9386	19.122	1062.27	79.2602
6.67						
7.63						
8.73						
9.73						
10.42	9.0037	ud	20.5862	17.9018	1009.6	71.6384
11.51						
12.36						
13.47						
14.34						
15.30						
16.31						
17.41						
18.41						
19.10	23.0997	ud	19.928	18.0666	1027.14	68.6614
20.04	17.0526	ud	21.5397	19.693	1075.49	80.4857
21.64						
22.72						
23.16						
23.70						
24.68						
25.43						
26.42						
27.40						
28.34						
29.32						
30.28						
31.26						
32.29						

PV[a]	Ca mg L^{-1}	Fe mg L^{-1}	K mg L^{-1}	Mg mg L^{-1}	Na mg L^{-1}	S mg L^{-1}
33.24						
34.21						
35.06						

[a]PV: Pore volume

[*]ud: concentrations below method detection limit

Table G.18. Trace element concentrations quantified by inductively coupled plasma–optical mass spectroscopy (ICP-MS) in the column influent during oil sand process-affected water (OSPW) input.

PV[a]	Al µg L−1	Ba µg L−1	Ca µg L−1	Fe µg L−1	K µg L−1	Mg µg L−1	Mo µg L−1
0.18	ud*	ud	7680.8081	ud	19313.2812	17217.3055	1.2191
0.44							
0.62	5.5114	ud	3584.6117	96.2101	19532.0560	16932.5115	ud
1.42	ud	ud	8023.3107	ud	21188.5877	20071.8306	1.8669
1.94							
2.48							
3.31							
3.58							
4.43	ud	ud	6647.8426	14.6264	18126.3398	20757.5417	12.1605
5.39	ud	1.4074	6210.5920	ud	20144.7347	19342.0296	1.8261
6.67							
7.63							
8.73							
9.73							
10.42	ud	ud	9745.2377	3209.5717	17764.2946	18668.9361	ud
11.51							
12.36							
13.47							
14.34							
15.30							
16.31							
17.41	ud	ud	6066.4407	81.2089	20305.2461	21241.3084	1.1853
18.41							
19.10	ud	1.8867	22587.8484	24.5001	20366.9207	21633.2945	ud
20.04							
21.64							
22.72							
23.16							
23.70							
24.68							
25.43							
26.42							
27.40							
28.34							
29.32							
30.28							
31.26							

PV[a]	Al µg L−1	Ba µg L−1	Ca µg L−1	Fe µg L−1	K µg L−1	Mg µg L−1	Mo µg L−1
32.29							
33.24							
34.21							
35.06							

[a]PV: Pore volume

*ud: concentrations below method detection limit

Continue **Table G.18**

PV[a]	Ni µg L−1	Sr µg L−1	V µg L−1
0.18	ud		
0.44			
0.62	ud		
1.42	ud		
1.94			
2.48			
3.31			
3.58			
4.43	ud		
5.39	ud		
6.67			
7.63			
8.73			
9.73			
10.42	ud		
11.51			
12.36			
13.47			
14.34			
15.30			
16.31			
17.41	ud		
18.41			
19.10	ud		
20.04			
21.64			
22.72			
23.16			
23.70			

PV[a]	Ni µg L−1	Sr µg L−1	V µg L−1
24.68			
25.43			
26.42			
27.40			
28.34			
29.32			
30.28			
31.26			
32.29			
33.24			
34.21			
35.06			

[a]PV: Pore volume

*ud: concentrations below method detection limit

Table G.19. Measurements of the dry coke column effluent under oil sand process-affected water (OSPW) input.

PV[a]	pH	Eh	EC[b] (mS cm^{-1})	Alkalinity (mg L^{-1})
0.18	6.11	516.38	5.65	649.40
0.44	6.07	502.73	5.57	598.41
0.62	6.17	490.49	5.49	582.83
1.42	6.14	533.63	5.24	646.71
1.94	6.25	491.39	4.99	690.48
2.48	6.29	516.14	4.86	704.59
3.31	6.2	525.99	4.84	707.75
3.58	6.3	538.57	4.84	709.74
4.43	6.22	447.03	4.77	634.92
5.39	6.23	385.22	4.7	709.74
6.67	6.14	448.02	4.7	718.00
7.63	6.18	395.99	4.93	707.75
8.73	6.14	405.12	4.87	700.60
9.73	6.11	443.33	4.85	697.21
10.42	6.17	454.26	4.81	718.25
11.51	6.42	536.58	4.79	698.60
12.36	6.34	520.36	4.74	671.29
13.47	6.38	538.09	4.9	717.13
14.34	6.44	572.05	4.82	696.00
15.30	6.37	455.23	4.83	694.44
16.31	6.28	497.75	4.82	722.22
17.41	6.34	474.29	4.8	656.06
18.41	6.57	527.81	4.73	715.71
19.10	6.5	450.62	4.7	675.94
20.04	6.75	562.17	4.61	640.00
21.64	6.62	595.31	4.3	738.52
22.72	6.76	458.82	4.93	726.19
23.16	6.79	445.26	4.86	710.00
23.70	6.75	487.11	4.87	776.89
24.68	6.7	518.60	4.85	701.20
25.43	6.7	517.97	4.89	718.56
26.42	6.68	530.33	4.82	704.95
27.40	6.72	523.72	4.81	689.86
28.34	6.64	501.03	4.8	689.72
29.32	6.63	539.71	4.79	689.11
30.28	6.7	455.80	4.72	686.00
31.26	6.62	518.26	5.01	695.65
32.29	6.71	537.88	4.95	697.21

PV[a]	pH	Eh	EC[b] (mS cm^{-1})	Alkalinity (mg L^{-1})
33.24	6.73	511.76	4.92	688.62
34.21	6.8	528.94	4.9	664.68
35.06	6.83	496.06	4.83	664.68

[a]PV: Pore volume

[b]EC: Electrical conductivity

Table G.20. Major cations quantified with inductively coupled plasma–optical emission spectroscopy (ICP-OES) in the column effluent of dry coke during oil sand process-affected water (OSPW) input.

PV[a]	Ca mg L^{-1}	Fe mg L^{-1}	K mg L^{-1}	Mg mg L^{-1}	Na mg L^{-1}	S mg L^{-1}
0.18	128.206	0.0651	28.5409	51.7192	1121.29	283.414
0.44						
0.62	100.6326	0.104167	22.7493	41.7839	936.3747	240.106
1.42	79.8867	ud*	23.3439	35.0308	1057.67	192.264
1.94	33.7433	0.0366	21.0398	23.8012	1038.39	111.886
2.48	17.8727	0.0449	21.7252	21.2311	1090.93	90.924
3.31						
3.58	11.3305	0.112	20.7763	19.8754	1050.38	82.2558
4.43						
5.39	6.4548	0.8825	20.5728	19.4464	1050.7	79.7875
6.67						
7.63	5.3525	0.6639	20.5419	19.3359	1047.71	80.2844
8.73						
9.73						
10.42	7.4933	1.0436	21.384	18.7106	1038.21	78.2389
11.51	8.7589	0.0289	20.6665	19.3862	1044.4	80.7794
12.36						
13.47						
14.34	5.5926	0.0661	20.9398	19.6423	1055.24	80.0976
15.30						
16.31						
17.41	9.4227	0.1771	21.2373	19.5399	1058.02	80.2062
18.41						
19.10	8.3448	0.371	20.5274	18.7119	1033.3	73.5022
20.04	9.1775	ud	22.0638	20.002	1094.75	82.0003
21.64						
22.72						
23.16	10.2313	0.0175	21.2242	19.5055	1054.24	79.6024
23.70						
24.68						
25.43						
26.42						
27.40						
28.34	3.62405	ud	20.9388	19.3055	1050.245	80.39075
29.32						
30.28						
31.26						

PV[a]	Ca mg L^{-1}	Fe mg L^{-1}	K mg L^{-1}	Mg mg L^{-1}	Na mg L^{-1}	S mg L^{-1}
32.29						
33.24						
34.21						
35.06	4.4678	ud	21.2054	19.4054	1065.01	79.532

[a]PV: Pore volume

[*]ud: concentrations below method detection limit

Table G.21. Trace element concentrations quantified by inductively coupled plasma–optical mass spectroscopy (ICP-MS) in the column effluent of dry during oil sand process-affected water (OSPW) input.

PV[a]	Al µg L−1	Ba µg L−1	Ca µg L−1	Fe µg L−1	K µg L−1	Mo µg L−1
0.18	ud*	75.1447	134315.4469	59.0391	25969.5422	60.5290
0.44	ud	73.4318	121927.5349	96.1967	26020.1093	53.5463
0.62	ud	71.0793	112365.4030	121.4958	25914.6005	54.7615
1.42	ud	67.1843	79350.2560	49.3608	21752.6916	63.9033
1.94	ud	73.1199	32365.3454	68.0764	20252.8765	58.7039
2.48	ud	69.6442	17874.8872	256.8871	19874.7749	52.9777
3.31						
3.58	ud	65.3073	10957.1378	153.4653	19901.9019	39.3917
4.43						
5.39	ud	52.4580	6287.1948	943.0972	20290.6742	26.5040
6.67						
7.63	ud	46.0188	6213.2661	701.2011	20114.8351	16.8764
8.73						
9.73		20.0000		740.0000		15.0000
10.42	ud	19.5439	7370.6014	531.4345	19377.2829	12.4519
11.51	ud	17.1024	8659.2855	45.3543	20252.2168	22.9324
12.36						
13.47						
14.34	ud	19.7864	5545.6293	87.3701	20125.2031	12.7882
15.30						
16.31						
17.41	ud	8.6114	9821.4762	854.0050	18941.3173	9.5623
18.41						
19.10	ud	8.8953	7974.9047	142.3419	20509.4730	8.6910
20.04	ud	8.2366	9087.5480	17.2904	20472.0751	15.1557
21.64						
22.72						
23.16	ud	7.8017	10476.7813	38.1376	20343.2848	12.0178
23.70						
24.68						
25.43						
26.42						
27.40						
28.34	ud	6.0118	3363.6352	15.8272	20032.8100	7.3461
29.32						
30.28						
31.26						

PV[a]	Al µg L−1	Ba µg L−1	Ca µg L−1	Fe µg L−1	K µg L−1	Mo µg L−1
32.29						
33.24						
34.21						
35.06	ud	2.2232	4727.6930	147.3588	17012.1926	6.2628

[a]PV: Pore volume

*ud: concentrations below method detection limit

Continue **Table G.21**

PV[a]	Ni µg L−1	Sr µg L−1	V µg L−1
0.18	903.6751	1085.4658	5.8714
0.44	929.1337	1012.1643	6.4041
0.62	876.1153	927.9930	6.5375
1.42	555.3554	684.0924	12.4556
1.94	246.8767	250.4819	15.2202
2.48	104.6340	111.1885	17.0414
3.31			
3.58	45.1380	59.2364	13.6879
4.43			
5.39	30.3416	32.9205	ud
6.67			
7.63	19.5547	22.9633	ud
8.73			
9.73	9.0000	16.0000	
10.42	9.5827	16.7080	ud
11.51	15.8449	16.8750	7.7617
12.36			
13.47			
14.34	7.5823	10.3042	2.4020
15.30			
16.31			
17.41	5.6362	9.0735	ud
18.41			
19.10	4.4119	8.2323	ud
20.04	13.8748	9.8757	15.6879
21.64			
22.72			
23.16	4.8432	10.5717	ud
23.70			

PV[a]	Ni µg L−1	Sr µg L−1	V µg L−1
24.68			
25.43			
26.42			
27.40			
28.34	ud	4.8743	5.5401
29.32			
30.28			
31.26			
32.29			
33.24			
34.21			
35.06	ud	4.1365	3.6926

[a]PV: Pore volume

*ud: concentrations below method detection limit

Table G.22. Measurements of the column effluent of slurry coke during oil sand process-affected water (OSPW) input.

PV[a]	pH	Eh	EC[b] (mS cm^{-1})	Alk (mg L^{-1})
0.15	6.78	500.63	7.8	1890.00
0.29	6.75	488.50	7.84	1675.25
0.42	6.64	473.33	7.56	1612.33
0.78	6.59	467.32	6.7	1414.34
1.20	6.42	484.99	5.69	1053.68
1.44	6.45	519.99	5.25	908.73
2.24	6.21	468.24	4.89	734.13
3.15	6.17	478.53	4.74	732.67
4.35	6.19	498.72	4.72	731.61
5.25	6.22	461.91	4.94	730.69
6.27	6.2	475.03	4.86	712.57
7.21	6.15	485.72	4.82	700.99
7.73	6.14	505.64	4.78	731.46
8.88	6.3	518.49	4.8	706.00
9.68	6.24	506.25	4.76	706.00
10.71	6.28	527.80	4.89	715.71
11.52	6.27	501.14	4.83	704.00
12.42	6.26	414.85	4.82	717.13
13.37	6.14	468.28	4.81	715.14
14.40	6.27	472.96	4.81	718.56
15.34	6.42	500.23	4.73	691.70
15.99	6.43	453.71	4.67	718.56
16.86	6.61	568.47	4.63	741.48
18.36	6.5	581.02	4.29	718.56
19.37	6.6	430.13	4.92	708.00
19.78	6.68	416.75	4.79	710.00
20.29	6.89	487.61	4.88	775.35
21.20	6.53	511.20	4.85	695.83
21.91	6.4	425.27	4.92	700.00
22.84	6.51	528.03	4.8	712.57
23.75	6.49	531.24	4.8	687.87
24.63	6.42	525.62	4.8	693.23
25.55	6.41	538.31	4.79	691.85
26.46	6.59	498.50	4.71	686.51
27.37	6.52	521.14	5.02	701.20
28.33	6.48	546.76	4.94	685.77
29.22	6.44	515.48	4.91	690.48
30.14	6.61	536.26	4.88	666.67

PV[a]	pH	Eh	EC[b] (mS cm^{-1})	Alk (mg L^{-1})
30.93	6.59	508.88	4.83	670.66

[a]PV: Pore volume

[b]EC: Electrical conductivity

Table G.23. Major cation concentrations quantified with inductively coupled plasma–optical emission spectroscopy (ICP-OES) in the column effluent of slurry coke during oil sand process-affected water (OSPW) input.

PV[a]	Ca mg L^{-1}	Fe mg L^{-1}	K mg L^{-1}	Mg mg L^{-1}	Na mg L^{-1}	S mg L^{-1}
0.15	109.614	ud*	41.9311	50.9801	1777.9	283.356
0.29	111.027	0.0331	38.3612	52.6992	1739.5	285.576
0.42	108.093	0.0794	35.7892	52.6847	1663.11	275.086
0.78	94.0371	0.0762	32.9878	47.8562	1503.89	218.78
1.20	66.9175	0.0891	26.604	32.9	1261.48	138.864
1.44	46.0944	0.0831	24.2173	26.607	1159.09	106.999
2.24	21.8952	0.1444	21.6036	22.4964	1070.74	84.4992
3.15	12.9703	0.0705	20.8485	20.8821	1051.4	79.6619
4.35	8.1468	0.116	22.6937	21.0147	1128.5	83.3698
5.25						
6.27	5.8113	0.1757	22.658	20.3777	1134.43	84.0191
7.21						
7.73	4.98725	0.08865	21.05075	19.14635	1024.81	79.28235
8.88	9.1189	0.0599	20.8604	22.2417	1042.94	80.0697
9.68						
10.71						
11.52	6.9163	0.0852	20.7445	18.8519	1048.34	80.1337
12.42						
13.37						
14.40	9.7166	0.1045	21.1873	18.7951	1059.84	79.507
15.34						
15.99	7.8788	ud	20.1134	17.5916	1020.96	72.4366
16.86						
18.36						
19.37						
19.78						
20.29	9.9367	0.0305	20.9904	18.1758	1056.29	80.6861
21.20						
21.91	6.4408	0.0327	21.2376	17.914	1065.85	81.2051
22.84						
23.75						
24.63						
25.55	3.9055	ud	21.8158	18.8133	1081.06	81.6773
26.46						
27.37						
28.33						
29.22						

PV[a]	Ca mg L^{-1}	Fe mg L^{-1}	K mg L^{-1}	Mg mg L^{-1}	Na mg L^{-1}	S mg L^{-1}
30.14						
30.93	4.8575	ud	22.129	19.0018	1115.06	81.9386

[a]PV: Pore volume

[*]ud: concentrations below method detection limit

Table G.24. Trace element concentrations quantified with inductively coupled plasma–optical mass spectroscopy (ICP-MS) in the column effluent of slurry coke during oil sand process-affected water (OSPW) input.

PV[a]	Al µg L−1	Ba µg L−1	Ca µg L−1	Fe µg L−1	Mo µg L−1	Ni µg L−1	Sr µg L−1	V µg L−1
0.15	Ud*	256.3183	114781.9	38.38996	1255.29	107.5815	2989.955	13501.4
0.29	ud	239.791	113919.3	60.07859	1341.772	106.8915	3126.128	13654.72
0.42	ud	241.5977	114084.1	110.7661	1297.699	113.0335	3006.866	13278.18
0.78	20			110	890	96	2400	9800
1.20	13.7721	241.3713	66608.12	131.0793	447.651	85.00638	1572.609	6106.006
1.44	8.6190	254.8947	46421.07	124.5738	266.4056	71.8002	980.5052	4087.011
2.24	ud	260.6041	21321.63	178.7746	100.6318	64.28799	307.8725	1620.775
3.15	ud	215.2169	14150.78	311.9039	30.18821	62.64945	108.7922	902.3169
4.35	ud	222.3469	8546.98	147.8658	41.06644	58.0619	63.30527	544.0683
5.25								
6.27	ud	191.6017	5988.501	191.4722	31.61799	62.0293	41.35938	362.8455
7.21								
7.73	ud	169.1936	5229.671	227.4588	23.55461	63.29083	35.03788	260.876
8.88	ud	171.9939	8897.788	87.91421	24.65971	69.80869	35.4758	237.4191
9.68								
10.71								
11.52	ud	118.2588	6808.834	108.7502	17.62492	55.53365	22.31557	179.5373
12.42								
13.37								
14.40	ud	98.65661	9862.363	133.0202	18.73279	60.09419	18.58316	134.8422
15.34								
15.99	ud	82.37248	7781.789	136.8276	11.84777	49.5236	15.54606	118.3463
16.86		79		40	15	42	16	230
18.36								
19.37								
19.78								
20.29	ud	55.89093	10289.99	69.8306	15.61422	31.70988	16.20273	115.5883
21.20								
21.91	ud	44.37063	6732.715	187.3132	14.41057	21.78997	13.62006	83.89863
22.84								
23.75								
24.63								
25.55	ud	27.48236	4091.326	24.75167	13.10548	13.65604	9.245174	108.0952
26.46								
27.37								
28.33								
29.22								

PV[a]	Al µg L−1	Ba µg L−1	Ca µg L−1	Fe µg L−1	Mo µg L−1	Ni µg L−1	Sr µg L−1	V µg L−1
30.14								
30.93	ud	17.43783	5013.003	34.31147	9.89502	10.47852	8.024972	73.92062

[a]PV: Pore volume

[*]ud: concentrations below method detection limit

Table G.25. Measurements of the column influent during acid rock drainage (ARD) input.

PV[a]	pH	Eh	EC[b] (mS cm^{-1})	Alk (mg L^{-1})
0.24	2.04	838.33	8.38	–
0.39	2.06	840.21	8.39	–
0.54	2	837.37	8.46	–
0.65	2.04	853.22	8.43	–
1.22	2.1	829.31	8.78	–
1.48	2.09	827.80	8.77	–
2.15	2.09	831.58	8.7	–
2.55	2.2	829.24	8.69	–
3.52	2	824.83	8.68	–
3.95	2.12	828.28	8.56	–
5.27	2.05	831.61	8.61	–
6.10	2	836.22	8.5	–
7.19	2.07	827.72	8.76	–
7.92	2.07	827.72	8.76	–
8.03	2.13	829.09	8.65	–
8.98	2.22	825.94	8.69	–
9.96	2.01	825.20	8.9	–
11.04	1.93	836.34	8.84	–
12.02	2.43	829.91	8.76	–
12.68	2.6	834.97	8.63	–
13.61	2.27	830.03	8.53	–
15.18	2.15	830.03	8.53	–
16.24	2.09	836.42	8.4	–
16.67	2.09	836.42	8.4	–
17.20	2.01	843.76	8.56	–
18.02	1.99	833.41	8.79	–
18.95	2	834.65	8.68	–
19.97	2.01	829.41	8.68	–
20.92	2	825.81	8.69	–
21.84	2.08	827.73	8.66	–
22.80	1.94	834.93	8.58	–
23.75	1.98	830.89	8.57	–
24.70	1.9	827.16	8.98	–
25.71	1.97	827.09	8.81	–
26.64	1.93	832.31	8.82	–
27.59	2.04	827.91	8.82	–
28.42	2	830.68	8.66	–
29.47	1.99	824.35	8.81	–
30.41	2.13	827.93	8.78	–

PV[a]	pH	Eh	EC[b] (mS cm^{-1})	Alk (mg L^{-1})
31.05	2.34	827.32	8.55	–

[a]PV: Pore volume

[b]EC: Electrical conductivity

Table G.26. Major cation concentrations quantified with inductively coupled plasma–optical emission spectroscopy (ICP-OES) in the column influent during acid rock drainage (ARD) input.

PV[a]	Ca mg L^{-1}	Fe mg L^{-1}	K mg L^{-1}	Mg mg L^{-1}	Na mg L^{-1}	S mg L^{-1}
0.24						
0.39						
0.54						
0.65						
1.22						
1.48						
2.15						
2.55	391.095	2421.87	Ud*	200.75	210.715	3705.03
3.52						
3.95	405.557	2492.63	0.1239	198.963	189.275	3501.28
5.27						
6.10						
7.19						
7.92						
8.03						
8.98						
9.96						
11.04	405.506	2220.69	ud	200.469	197.573	3674.52
12.02	404.654	2403.58	ud	200.173	203.66	3700.58
12.68	400.662	2542.13	1.3043	205.815	200.902	3506.38
13.61						
15.18						
16.24						
16.67						
17.20						
18.02						
18.95						
19.97						
20.92						
21.84						
22.80						
23.75						
24.70						
25.71						
26.64	382.81	2747.33	1.3043	186.116	194.301	3436.25
27.59						
28.42						
29.47						

PV[a]	Ca mg L^{-1}	Fe mg L^{-1}	K mg L^{-1}	Mg mg L^{-1}	Na mg L^{-1}	S mg L^{-1}
30.41						
31.05						

[a]PV: Pore volume

[*]ud: concentrations below method detection limit

Table G.27. Trace element concentrations quantified with inductively coupled plasma–optical mass spectroscopy (ICP-MS) in the columns influent during acid rock drainage (ARD) input.

PV[a]	Al µg L−1	Ba µg L−1	K µg L−1	Mo µg L−1	Ni µg L−1	Sr µg L−1	V µg L−1
0.24	Ud*	7.2956	185.5526	12.3987	15.4998	98.4764	3.4536
0.39	326.0259	7.5382	193.7886	16.6673	28.9475	110.3974	24.9790
0.54							
0.65	ud	7.5071	184.0733	12.3154	14.2887	101.4230	5.0092
1.22							
1.48							
2.15							
2.55							
3.52							
3.95	20.7077	5.9368	224.1356	ud	13.5609	112.6890	ud
5.27							
6.10							
7.19							
7.92							
8.03							
8.98							
9.96							
11.04							
12.02							
12.68	ud	6.8793	1225.3621	12.8693	15.2498	104.5072	ud
13.61							
15.18							
16.24							
16.67							
17.20							
18.02							
18.95							
19.97							
20.92							
21.84							
22.80							
23.75							
24.70							
25.71							
26.64	ud	7.3616	ud	11.6360	12.8252	106.6856	3.6375
27.59							
28.42							
29.47							

PV[a]	Al µg L−1	Ba µg L−1	K µg L−1	Mo µg L−1	Ni µg L−1	Sr µg L−1	V µg L−1
30.41							
31.05							

[a]PV: Pore volume

[*]ud: concentrations below method detection limit

Table G.28. Measurements of the column effluent for dry coke during acid rock drainage (ARD) input.

PV[a]	pH	Eh	EC[b] (mS cm^{-1})	Alk (mg L^{-1})
0.24	2.3	713.22	8.3	–
0.39	2.28	719.54	8.24	–
0.54	2.16	716.13	8.22	–
0.65	2.24	718.22	8.19	–
1.22	2.35	712.99	8.62	–
1.48	2.17	712.00	8.64	–
2.15	2.18	728.59	8.44	–
2.55	2.2	731.33	8.36	–
3.52	2.02	738.04	8.33	–
3.95	2.21	746.44	8.28	–
5.27	2.24	750.92	8.24	–
6.10	2.08	746.46	8.3	–
7.19	2.07	747.19	8.55	–
7.92	2.34	749.29	8.42	–
8.03	2.14	749.28	8.46	–
8.98	2.26	751.34	8.53	–
9.96	2.01	748.58	8.48	–
11.04	1.99	751.71	8.63	–
12.02	2.45	756.50	8.6	–
12.68	2.6	759.89	8.5	–
13.61	2.3	766.27	8.35	–
15.18	2.16	759.02	7.76	–
16.24	1.97	735.74	8.97	–
16.67	1.98	742.86	8.8	–
17.20	2.1	753.06	8.58	–
18.02	2.15	752.21	8.57	–
18.95	1.97	762.45	8.58	–
19.97	2.02	761.32	8.61	–
20.92	2.02	762.91	8.66	–
21.84	2.09	759.81	8.67	–
22.80	1.95	760.41	8.64	–
23.75	1.98	759.71	8.53	–
24.70	1.9	758.03	9.02	–
25.71	1.97	766.05	8.92	–
26.64	1.99	760.56	8.8	–
27.59	2.03	764.93	8.84	–
28.42	2.02	751.78	8.81	–
29.47	2	757.96	8.77	–

PV[a]	pH	Eh	EC[b] (mS cm^{-1})	Alk (mg L^{-1})
30.41	2.11	756.22	8.64	–
31.05	2.33	758.73	8.64	–

[a]PV: Pore volume

[b]EC: Electrical conductivity

Table G.29. Major cation concentrations quantified with inductively coupled plasma–optical emission spectroscopy (ICP-OES) in the column effluent form dry coke during acid rock drainage (ARD) input.

PV[a]	Ca mg L^{-1}	Fe mg L^{-1}	K mg L^{-1}	Mg mg L^{-1}	Na mg L^{-1}	S mg L^{-1}
0.24	518.6865	2788.56	Ud*	252.871	238.286	3955.77
0.39	521.046	2761.22	ud	240.003	218.953	3826.07
0.54	507.847	2748.51	ud	230.48	211.947	3805.65
0.65	497.087	2510.79	ud	224.533	211.024	3714.41
1.22	458.075	2508.27	ud	216.769	198.918	3831.14
1.48	427.947	2477.92	ud	209.061	209.193	3756.39
2.15						
2.55	403.412	2389.33	ud	204.741	211.168	3766.49
3.52						
3.95	403.251	2439.355	ud	201.719	191.4585	3574.71
5.27						
6.10	398.835	2399.14	ud	203.356	208.811	3728.92
7.19						
7.92	397.56	2541.58	ud	201.27	209.594	3733.4
8.03						
8.98	405.709	2527.6	ud	197.528	199.456	3646.73
9.96						
11.04						
12.02						
12.68	401.7285	2429.805	ud	205.8725	195.996	3456.845
13.61						
15.18						
16.24						
16.67						
17.20	402.92	2156.97	ud	196.082	381.778	3312.55
18.02						
18.95						
19.97	403.583	2637.38	ud	195.934	190.751	3629.44
20.92						
21.84						
22.80						
23.75						
24.70						
25.71						
26.64	400.12	2674.44	ud	194.864	184.561	3378.41
27.59						
28.42						

PV[a]	Ca mg L^{-1}	Fe mg L^{-1}	K mg L^{-1}	Mg mg L^{-1}	Na mg L^{-1}	S mg L^{-1}
29.47						
30.41						
31.05	399.722	2616.21	ud	197.517	195.382	3658.94

[a]PV: Pore volume

[*]ud: concentrations below method detection limit

Table G.30. Trace element concentrations quantified with inductively coupled plasma–optical mass spectroscopy (ICP-MS) in the column effluent from dry coke during acid rock drainage (ARD) input.

PV[a]	Al µg L−1	Ba µg L−1	K µg L−1	Mo µg L−1	Ni µg L−1	Sr µg L−1	V µg L−1
0.24	47364.51	8.313892	3750.533	408.3378	2601.71	1929.643	3416.322
0.39	45228.08	3.317172	2184.541	391.339	2171.316	1617.984	3029.371
0.54	41341.26	1.924838	1275.119	365.8314	1857.878	1402.095	2843.853
0.65	38232.8	1.349059	1009.3	243.0729	1616.539	1246.522	1668.164
1.22	24999.38	ud*	303.5009	190.4771	714.4275	672.3961	1105.196
1.48	18810.55	1.668346	190.0096	154.2167	446.4067	461.3182	807.2494
2.15							
2.55	9358.021	ud	ud	80.42259	151.4224	204.1129	379.1831
3.52							
3.95	6901.419	ud	ud	33.87416	165.8374	232.8348	107.4732
5.27							
6.10	6443.165	ud	ud	40.37978	97.98733	125.57	179.0724
7.19							
7.92	7077.534	ud	295.4103	47.88127	128.583	140.8568	259.8007
8.03	6500			40	90	90	210
8.98	5789.165	ud	ud	44.65659	83.9515	98.66322	191.8812
9.96							
11.04							
12.02	4196.303	ud	ud	30.83909	66.12763	92.94982	116.5478
12.68	3835.6	8.344432	ud	33.97291	75.25845	98.64882	141.3396
13.61	3900			40	70	70	170
15.18	2852.766	ud	ud	41.20351	66.34198	81.04558	176.3266
16.24							
16.67							
17.20	2369.431	ud	87.01985	36.49628	247.5518	29.81811	156.3514
18.02							
18.95							
19.97	1983.54	2.878847	ud	39.8886	48.06121	32.12656	123.7434
20.92							
21.84							
22.80							
23.75							
24.70							
25.71							
26.64	1153.253	ud	ud	43.82254	39.569	31.26745	92.4503
27.59							
28.42							

PV[a]	Al µg L−1	Ba µg L−1	K µg L−1	Mo µg L−1	Ni µg L−1	Sr µg L−1	V µg L−1
29.47							
30.41							
31.05	669.2527	ud	ud	21.32908	25.09269	18.21648	56.44334

[a]PV: Pore volume

[*]ud: concentrations below method detection limit

Table G.31. Measurements of the column effluent from slurry coke during acid rock drainage (ARD) input.

PV[a]	pH	Eh	EC[b] (mS cm^{-1})	Alk (mg L^{-1})
0.20	3.31	553.93	11.98	–
0.32	3.15	579.35	11.62	–
0.46	2.86	622.34	10.72	–
0.61	2.65	650.65	9.89	–
0.74	2.67	666.06	9.07	–
0.85	2.41	669.45	8.86	–
1.79	2.38	695.03	8.63	–
2.77	2.11	700.83	8.56	–
3.85	2.01	705.78	8.7	–
4.82	2.49	710.31	8.67	–
5.47	2.59	706.53	8.6	–
6.40	2.3	712.44	8.57	–
7.96	2.22	712.90	7.97	–
9.00	2.01	698.44	9.4	–
9.43	1.93	698.96	9.23	–
9.55	1.93	698.31	9.18	–
9.96	2.09	700.70	9	–
10.77	2.12	699.59	9.01	–
11.70	1.91	709.39	9.05	–
12.71	2.03	708.52	8.97	–
13.66	2.01	713.24	8.92	–
14.57	2.07	708.83	9	–
15.53	1.94	712.21	8.98	–
16.46	1.98	716.50	8.85	–
17.41	1.9	712.36	9.27	–
18.41	1.97	717.96	9.19	–
19.33	1.92	714.14	9.1	–
20.29	2.04	718.16	9.02	–
21.11	2.03	715.38	8.92	–
22.15	1.98	717.78	8.84	–
23.09	2.11	718.22	8.46	–
23.72	2.32	718.41	8.8	–
24.72	1.99	723.20	8.77	–
25.40	2	721.89	9.22	–
26.00	2.07	721.32	9.22	–
26.44	2.01	717.46	9.32	–
27.26	2.05	715.84	9.22	–
27.68	2.03	716.74	9.2	–

PV[a]	pH	Eh	EC[b] (mS cm^{-1})	Alk (mg L^{-1})
27.95	2	717.83	9.23	–
28.04	2.06	721.83	9.12	–
29.12	2.01	722.72	9.07	–
29.38	2.01	721.52	9.17	–
30.52	2	720.34	9.14	–
31.02	2	720.56	9.12	–

[a]PV: Pore volume

[b]EC: Electrical conductivity

Table G.32. Major cation concentrations quantified with inductively coupled plasma–optical emission spectroscopy (ICP-OES) in the column effluent from slurry coke during acid rock drainage (ARD) input.

PV[a]	Al mg L^{-1}	Ca mg L^{-1}	Fe mg L^{-1}	K mg L^{-1}	Mg mg L^{-1}	Na mg L^{-1}	S mg L^{-1}
0.20	212.2635	501.4355	1672.9	59.7396	366.9345	1582.435	3829.145
0.32	215.886	501.093	1713.18	53.3541	355.381	1418.96	3795.44
0.46	197.823	499.718	1930.62	31.3023	331.531	1062.11	3809.08
0.61	167.311	500.505	2146.32	19.1728	291.32	761.107	3820.63
0.74	103.844	520.728	2341	8.2119	238.562	419.508	3646.72
0.85							
1.79	26.4966	492.92	2458.33	Ud*	201.451	196.758	3695.12
2.77	16.6781	420.921	2308.53	ud	200.682	196.247	3621.2
3.85	10.4263	409.854	2289.43	ud	198.701	193.978	3675.25
4.82							
5.47	6.5058	405.293	2462.96	ud	204.329	190.51	3437.78
6.40	5.9008	408.438	2712.19	ud	203.654	199.538	3801.74
7.96	4.1204	403.259	2660.6	ud	196.546	190.363	3646.55
9.00							
9.43							
9.55							
9.96	3.48795	407.038	2060.37	ud	197.2355	392.954	3288.55
10.77							
11.70							
12.71	2.4172	406.877	2622.36	ud	194.402	182.189	3636.57
13.66							
14.57							
15.53							
16.46							
17.41							
18.41							
19.33	0.5881	383.8765	2688.355	ud	187.307	178.4755	3355.075
20.29							
21.11							
22.15							
23.09							
23.72							
24.72	1.1757	402.713	2614.17	ud	207.734	200.211	3793.34
25.40							
26.00							
26.44							
27.26	1.646	405.785	2590.54	ud	205.756	193.073	3728.08

PV[a]	Al mg L^{-1}	Ca mg L^{-1}	Fe mg L^{-1}	K mg L^{-1}	Mg mg L^{-1}	Na mg L^{-1}	S mg L^{-1}
27.68							
27.95							
28.04							
29.12							
29.38	0.9521	407.305	2588.82	ud	207.709	195.28	3808.73
30.52							
31.02	0.8078	393.059	2621.68	ud	197.802	180.581	3220.31

[a]PV: Pore volume

[*]ud: concentrations below method detection limit

Table G.33. Trace element concentrations quantified with inductively coupled plasma–optical mass spectroscopy (ICP-MS) in the column effluent from slurry coke during acid rock drainage (ARD) input.

PV[a]	Al	Ba	K	Mo	Ni	Sr	V
	µg L−1	µg L−1	µg L−1	µg L−1	µg L−1	µg L−1	µg L−1
0.20	180433.2019	67.6353	60253.4492	3.4109	8459.0756	6846.5065	5615.9260
0.32	180179.9617	66.2449	53348.6526	5.4455	7777.6176	6410.0706	9139.3124
0.46	157189.6551	32.5869	29069.7184	18.9491	6267.0581	5229.7336	19592.3456
0.61	133899.9927	19.0189	17458.7984	47.2037	4351.4930	4146.3499	22390.5422
0.74	98964.9539	9.3355	8113.9348	77.0511	2495.6435	2494.3376	16751.2344
0.85	86691.5334	5.8750	4610.4615	82.7890	2061.9865	1839.6420	13462.2280
1.79	26902.5564	ud*	ud	98.5610	407.2338	667.0413	2744.1463
2.77	17068.9585	ud	ud	98.8441	272.2338	267.0106	1426.9276
3.85	10663.6896	ud	ud	84.8680	192.9425	150.4094	802.2062
4.82	7327.8540	ud	ud	61.8731	150.3142	145.9997	395.0660
5.47	5621.3097	ud	ud	57.2356	135.3936	126.9524	317.3383
6.40	5967.2372	ud	ud	102.0394	114.3570	91.6695	711.6267
7.96	3773.3425	ud	ud	92.6642	95.9544	90.2285	522.6933
9.00							
9.43							
9.55							
9.96	3091.2263	ud	ud	54.1403	293.2344	28.5380	344.4583
10.77							
11.70							
12.71	2231.5757	ud	ud	48.6912	64.5913	38.1245	209.9591
13.66							
14.57							
15.53							
16.46							
17.41							
18.41							
19.33	1293.4196	ud	ud	19.3599	55.2896	28.9026	119.4636
20.29							
21.11							
22.15							
23.09							
23.72							
24.72	1271.0216	ud	ud	11.3403	44.4433	21.1484	101.9625
25.40							
26.00							
26.44							
27.26	1952.8871	ud	ud	8.4464	50.1449	24.3658	149.8316

PV[a]	Al µg L−1	Ba µg L−1	K µg L−1	Mo µg L−1	Ni µg L−1	Sr µg L−1	V µg L−1
27.68							
27.95							
28.04							
29.12							
29.38	1222.5877	ud	ud	11.4600	45.1734	21.1013	83.8479
30.52							
31.02	1220.0344	ud	ud	7.4563	38.5321	15.8389	65.8891

[a]PV: Pore volume

[*]ud: concentrations below method detection limit

APPENDIX H: CUMULATIVE MASS RELEASE

Table H.1. Cumulative mass release per kg of fluid petroleum coke for the small columns. DC: dry coke; SC: slurry coke.

Elements	DI[a] (µg kg^{-1})		OSPW[b] (µg kg^{-1})		ARD[c] (µg kg^{-1})	
	DC	SC	DC	SC	DC	SC
V	1.27	5030	70.5	10100	3290	12800
Ni	1170	1330	760	651	2110	3550
Mo	3.82	514	276	869	758	610
Al	4500	6980	0.00	7.94	80000	127000
Mn	3540	2690	3030	1570	6550	5310
Ti	0.00	5.56	1.60	35.9	605	1220
Sr	1060	2810	890	2030	1820	2820
Se	0.31	177	2.00	326	399	1050
Co	145.0	102	99.8	46.3	404	387
As	1.61	6.28	0.00	8.53	73	155
U	0.00	1.06	0.08	2.44	6.33	14
Zn	14500	8300	4610	2270	29900	28600
Cu	11.8	15.6	911	2320	581	425

[a]DI: Deionized water

[b]OSPW: synthetic oil sand processing affected water

[c]ARD: Acid rock drianage

Table H.2. Cumulative mass release during sequential water input phases for the large column. Negative values mean attenuation in their concentrations.

Elements	DI[a] (µg kg^{-1})	OSPW[b] (µg kg^{-1})	OSPW[c] (µg kg^{-1})	ARD[d] (µg kg^{-1})	Total (µg kg^{-1})	Leaching efficiency
V	13	123	49	4160	4350	0.31%
Ni	803	0	-10	1360	2160	0.40%
Mo	4	280	2	235	520	0.69%
Al	3540	6	354	63500	67400	0.94
Mn	2980	156	3	2970	6100	7.89
Ti	1	2	2	479	483	0.03
Sr	860	54	-130	380	1170	1.47
Se	20	1	-16	290	295	29.46
Co	92	1	2	204	298	4.81
As	0	0	-31	45	14	0.62
U	0	0	-22	21	-1	0
Zn	3430	50	14	750	4240	12.34
Cu	240	80	-58	600	850	7.36

[a]DI: Deionized water

[b]OSPW: synthetic oil sand processing affected water

[c]OSPW: field oil sand processing affected water

[d]ARD: Acid rock drainage

APPENDIX I: BREAKTHROUGH CURVE

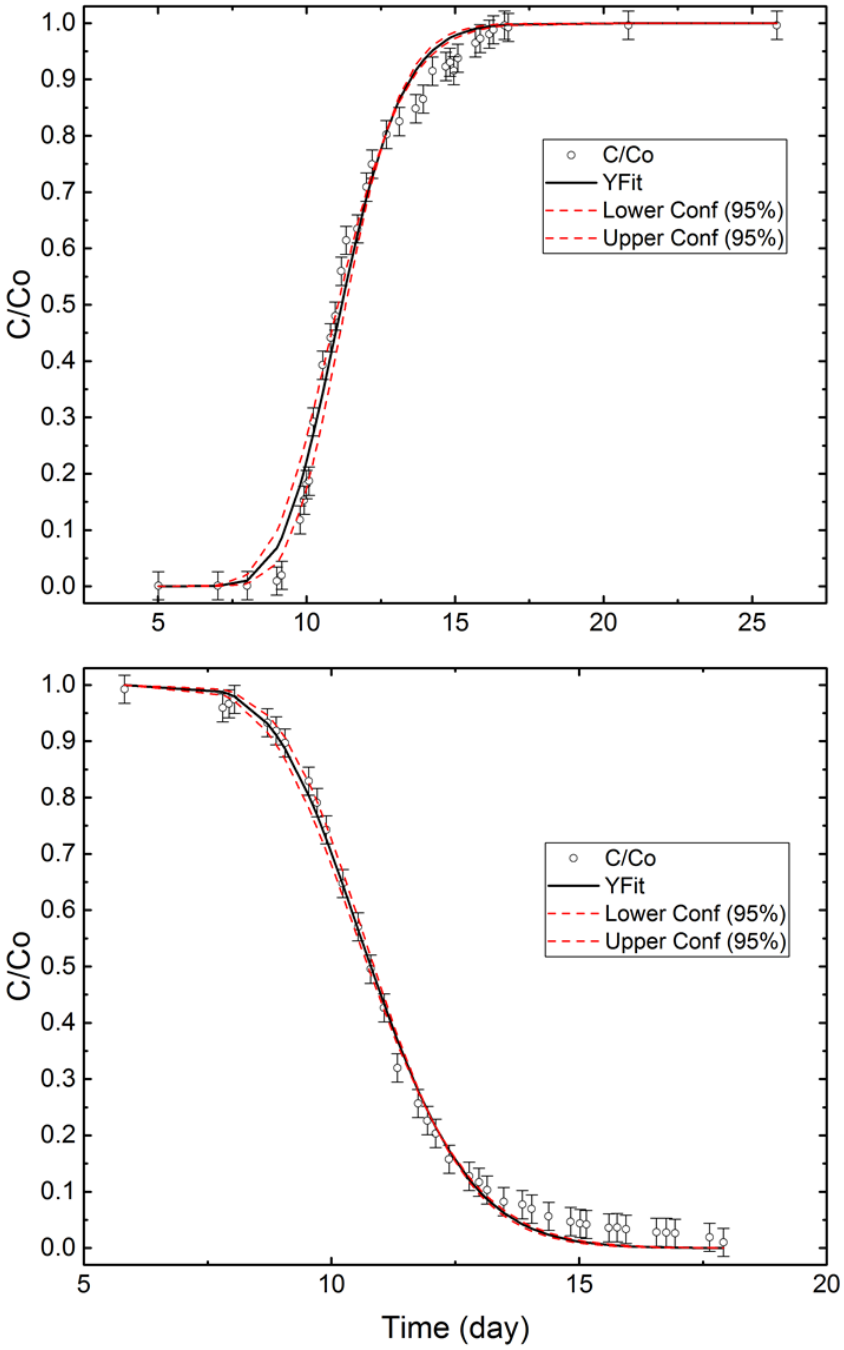

Figure I.1. Breakthrough curve for the first tracer test of the large column; injection (top) and decay (bottom). Error bars represent the electrode ±2.5% electrode sensitivity. Red dashed lines indicate the lower and higher 95% confidence.

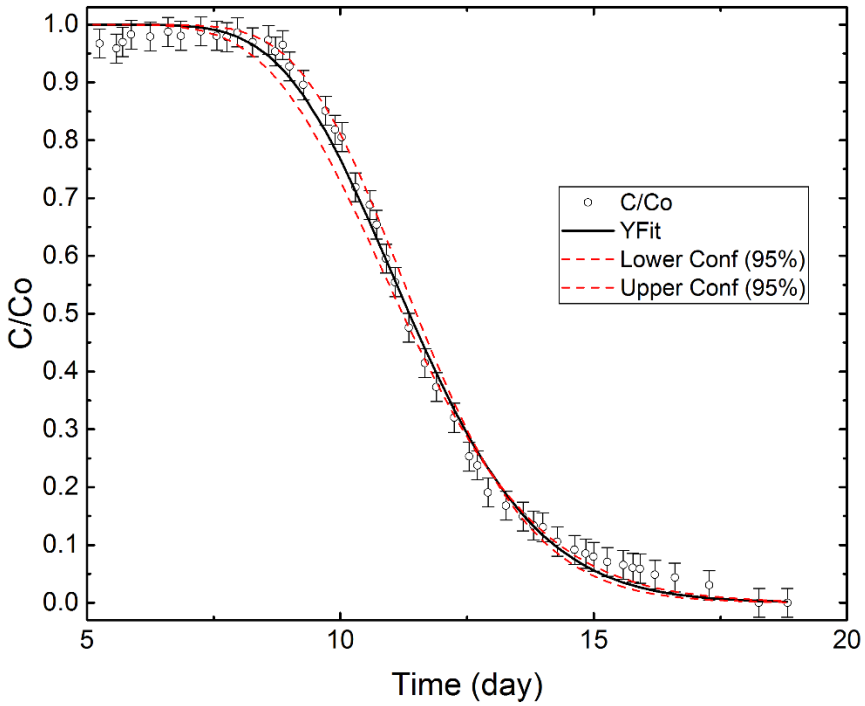

Figure I.2. Breakthrough curve for the decay part of the second tracer test on the large column. Error bars represent the electrode ±2.5% electrode sensitivity. Red dashed lines indicate the lower and higher 95% confidence.